Long memory model of resting state functional MRI

zur Erlangung des akademischen Grades

Doktoringenieur
(Dr.-Ing.)

von M.Sc. Wonsang You

geb. am 23.12.1977 in Seoul (Republik Korea)
genehmigt durch
die Fakultät für Elektrotechnik und Informationstechnik
der Otto-von-Guericke-Universität Magdeburg

Gutachter
Prof. Dr. Udo Seiffert
Prof. Dr. Rolf Findeisen
Prof. Dr. Christian Windischberger

Promotionskolloquium am 30.09.2013

Schriftliche Erklärung

Ich erkläre hiermit, dass ich die vorliegende Arbeit ohne unzulässige Hilfe Dritter und ohne Benutzung anderer als der angegebenen Hilfsmittel angefertigt habe; die aus fremden Quellen direkt oder indirekt übernommenen Gedanken sind als solche kenntlich gemacht.

Insbesondere habe ich nicht die Hilfe einer kommerziellen Promotionsberatung in Anspruch genommen. Dritte haben von mir weder unmittelbar noch mittelbar geldwerte Leistungen für Arbeiten erhalten, die im Zusammenhang mit dem Inhalt der vorgelegten Dissertation stehen.

Die Arbeit wurde bisher weder im Inland noch im Ausland in gleicher oder ähnlicher Form als Dissertation eingereicht und ist als Ganzes auch noch nicht veröffentlicht.

Magdeburg, 2. Januar 2013

Dedicated to my Lord Jesus Christ
and lovely wife Miae Jeon

Abstract

In the latest years momentous advance has been made in understanding the endogenous brain dynamics from resting state functional MRI (rs-fMRI) signals. An rs-fMRI signal tends to have long memory in time as well as the $1/f$ power spectrum at low frequencies. A few statistical models of rs-fMRI time series, such as fractional Gaussian noise (FGN), had been proposed to describe such properties called the fractal behavior. Nonetheless, the long memory properties have not been elucidated by the underlying physical mechanism. In addition, how such properties have an impact on large-scale functional networks of the brain has been unclear. This thesis develops not only a parsimonious model of long memory in rs-fMRI, which provides us hypothetical ideas on these unresolved issues, but also advanced techniques for estimating intrinsic functional connectivity among brain regions hidden beyond the long memory phenomenon of rs-fMRI signals.

The long memory model of rs-fMRI was constructed by extending the present models of cerebral hemodynamics which describe the association between synaptic activities and fMRI signals. This model empowers us to deduce a rigorous hemodynamic condition that brings about long memory in rs-fMRI time series, and has essential implication on resting state brain dynamics. First, the impulse hemodynamic response to resting state brain activity may have considerably different shape from the typical hemodynamic response function corresponding to evoked state. The variability of hemodynamic responses directs us to hypothesize the history dependent excitability of hemodynamic response such that the hemodynamic state is subordinate to the history

of brain activities. Second, the nonlinearity of hemodynamics has little influence on long memory properties in rs-fMRI data. Third, a fractionally integrated (FI) process can be taken into account as a novel statistical model of rs-fMRI time series since it is suitable for the long memory model of hemodynamic response. Lastly, the heterogeneity of fractal behavior among brain regions incurs significant divergence in both functional connectivity and information flow between rs-fMRI signals and the corresponding spontaneous neuronal activities.

To cope with the fractal-driven connectivity distortion in rs-fMRI, nonfractal connectivity was proposed as a novel concept of resting state functional connectivity. It is defined as the correlation of nonfractal constituents of two rs-fMRI time series that are independent of fractal behavior, and is comparable to the fractal connectivity defined as the convergence of wavelet correlation. Although the nonfractal connectivity is not akin to correlation of neuronal population activities, it is capable of efficaciously mitigating the inaccuracy of functional connectivity estimation attributed to fractal behavior. A diversity of wavelet-based estimators for both nonfractal connectivity and fractal connectivity were developed and verified through simulation studies. Moreover, a multivariate method was suggested as a robust estimator of memory parameter which is resilient to severe signal contamination. This fractal-based approach to resting state functional connectivity has been effectively exploited for the analyses of both human and animal brain. These applications demonstrate that the fractal-based analysis is instrumental in revealing the between-group difference in functional connectivity.

In consequence, all these results may give valuable insights on the scientific implication of fractal behavior on functional connectivity, and lead to further exploration of endogenous brain dynamics beyond fractal behavior of rs-fMRI.

Zusammenfassung

In den letzten Jahren gab es wichtige Fortschritte im Verständis von endogenen, dynamischen Vorgängen im Gehirn anhand von funktionellen resting state MRT (rs-fMRT) Signalen. rs-fMRT Signale neigen zu einem Langzeitgedächtnis in der Zeitdomäne sowie zu einem $1/f$ Signalverlauf bei niedrigen Frequenzen im Leistungsspektrum. Wenige statistische Modelle von rs-FMRT Zeitsignalen, wie z.B. fractional Gaussian noise (FGN) wurden vorgeschlagen um dieses sogenannte fraktale Verhalten zu beschreiben. Diese Langezeitgedächtis Eigenschaften wurden bisher nicht durch physikalische Mechanismen erklärt. Darüberhinaus ist der Einfluss dieser Eigenschaften auf die großen funktionellen Netzwerke im Gehirn unklar. In dieser Doktorarbeit wurde nicht nur ein einfaches Model des Langzeitgedächtnis von rs-fMRT Signalen, welche hypothetische Ideen für die ungeklärten Fragen liefern, entwickelt sondern darüberhinaus auch spezielle Methoden um intrisische funktionale Verbindungen zwischen Hirnregionen abzuschätzen, die von dem Langzeitgedächtis der rs-fMRT Signale verdeckt sein können.

Das Langzeitgedächtnismodel von rs-fMRT Daten wurde auf Basis bestehender Modelle der cerebralen Haemodynamik, die Verbindung zwischen synaptischer Aktivität und fMRI Signal beschreiben, entwickelt. Dieses Model ermöglicht einen präziesen haemodynamischen Zustand zu beschreiben, der für das Langzeitgedächtnis verantwortlich ist und einen essentiellen Einfluss auf die dynamischen Vorgänge im Hirn im resting state hat. Erstens kann die spontale haemodynamische Antwort auf Hirnaktivität im resting state eine andere Form aufweisen als die haemodynamische Antwort für ein

evoziertes Signal. Die Variablität der haemodynamischen Antworten führte zur Vermutung der vergangenheitsabhängigen Erregbarkeit der haemodynamischen Antwort, so als sei der haemodynamische Zustand abhängig von der Vergangenheit der Hirnaktivität. Zweitens hat die Nichtlinearität der Haemodynamik nur einen geringen Einfluss auf die Eigenschaften des Langzeitgedächtnisses von rs-fMRT Daten. Drittens kann ein fractionally integrated (FI) process als neues statistisches Modell fur rs-fMRT Zeitreihen herangezogen werden, da es in der Lage ist die Vergangenheitsabhängigkeit der haemodynamsichen Antwort zu beschreiben. Zuletzt ist es die Heterogenität des fraktalen Verhaltens zwischen Hirnregionen die einen signifikaten Unterschied bei der funktionalen Konnektivität und dem Informationsfluss zwischen rs-fMRT Signalen und somit der dazugehörigen spontanen neronalen aktivität hervoruft. Nichtfraktale Konnektivität wird als neues Konzept zur Beschreibung von funktionaler Konnektivität im resting state vorgestellt um den störenden Einfluss des fraktalen Verhaltens in rs-fMRT zu beseitigen. Sie ist definiert als Korrelation von nichtfraktalen Bestandteilen von zwei rs-fMRT Zeitreihen die unabhängig von fraktalem Verhalten ist, ähnlich wie die fraktale Konnektivität als Konvergenz der Wavelet Korrelation definiert ist. Auch wenn die nichtfraktale Korrelation nicht sehr ähnlich der Korrelation von neuronaler Aktivität ist, ist sie dennoch in der Lage den störenden Einfluss des fraktalen Verhaltens auf die Bestimmung der funktionalen Konnektivität wirksam abzuschwächen. Für die Bestimmung von nichtfraktaler wie auch fraktaler Konnektivität wurden eine Vielzahl von Wavelet basierter Methoden entwickelt und durch Simulationen überprüft. Darüber hinaus wird eine multivariate Methode zur Bestimmung der Gedächtnis Parameter vorgeschlagen, die robust gegenüber größeren Signalstörungen ist. Dieser fraktale Ansatz der funktionellen Konnektivität von Hirnregionen im resting state wurde erfolgreich bei der Analyse sowohl beim Menschen als auch beim Tier angewendet. Die Anwendung zeigt, dass dieser fraktale Ansatz in der Lage ist Gruppenunterschiede in der funktionalen Konnektivität zu

erkennen.

All diese Ergebnisse können eine neue nützliche Blickweise auf die Auswirkungen von fraktalem Verhalten auf die funktionale Konnektivität eröffnen und Untersuchungen von endogenen dynamischen Vorgängen im Gehirn jenseits des fraktalen Verhaltens von rs-fMRT Signalen ermöglichen.

Contents

List of Figures

List of Tables

Chapter 1

Introduction

The brain is so dynamic that brain activities are ceaseless even at rest. Cognitive processes such as dreaming or emotion follow one after another when someone sleeps or takes rest. Just before falling asleep, his brain may become more active due to either feeling anxiety about having a lot on his plate, or joyful news about his success in an important examination. Moreover, the brain potentially consumes a great deal of energy during rest while an external stimulation to the brain brings about relatively small increase in neuronal activities (Shulman et al., 2004). The ongoing brain activities arouse us curiosity about a huge functional network of endogenous brain activities concealed behind resting state neuroimaging signals. The great exploration of the resting brain goes way back to the pioneering observation of *low frequency fluctuation* (LFF) in resting state blood-oxygen-level-dependent (BOLD) signals of functional magnetic resonance imaging (fMRI) that was performed by Biswal et al. (1995) (see Ogawa et al. (1990) for the BOLD contrast). Since their monumental discovery, attention on spontaneous brain dynamics has tremendously increased during a couple of decades.

One typical approach to LFF is to identify the spatial pattern of coherent brain activities in terms of *functional connectivity* which is defined as the strength of correlation between neurophysiological processes in remote brain regions (Auer, 2008; Fox & Raichle, 2007). A diversity of approaches to resting state functional connectivity have been developed including cross-correlation (Greicius et al., 2007), partial correlation (Marrelec et al., 2007; Salvador et al., 2005), hi-

1

erarchical clustering (Cordes et al., 2002; Salvador et al., 2005), and independent component analysis (ICA) (Beckmann et al., 2005; van de Ven et al., 2004).

The other growing approach to LFF is to analyze the *long memory* phenomenon (also called the *fractal behavior*). A BOLD signal taken at rest tends to exhibit long-range temporal dependence according to a special order of self-similarity and its power spectrum follows an $1/f$ power-law scaling across low frequencies (Cordes et al., 2001; Expert et al., 2011; Herman et al., 2011; Maxim et al., 2005; Stam & de Bruin, 2004; Van de Ville et al., 2010; Wink et al., 2008; Woolrich et al., 2001; Zarahn et al., 1997). These properties are crucial marks of fractal behavior (Beran, 1994), and can be summarized as a single parameter called the fractal dimension.[1] The parameter can be effectively measured by modeling the resting state BOLD signal as a long memory process; the most popular long memory model for resting state BOLD signals has been the fractional Gaussian noise (FGN) (Maxim et al., 2005; Meyer, 2003; see section 2.7.2.1 for its mathematical definition).

Two critical neuroscientific problems relevant to long memory remain unsolved. First, the physical mechanism of long memory in resting state BOLD signals has not been well understood. It is a complicated problem since the origin of the long memory phenomenon is not solitary; the long memory properties may arise from various factors such as respiration (Birn et al., 2006; Cordes et al., 2001; Fadel et al., 2004; Peng et al., 2002), cardiovascular activity (Cordes et al., 2001; Peng et al., 1995; Schmitt & Ivanov, 2007; West et al., 1999; Yamamoto et al., 1995), system noise from instruments as well as neuronal activities (Allegrini et al., 2009; Mazzoni et al., 2007; Teich, 1989; Teich et al., 1997). The diversity of fractal origins makes it difficult to figure out the mechanism of long memory. Second, the relationship between long memory and functional connectivity has not been clarified either theoretically or empirically. Recent studies have suggested indirect evidences supporting that the fractal behavior may be associated with neurophysiological activities. As an example, it has been ob-

---

[1] The fractal parameter can be represented in terms of Hausdorf dimension, Hurst exponent, and memory parameter. On the other hand, a single parameter is sometimes not enough to represent the fractal behavior of a time series. In this case, the fractality can be described by a spectrum of exponents called the *singularity spectrum*. Such a process is called the *multifractal process* (Riedi, 1999).

served that resting state BOLD signals have a tendency to have long memory in gray matter composed of neuronal cell bodies rather than in either white matter or cerebrospinal fluid (CSF) regions (Wink et al., 2008). However, this observation gives us no implication about functional interaction between remote brain regions. Indeed, two approaches to LFF, the long memory analysis and the functional connectivity analysis, have been separately developed so far.

The broad goals of this study are not only to provide theoretical solutions for these problems by formulating a theoretical model of long memory in resting state fMRI through a reasonable hypothesis of its physical mechanism, but also to suggest advanced techniques for analyzing resting state functional connectivity on the basis of the long memory model of resting state BOLD signals. The model would allow figuring out not only the association between long memory and its underlying physical mechanism but also the inherent implication of fractal behavior on functional connectivity among endogenous brain activities.

The most robust clues for solving these problems can be found from the recent studies on long memory in cerebral hemodynamic activities. It was found that the spontaneous fluctuation pattern of cerebral blood volume and flow also tends to exhibit long memory (Eke et al., 2006; Herman et al., 2009; Latka & Latka, 2003; Latka et al., 2005; West et al., 2003; Zhang et al., 2000). A BOLD signal directly reflects the temporal changes in cerebrovascular volume and flow activities, and it has been admittedly supposed that the cerebrovascular activities are indirectly correlated with neuronal activities (Buxton, 2002). In other words, in fMRI the neuronal information is mediated by cerebral hemodynamics and transformed into a BOLD signal. In this reason, a BOLD signal taken at evoked state has been usually modeled as either the linear convolution of neuronal activities with hemodynamic response function (HRF) or a set of nonlinear differential equations describing the hemodynamic mechanism linking a BOLD signal to the underlying neuronal activity (see section 2.1). Hence, it is natural to assume that the cerebral hemodynamics has the strongest effect on long memory phenomenon of resting state BOLD signals among all fractal sources. These collective empirical studies lead us to consider ascribing the fractal behavior of resting state BOLD signals to cerebral hemodynamics.

Motivated by these clues, a long memory model of hemodynamic response to

spontaneous neuronal activity is proposed in Chapter 3 to describe the mechanism of fractal behavior driven by hemodynamic activities as well as the influence of fractal behavior on functional connectivity. The primary ideas of this hemodynamic model include generalizing the conventional HRF which has been applied to evoked state, and finding the hemodynamic condition that gives rise to fractal behavior in resting state BOLD signals. One merit of building an extended hemodynamic model to describe the long memory phenomenon is that it can act as a theoretical basis to figure out the impacts of hemodynamic fractal behavior on the relationship between neuronal activities and BOLD signals.

This extended model of hemodynamic response provides important inferences on resting state fMRI that have been unknown so far. First, the shape of impulse hemodynamic response is influenced by the history of past neuronal activities. In other words, the shape of HRF may dynamically alter according to neuronal states, which results in the considerable difference of HRF between resting state and evoked state. This property of hemodynamic response is named the *history dependent excitability* (HDE). Second, the impact of nonlinearity in BOLD signals on long memory properties is negligible. This property can be effectively inferred through the nonlinear extension of the linear long memory model based on Volterra series expansion. Third, the fractionally integrated (FI) process can be considered as a novel statistical model of resting state BOLD signals since it is more suited for the hemodynamic mechanism of long memory than the FGN process. This idea is intuitively reasonable since the FI process model encompasses a wide range of brain activities while the FGN model is limited to specify the complexity of neuronal activities controlled by numerous hidden parameters. Lastly, the heterogeneous fractal behaviors between brain regions result in the connectivity distortion - the discrepancy of both undirectional and directional connectivity between resting state BOLD signals and the corresponding neuronal activities. In this sense, the fractal behavior may be viewed as a non-neuronal hindrance to functional connectivity analyses since it widens the gap of statistical properties in connectivity between resting state BOLD signals and neuronal activities.

Based on the proposed model of hemodynamic response, a new class of fractal-based techniques for analyzing resting state functional connectivity has been de-

veloped (see Chapter 4). The techniques are summarized as the following three terms. First, a novel notion of resting state functional connectivity, called the *nonfractal connectivity*, was suggested to correct the fractal-driven connectivity distortion expected by the proposed hemodynamic model. The basic idea underlying the nonfractal connectivity is to split a resting state BOLD signal into two parts - fractal and nonfractal components on the basis of the FI process model. The nonfractal connectivity is defined as the correlation of nonfractal components whose statistical properties are independent from fractal behaviors. The nonfractal connectivity may still be interrupted by non-neuronal physiological factors, but at least it is less affected by fractal behaviors than Pearson correlation is affected. The concept of nonfractal connectivity is comparable to *fractal connectivity* which is defined as the asymptotic value of wavelet correlations over low frequency scales (Achard et al., 2008). The theoretical relevance of nonfractal connectivity to fractal connectivity was studied. Second, a variety of wavelet-based methods were developed as estimators of both nonfractal connectivity and fractal connectivity; the wavelet transform is suitable to deal with long memory since it effectively decomposes energy of a long memory process over frequency ranges. Third, a multivariate wavelet-based estimator of memory parameters was developed to reduce the deterioration of estimation performance in the presence of additive noises. It was proved, through simulation studies, that the multivariate estimator is more resilient to additive noises than other univariate estimators are. This robust estimator of memory parameters is instrumental in obtaining more precise estimates of nonfractal connectivity and fractal connectivity since the connectivity estimator requires estimating memory parameters beforehand.

These fractal-based analysis techniques were tested for the analyses of both human and animal fMRI data taken at rest in order to verify their usefulness in neuroscientific and medical applications (see Chapter 5). The human brain studies focused on the comparison of functional connectivity between depressive patients and healthy subjects while the rat brain studies focused on observing the temporal evolution in functional connectivity between pre-stimulation resting state and post-stimulation resting state. The experimental results show that both nonfractal connectivity and fractal connectivity are useful to discover the between-group difference and intrinsic patterns in statistical properties of a func-

tional brain network.

This paper is organized as follows. Chapter 2 contains the background theories underlying this thesis. It includes hemodynamic models, neural field model, functional connectivity and information flow, graph theoretical metrics, wavelet theory, and long memory process models. Chapter 3 introduces the long memory model of hemodynamic response along with its theoretical inferences on the relation of long memory on functional connectivity. In Chapter 4, wavelet-based estimators of nonfractal connectivity and fractal connectivity are proposed, and their performance is evaluated through simulation studies. Also, a multivariate wavelet-based estimator of memory parameter is introduced. Chapter 5 introduces the applications of fractal-based connectivity analyses on both human and animal brains. In Chapter 6, all results are summarized and discussed with advanced issues and future works.

Chapter 2

Background

2.1 Hemondynamic models

this section introduces two major hemodynamic models that describe the coupling of neuronal activities with BOLD signals: one is a linear convolution model called the hemodynamic response function (HRF), and the other is the Balloon-Windkessel model that consists of hemodynamic state equations related to blood flow, blood volume, and deoxyhemoglobin level.

2.1.1 Hemodynamic response function

A BOLD response to a single stimulation can be typically modeled as the linear convolution of neuronal activity with the *hemodynamic response function* (HRF). It has been shown that the impulse BOLD response has different shape according to brain regions and subjects. This variability can be effectively expressed in terms of the HRF. In the general linear model (GLM) of fMRI, a BOLD signal $x(t)$ is represented by

$$y(t) = X(t)\beta + \varepsilon(t) \tag{2.1}$$

where β is a vector of parameters, $X(t)$ is a design matrix which represents the predicted BOLD response to neuronal activity $\mathbf{u}(t)$, and $\varepsilon(t)$ is a white Gaussian noise with variance σ^2 (Friston et al., 1994). The predicted BOLD signal $x(t)$ is primarily regarded as an output of the nonlinear cerebral hemodynamic system.

One simplified assumption is that the hemodynamic system can be approximated as a linear time-invariant (LTI) system. In this case, $X(t)$ is described as the linear convolution of neuronal activity $u(t)$ with HRF $g(t)$ by

$$x(t) = \sum_{\tau=0}^{\infty} g(\tau)u(t - \tau). \qquad (2.2)$$

In the classical HRF model, $g(t)$ can be given as the combination of two Gamma functions

$$g_{(e)}(t) = \left(\frac{t}{s_1}\right)^{r_1} e^{-(t-s_1)/b_1} - c\left(\frac{t}{s_2}\right)^{r_2} e^{-(t-s_2)/b_2} \qquad (2.3)$$

where $\{s_1, s_2, r_1, r_2, b_1, b_2\}$ is a set of constants that determines the form of HRF curve (Henson & Friston, 2006). This HRF can be approximately viewed as a low pass filter (LPF) as shown in Figure 3.3. One important consideration regarding the HRF is that it does not reflect nonlinearity of hemodynamic system. The HRF can be generalized to allow nonlinearity through the Volterra series expansion. The nonlinear representation of hemodynamic response will be discussed in Section 3.4.

2.1.2 Biophysical model

The hemodynamic response function has been widely used to regress a task-activated BOLD signal with neuronal activity. On the other hand, the other parsimonious model, called the *Balloon-Windkessel model*, can be considered (Buxton et al., 1998; Mandeville et al., 1999). While the Volterra series representation of nonlinear dynamics is model-independent, the model describes a nonlinear hemodynamic system with intrinsic variables such as deoxyhemoglobin content, blood flow (CBF), and blood volume (CBV). It describes the nonlinear dynamics of blood oxygenation and volume which directly affect BOLD signals in fMRI. In this model, the evolution of blood volume and deoxyhemoglobin content is dependent on blood flow. Suppose that the CBF is a linear transform of neuronal activity even though its mechanism has not been perfectly understood. Then, the Balloon model can be combined with neurovascular state equations that represent the change in regional cerebral blood flow (rCBF) linearly coupled

with neuronal activity (Buxton et al., 2004; Friston et al., 2000; Mechelli et al., 2001). Finally, the hemodynamic model consists of the Balloon model and the neurovascular state equation.

Let u_n be a discrete time function of neuronal activity $u(t)$ measured at time $t = n\tau$ where $0 \leq n \leq N$ and τ denotes the sampling period; that is, $u_n = u(n\tau)$. The corresponding BOLD signal change relative to resting signal is taken by

$$y_n \approx V_0 \left[k_1 \left(1 - q_n \right) + k_2 \left(1 - \frac{q_n}{v_n} \right) + k_3 \left(1 - v_n \right) \right] \tag{2.4}$$

where $q(t)$ and $v(t)$ denote venous blood volume and total deoxyhemoglobin content, V_0 is the resting blood volume, and k_1, k_2, k_3 are coefficients (Friston et al., 2000). Let the discrete derivative of y_n be denoted by $D_\tau y_n := (y_n - y_{n-1})/\tau$. Then, the hemodynamic state is fully described by the following nonlinear differential equations with respect to vasodilatory signal (s), blood inflow (f) along with v and q.

$$D_\tau s_{n+1} = \epsilon x_n - \kappa s_n - \gamma \left(f_n - 1 \right) \tag{2.5}$$

$$D_\tau f_{n+1} = s_n \tag{2.6}$$

$$\tau_0 D_\tau v_{n+1} = f_n - v_n^{1/\alpha} \tag{2.7}$$

$$\tau_0 D_\tau q_{n+1} = f_n \frac{1 - (1 - E_0)^{1/f_n}}{E_0} - q_n v_n^{1/\alpha - 1} \tag{2.8}$$

In these equations, ϵ, $\kappa = 1/\tau_s$, $\gamma = 1/\tau_f$, τ_0, α, and E_0 denote the neuronal efficacy, signal decay rate, autoregulation rate, transit time, stiffness parameter, and resting oxygen extraction respectively (Friston et al., 2000). The seven intrinsic parameters $p = \{\epsilon, \tau_s, \tau_f, \tau_0, \alpha, E_0, V_0\}$ determine the properties of hemodynamic response. While the equations (2.7) and (2.8) constitute the classical Balloon model, (2.5) and (2.6) compose of the neurovascular state equations that can be reduced to

$$D_\tau s_{n+1} = -\kappa s_n - \tau \gamma \sum_{j=1}^{n-1} s_{n-j} + (\gamma + \epsilon x_n). \tag{2.9}$$

2.2 Large-scale neuronal dynamics

It is instrumental to understand the dynamics of endogenous neuronal processing underlying resting state BOLD signals. Since the fMRI is a macroscopic noninvasive measurement of brain activity, the BOLD signals would reflect the activity of neuronal population. However, it is difficult to figure out the dynamics of neuronal population since its space is high dimensional. The complexity of population activity can be reduced by considering the probabilistic evolution of representative variables such as the mean firing rate. Modeling the neuronal population is beneficial to figure out the properties of functional interaction among neuronal populations hidden behind the corresponding BOLD signals even though the exact relationship between neural activity and BOLD signal is still unclear. In this section, both a simple model for a single neuron and a neuronal population model, called the *stochastic neural field model*, is briefly introduced.

Single neuron model

The most representative spiking model for a single neuron is the Hodgkin-Huxley model (Hodgkin & Huxley, 1952). Since it is computationally too expensive to be simulated, Izhikevich (2003) suggested a two-dimensional model of spiking neurons based on the bifurcation theories. This model is described by two ordinary differential equations

$$\frac{d\mathbf{v}}{dt} = 0.04\mathbf{v}^2 + 5\mathbf{v} + 140 - \mathbf{u} + I \tag{2.10}$$

$$\frac{d\mathbf{u}}{dt} = a(b\mathbf{v} - \mathbf{u}) \tag{2.11}$$

with the auxiliary after-spike resetting

$$\text{if } v_i \geq 30\text{mV, then } \begin{cases} v_i \leftarrow c \\ u_i \leftarrow u_i + d \end{cases} \tag{2.12}$$

where $\mathbf{v}$ and $\mathbf{u}$ represent respectively the membrane potentials of neurons and membrane recovery variables related to ionic currents. All variables are listed in the table 2.1.

Table 2.1: Parameters of the Izhikevich's neuronal model.

Parameter	Description
v_i	Membrane potential of the ith neuron
u_i	Membrane recovery variable of the ith neuron
I	Ion current
I_{in}	Random thalamic input
I_{sync}	Sum of inputs from fired neighbors
g	Maximum synaptic current
a	Time scale of u
b	Sensitivity of u to the subthreshold fluctuation of v
c	After-spike reset value of v
d	After-spike reset value of u

The synaptic current I is the combination of random thalamic input and internal inputs from neighbors; i.e.,

$$I = I_{in} + I_{sync}. \tag{2.13}$$

The thalamic input I_{in} is activated in a randomly-chosen neuron at each time point, and I_{sync} of the i-th neuron is computed by

$$I_{sync}(i) = g \sum_{j=1}^{n} s_{i,j} \mathbf{1}_{v_j \geq 30} \tag{2.14}$$

where g is the maximum synaptic strength, and $s_{i,j}$ is the binary connection between neuron i and j which is defined in the structural connectivity matrix S. An example of simulated neuronal spike trains are shown in Fig. 2.1.

The maximum synaptic strength g is related to the strength of influence of a neuron on connected neighbor neurons; as g increases, a neuron is more affected by other neurons from (2.14), and spike trains of a neuron are more synchronized with connected neighbors. On the other hand, the thalamic input I_{in} is related to the frequency of spikes. The increase in the thalamic input results in the increase of frequency of spike trains.
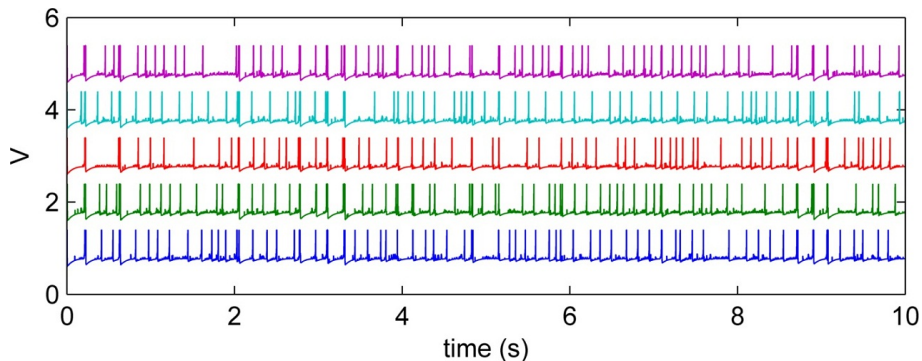
Figure 2.1: The membrane potentials of five neurons simulated from the Izhikevich's model.

Dynamic causal modeling

A simple way of dealing with neuronal population activities is to exploit dynamic causal modeling (DCM) (Friston et al., 2003; Stephan et al., 2008). The DCM describes how neuronal populations dynamically interact with each other by using a bilinear approximation. Let us consider a brain network consisting of N regions where $\mathbf{x}(t) := [x_1(t), \cdots, x_N(t)]^T$ denote neuronal population activity states at a time t. $\mathbf{x}(t)$ is primarily given based on dynamic causal modelling (DCM) by

$$\dot{\mathbf{x}}(t) := F\left(\mathbf{x}(t), \mathbf{u}(t), \theta_c\right) \tag{2.15}$$

where F is a nonlinear function, $\mathbf{u}(t) := [u_1(t), \cdots, u_M(t)]^T$ is a set of M inputs, and θ_c denotes the coupling parameters. This model can be approximated by a bilinear form

$$\dot{\mathbf{x}}(t) \approx \left(\mathbf{A} + \sum_{j=1}^{M} u_j(t)\mathbf{B}_j\right)\mathbf{x}(t) + \mathbf{C}\mathbf{u}(t) \tag{2.16}$$

where $\mathbf{A}$ describes the structural connectivity matrix, the matrix $\mathbf{B}_j$ represents the indirect variation in coupling triggered by the jth input, and the matrix $\mathbf{C}$ substantiates the direct impact of inputs on neuronal dynamics. The parameter $\theta_c = \{\mathbf{A}, \mathbf{B}_1, \cdots, \mathbf{B}_M, \mathbf{C}\}$ fully describes functional dynamics of neuronal population activities in a given network.

The model was primarily built to describe effective connectivity of neuronal

activities in evoked state of the brain where external inputs lead to changes in neuronal dynamics. On the other hand, the resting state neuronal activities no longer depend on external stimulations; instead, they are governed by self-imposed sources of the brain. Thus, $\mathbf{u}(t)$ is regarded as intrinsic inputs in resting state. Notice that $\mathbf{A}$ is homogeneous both in evoked state and in resting state, but $\mathbf{B}_j$ and $\mathbf{C}$ in resting state may not be identical with those of evoked state.

Even though the coupling parameters in resting state are unknown due to its complexity, it is valuable to simplify the model of resting state neuronal activities since it will enable us to figure out the relationship between structural and functional connectivity. First, it can be assumed that each region has its own spontaneous input, and is not influenced by other intrinsic inputs; it results in $N = M$, $\mathbf{B}_j = 0$ and $\mathbf{C} = \mathbf{I}$. Second, the intrinsic input $u_j(t)$ in the jth region can be modeled as a Gaussian process. As a result, we obtain a first-order differential model of resting state neuronal activities as follows

$$\dot{\mathbf{x}}(t) \approx \mathbf{A}\mathbf{x}(t) + \mathbf{u}(t). \tag{2.17}$$

This model produces a sequence of neuronal activities whose rate exhibits Gaussian distribution. According to the Langevin equation (see Appendix A.1), the increment process of $\mathbf{x}(t)$ is approximately a multivariate Brownian motion. The spectral density of $\mathbf{x}(t)$ is given by

$$\mathbf{X}(f) = \left(|\mathbf{A} + \mathbf{i}f\mathbf{I}|^2 \right)^{-1} \mathbf{U}(f). \tag{2.18}$$

Neural field theory

The neural field theory builds a mathematical model for populations of neurons and describes the stochastic properties of their synaptic or firing rate activity (Amari, 1975, 1977; Jirsa & Haken, 1996, 1997; Nunez, 1974; Wilson & Cowan, 1972, 1973). Therefore, it is more biophysically plaugible than the DCM (Daunizeau et al., 2011). Here, the neural field model is reviewed by focusing on studies by Bressloff (2009).

Let us consider a brain network consisting of N homogeneous populations where all neurons in a population are synaptically connected each other. Let

$n_j(t)$ denote the number of active neurons in population j at time t. The state of population activities in the brain network is specified by $\mathbf{x}(t) = [x_j(t)]_{j=1,\cdots,N}^T$ where $x_j(t) = n_j(t)/M_j$ where M_j denotes the number of neurons in population j. The neuronal activity of one population is influenced by other populations via synaptic currents. Let $I_j(t)$ denote total synaptic current flowing into the jth population from other populations. Then, it satisfies

$$I_j(t) = \sum_{i=1}^{N} W_{j,i} \int_0^\infty \epsilon(\tau)x_i(t-\tau)d\tau + I_j^{ext}(t) \tag{2.19}$$

where $W_{j,i} \in \mathbb{R}$ denotes a (directional) connectivity coefficient from the ith neuron to jth neuron, $I_j^{ext}(t)$ is an external input to population j, and $\epsilon(t)$ denotes the postsynaptic response function given by $\epsilon(t) = -\tau_\epsilon^{-1}e^{-t/\tau_\epsilon}$. We set $I_j^{ext}(t) = 0$ since the brain network is supposed to be in resting state which has no external inputs. The brain network is said to have the (weighted) *structural connectivity* $\mathbf{W} := [W_{i,j}]_{i,j=1,\cdots,N}$.

Let f denote a gain function between population activity and synaptic current, $x_j(t) = f(I_j(t))$, and suppose that f is a positive and monotonically increasing function. Provided that τ_ϵ is large, the equation (2.19) is equivalent to the following equation (Refer the appendix A.1 for proofs.)

$$\tau_c \frac{\mathrm{d}x_j(t)}{\mathrm{d}t} = -x_j(t) + f\left(\sum_{i=1}^{N} W_{j,i}x_i(t)\right). \tag{2.20}$$

Since this equation does not describe stochastic dynamics of population activity, we consider the probability distribution of population activities. Let $P(\mathbf{n}, t)$ be the time-dependent probability distribution of $\mathbf{n}(t) := [n_i(t)]_{i=1,\cdots,N}^T$. $n_j(t)$ can be regarded as a stochastic one-step process as a special type of Markov processes. Hence, the probability distribution $P(\mathbf{n}, t)$ evolves according to the following nonlinar master equation

$$\begin{aligned}
\tau_c \frac{\partial P(\mathbf{n}, t)}{\partial t} &= \sum_{i=1}^{N} \left[(\mathbb{E}_i^+ - 1)\left(T_i^-(\mathbf{n})P(\mathbf{n}, t)\right) \right. \\
&\quad \left. + (\mathbb{E}_i^- - 1)\left(T_i^+(\mathbf{n})P(\mathbf{n}, t)\right) \right]
\end{aligned} \tag{2.21}$$

where $\mathbb{E}^{\pm} f(n_i) = f(n_i \pm 1)$, and $T_i^{\pm}(\mathbf{n})$ denote the transition rates where $T_i^-(\mathbf{n}) = \alpha_i n_i$ and $T_i^+(\mathbf{n}) = M_i f\left(\sum_{j=1}^N W_{i,j} n_j / M_j\right)$. (Refer to Appendix A.2 for details.)

Let us define a *fluctuation process* $\xi_i(t)$ of population i where $\xi_i^2(t) \doteq \mathrm{var}(x_i(t))/M_i$. In this case, $P(\mathbf{x}, t)$ can be described as a function of ξ, $P(\mathbf{x}, t) := \Pi(\xi, t)$. Through Kramer-Moyal expansion of the master equation (2.21) and its linear approximation, we obtain the linear multivariate Fokker-Planck equation given by

$$
\begin{aligned}
\tau_c \frac{\partial \Pi(\xi, t)}{\partial t} &= -\sum_{i=1}^N \sum_{k=1}^N A_{i,k}(\bar{\mathbf{x}}) \frac{\partial}{\partial \xi_i}[\xi_k \Pi(\xi, t)] \\
&\quad + \frac{1}{2}\sum_{i=1}^N B_i(\bar{\mathbf{x}}) \frac{\partial^2}{\partial \xi_i^2} \Pi(\xi, t)
\end{aligned} \tag{2.22}
$$

where $\bar{\mathbf{x}}(t) := E[\mathbf{x}(t)]$. (Refer to the appendix A.3 for proofs.) The drift function $A_{i,k}$ and the diffusion function B_i are given by

$$
A_{i,k}(\bar{\mathbf{x}}) := \frac{\partial}{\partial \bar{x}_k}\left(\Omega_{i,1}(\bar{\mathbf{x}}) - \Omega_{i,-1}(\bar{\mathbf{x}})\right), \tag{2.23}
$$

$$
B_i(\bar{\mathbf{x}}) := \Omega_{i,1}(\bar{\mathbf{x}}) + \Omega_{i,-1}(\bar{\mathbf{x}}) \tag{2.24}
$$

where $\Omega_{i,-1}(\bar{\mathbf{x}}) = \alpha_i \bar{x}_i$ and $\Omega_{i,1}(\bar{\mathbf{x}}) = f\left(\sum_{j=1}^N W_{i,j}\bar{x}_j\right)$ denote transition rates.

Let $\Xi_{i,j}(t, \tau) := \mathrm{cov}(\xi_i(t), \xi_j(t+\tau))$ be the cross-covariance function of $\xi_i(t)$ and $\xi_j(t)$. The first-order differential equation for $\Xi_0(t) := \Xi_{i,j}(t, 0)$ is obtained from the equation (2.22) as

$$
\begin{aligned}
\tau_c \frac{\partial \Xi_0(t)}{\partial t} &= \tau_c \int_{-\infty}^{\infty} \xi(t)^T \xi(t) \frac{\partial \Pi(\xi, t)}{\partial t} \mathrm{d}\xi \\
&\approx \mathbf{A}(\bar{\mathbf{x}})\Xi_0(t) + \Xi_0(t)\mathbf{A}^T(\bar{\mathbf{x}}) + \mathbf{B}(\bar{\mathbf{x}})
\end{aligned} \tag{2.25}
$$

where $\mathbf{A} := [A_{i,j}]_{i,j=1,\cdots,N}$ and $\mathbf{B} = \mathrm{diag}(B_1, \cdots, B_N)$. Suppose that $\mathbf{x}(t)$ is in *steady state*; in other words, $\bar{\mathbf{x}}(t)$ is constant over time and $\xi(t)$ is a stationary process. In this case, $\Xi_0(t)$ is also invariable and satisfies the following condition

$$
\Xi_0(t) = \Xi_0 = \mathbf{A}^{-1}(\bar{\mathbf{x}})\mathbf{B}(\bar{\mathbf{x}})/2. \tag{2.26}
$$

Fractal-rate neuronal activities

Previous studies have turned out that neuronal spike trains in some area of the brain tend to exhibit long-range autocorrelation and self-similarity which results in the $1/f$-type power spectrum. Such a phenomenon can be represented by fratals. A sequence of fractal-rate action potentials can be modelled as a fractal-shot-noise-driven point process (FSNDP) which is a type of doubly stochastic point process driven by fractal shot noise defined by $\phi_i(t; \beta_i) := bt^{-\beta_i}$ with a constant b (Lowen & Teich, 1991, 2005).

2.3 Connectivity and information flow

2.3.1 Functional connectivity

Pearson correlation Let $x_1(t)$ and $x_2(t)$ be stochastic processes where $\mathbb{E}[x_1(t)] = \mu_1$ and $\mathbb{E}[x_2(t)] = \mu_2$. Then, $\text{cov}[x_1(t), x_2(t)]$, the covariance of $x_1(t)$ and $x_2(t)$ is given by (2.63). Then, the correlation of $x_1(t)$ and $x_2(t)$ is defined by

$$\rho_{1,2} \doteq \frac{\text{cov}[x_1(t), x_2(t)]}{(\text{var}[x_1(t)] \cdot \text{var}[x_1(t)])^{1/2}} \tag{2.27}$$

Partial correlation Pearson correlation provides information on similarity between two time series over scales, but these measures do not effectively eliminate the influences from other time series. On the other hand, partial correlation measures the conditional relationship between two random variables while controlling a set of other random variables; in other words, the conditional independence of $x_1(t)$ and $x_2(t)$ given $\mathbf{y}(t) = [y_1, ..., y_p]$ (Baba et al., 2004). Let us define the partial covariance matrix for $\mathbf{X} = (X_1, X_2)$ as follows

$$\Sigma_{\mathbf{XX \cdot Y}} = \begin{bmatrix} \sigma_{11 \cdot \mathbf{Y}} & \sigma_{12 \cdot \mathbf{Y}} \\ \sigma_{21 \cdot \mathbf{Y}} & \sigma_{22 \cdot \mathbf{Y}} \end{bmatrix} \tag{2.28}$$

such that $\Sigma_{\mathbf{XX \cdot Y}} = \Sigma_{\mathbf{XX}} - \Sigma_{\mathbf{XY}}\Sigma_{\mathbf{YY}}^{-1}\Sigma_{\mathbf{YX}}$ where $\Sigma_{\mathbf{XX}}$ is 2×2, $\Sigma_{\mathbf{XY}}$ is $2 \times p$, $\Sigma_{\mathbf{YY}}$ is $p \times p$ covariance matrix. Then, the partial correlation is defined as

$$\rho_{12 \cdot \mathbf{Y}} = \frac{\sigma_{12 \cdot \mathbf{Y}}}{\sqrt{\sigma_{11 \cdot \mathbf{Y}}\sigma_{22 \cdot \mathbf{Y}}}}. \tag{2.29}$$

2.3.2 Information flow

Remarkable advances have been made in the field of information theory, and also applied to capture the information flow in the brain network (Hinrichs et al., 2006, 2008). In this section, some useful information theoretical methodologies such as mutual information and transfer entropy are introduced. Let x_t and y_t be discrete random variable with probability distributions $p(x_t) = f_X(x_t)$ and $p(y_t) = f_Y(y_t)$. the *Shannon entropy* is defined as

$$H(x_t) = \sum_{x_t \in \mathcal{A}} p(x_t) \log \frac{1}{p(x_t)} \tag{2.30}$$

where $\mathcal{A}$ is the state space of x_t (Shannon & Weaver, 1949). Let $q(x_t)$ be a prior estimate of $p(x_t)$. then, the error of using $q(x_t)$ comparing with the true $p(x_t)$ can be measured by the *Kullback entropy*

$$K_{p|q}(x_t) = \sum_{x_t \in \mathcal{A}} p(x_t) \log \frac{p(x_t)}{q(x_t)} \tag{2.31}$$

(Jumarie, 1990; Kullback, 1968). Let us consider a bivariate process consisting of x_t and y_t. Suppose that x_t and y_t are statistically independent, and $q(x_t, y_t) = p(x_t)p(y_t)$. Then, the *mutual information* between x_t and y_t can be defined from (2.31) as follows

$$M(x_t, y_t) = \sum_{x_t \in \mathcal{A}} \sum_{y_t \in \mathcal{A}} p(x_t, y_t) \log \frac{p(x_t, y_t)}{p(x_t)p(y_t)} \tag{2.32}$$

(Cover & Thomas, 2006; Jumarie, 1990). It can be re-expressed in terms of the Shannon entropy in (2.30) by

$$M(x_t, y_t) = H(x_t) + H(y_t) - H(x_t, y_t). \tag{2.33}$$

17

In (2.33), the mutual information is symmetric and undirectional. Let $\mathbf{x}_t^{(k)}$ be a set of k past variables such that $\mathbf{x}_t^{(k)} = \{x_t, \cdots, x_{t-k+1}\}$. Suppose that the future state x_{t_1+1} and y_{t_2+1} is dependent on the k past states $\mathbf{x}_{t_1}^{(k)}$ and $\mathbf{y}_{t_2}^{(l)}$. The *conditional mutual information* can be given by

$$
\left(x_{t_1+1}, y_{t_2+1} | \mathbf{x}_{t_1}^{(k)}, \mathbf{y}_{t_2}^{(l)} \right) = \sum_{x_{t+1} \in \mathcal{A}} \sum_{\mathbf{x}_{t_1}^{(k)} \in \mathcal{A}^k} \sum_{y_{t+1} \in \mathcal{A}} \sum_{\mathbf{y}_{t_2}^{(l)} \in \mathcal{A}^k} p(x_{t_1+1}, \mathbf{x}_{t_1}^{(k)}, y_{t_2+1}, \mathbf{y}_{t_2}^{(l)})
$$

$$
\log \frac{p\left(x_{t_1+1}, y_{t_2+1} | \mathbf{x}_{t_1}^{(k)}, \mathbf{y}_{t_2}^{(l)} \right)}{p\left(x_{t_1+1} | \mathbf{x}_{t_1}^{(k)} \right) p\left(y_{t_2+1} | \mathbf{y}_{t_2}^{(l)} \right)} \tag{2.34}
$$

(Cover & Thomas, 2006; Jumarie, 1990). Howver, it does not provide any inference on directional information flow. Let $\mathbf{x}_t^{(k)}$ be a set of k past variables such that $\mathbf{x}_t^{(k)} = \{x_t, \cdots, x_{t-k+1}\}$. Suppose that the future state x_{t+1} is dependent just on the k past states $\mathbf{x}_t^{(k)}$ and independent of $\mathbf{y}_t^{(l)}$. Then, $p(x_{t_1+1} | \mathbf{x}_{t_1}^{(k)}, \mathbf{y}_{t_2}^{(l)}) = p(x_{t_1+1} | \mathbf{x}_{t_1}^{(k)})$. Then, the *transfer entropy* can be defined as follows

$$
T(X_{t_1+1} | \mathbf{x}_{t_1}^{(k)}, \mathbf{y}_{t_2}^{(l)}) = \sum_{x_{t+1} \in \mathcal{A}} \sum_{\mathbf{x}_{t_1}^{(k)} \in \mathcal{A}^k} \sum_{\mathbf{y}_{t_2}^{(l)} \in \mathcal{A}^k} p(x_{t_1+1}, \mathbf{x}_{t_1}^{(k)}, \mathbf{y}_{t_2}^{(l)}) \log \frac{p\left(x_{t_1+1}, | \mathbf{x}_{t_1}^{(k)}, \mathbf{y}_{t_2}^{(l)} \right)}{p\left(x_{t_1+1} | \mathbf{x}_{t_1}^{(k)} \right)}.
$$

$$\tag{2.35}$$

The transfer entropy in (2.35) is not symmetric and describes the directionaly transformation of information (Kaiser & Schreiber, 2002; Schreiber, 2000).

2.4 Graph theory

While the neuronal population model discussed in Section 2.2 is the best tool to analyze temporal evolution of dynamic states, the graph theory is an effective approach to understand the topology of complex brain networks. The functional network of the brain can be modeled as directed or undirected graphs which consist of nodes and edges. Note that a brain network tends to have small-world properties, that is, high clustering with a short path length (Bullmore et al., 2009; Bullmore & Sporns, 2009; Sporns, 2011). It has been shown that

a resting state network also exhibits small-worldness (Achard et al., 2006). In this section, a basic concept and metrics, which are necessary to analyze a brain network, is introduced. For a generic overview of graph theoretical analysis, refer to (Bullmore & Sporns, 2009).

Graph representation A network is defined by vertices and edges. In a network $G = (V, E)$ where V and E denote *vertices* and *edges* respectively, let N_e be the number of all possible edges, and n_e be the number of edges in the network G. The *density of connections* in the random network is defined by $D(G) = n_v/N_v$. If $D(G) = 1$, the network is said to be *fully connected* while if $D(G) < 1$ the network is said to be *partly connected*. A random network is supposed to have spatially homogeneous density of connections. Unlike the random network, a modular small-world network consists of in-module connections and between-module connections (sometimes called shortcuts). Each module can be fully or partly connected in a similar way with random networks.

Two types of network topology are illustrated in Figure 2.2; one is a random network with the specified number of nodes and density of connections, and the other is a modular small-world network that contains several partly-connected (or fully-connected) modules with randomly distributed between-module connections. The network structure can be fully described by a *structural connectivity matrix*.

Network measures The *degree* of node i is defined as the number of other nodes connected to the node as follows

$$k_i = \sum_{j \in V} e_{ij} \tag{2.36}$$

where $e_{ij} \in \{0, 1\}$ denotes the binary edge connecting between node i and node j. If $e_{ij} \in \mathbb{R}$, k_i is called the *weighted degree* of node i or the *node strength*. The *shortest path length* between node i and node j is the minimum number of edges

(a)

(b)

(c)

(d)
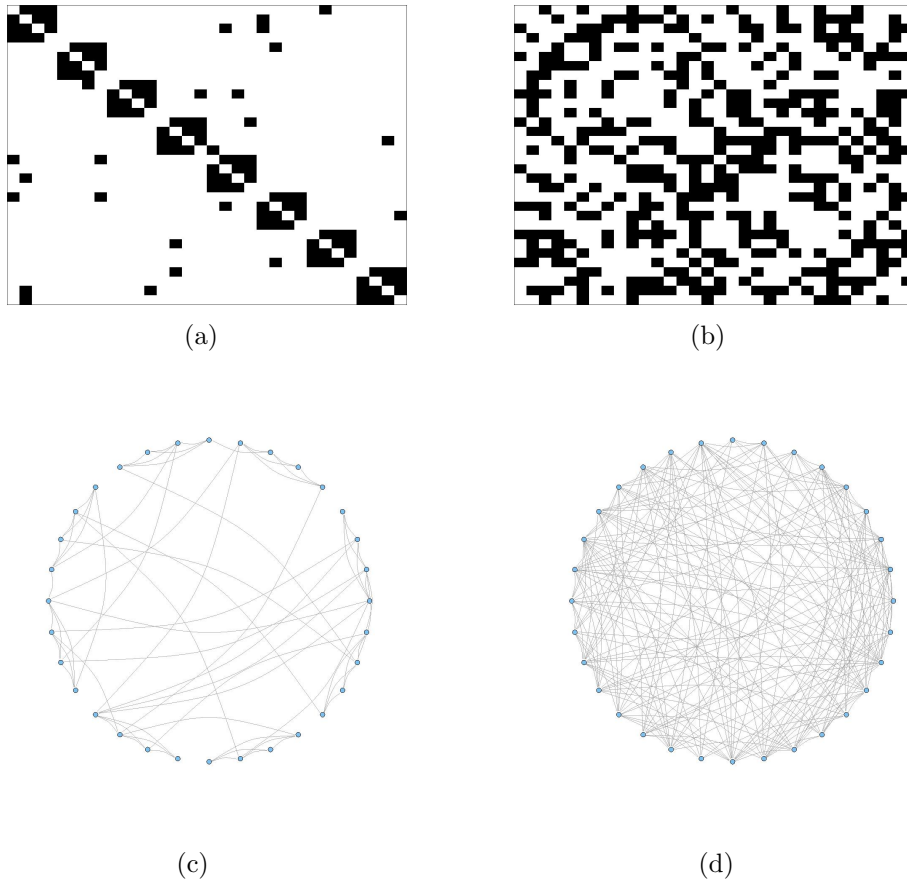
Figure 2.2: Illustrations of network topologies and structural connectivity matrices; (a) a modular small-world network which consists of partly-connected modules, and (b) a randomly distributed network. (c) and (d) are the visualizations of network topology corresponding to these networks.

passing to travel from node i to node j.

$$d_{ij} = \sum_{e_{uv} \in E_{i \leftrightarrow j}} e_{uv} \tag{2.37}$$

where $E_{i \leftrightarrow j}$ denotes the set of all edges included in the shortest path between node i and node j. Especially, the *characteristic path length* of the network G can be defined as a global metric:

$$L \doteq \frac{1}{n_v} \sum_{i \in V} L_i = \frac{1}{n_v(n_v - 1)} \sum_{i \in V} \sum_{j \in V, j \neq i} d_{ij} \tag{2.38}$$

20

where L_i is the mean shortest path length between node i and other nodes (Watts & Strogatz, 1998). The *global efficiency* of the network G is regarded as the average of the inverse (shortest) path length matrix as follows:

$$E = \frac{1}{n_v} \sum_{i \in V} E_i = \frac{1}{n_v(n_v - 1)} \sum_{i \in V} \sum_{j \in V, j \neq i} d_{ij}^{-1} \tag{2.39}$$

where E_i denotes the efficiency of the individual node i. A network with full edges has the maximum of global efficiency while a network with no edge has the minimum of global efficiency (Latora & Marchiori, 2001). Therefore, either low characteristic path length or high efficiency can be interpreted that nodes interact fast through short routes. The *clustering coefficient* of the network G (Watts & Strogatz, 1998) is a metric to quantifies the density of edges connecting neighbors normalized by the number of all possible connections as defined by

$$C = \frac{1}{n_v} \sum_{i \in V} C_i = \frac{1}{n_v} \sum_{i \in V} \frac{2t_i}{k_i(k_i - 1)} \tag{2.40}$$

where C_i is the clustering coefficient of node i, and t_i is the number of triangles around the node i

$$t_i \doteq \frac{1}{2} \sum_{j,h \in V} e_{ij} e_{ih} e_{jh}. \tag{2.41}$$

Let ρ_{hj} be the number of all shortest paths between node h and node j, and $\rho_{hj}(i)$ be the number of shortest paths between node h and node j that go through node i. Then, the *betweenness centrality* of node i is defined as follows

$$b_i = \frac{1}{(n_v - 1)(n_v - 2)} \sum_{h,j \in V} \frac{\rho_{hj}(i)}{\rho_{hj}}. \tag{2.42}$$

Hence, the betweenness centrality of a node means the density of shortest paths passing through the node (Freeman, 1978). A node with high betweenness centrality is expected to act as a hub controlling information flow. The *participation coefficient* of node i reflects the degree of contribution to interconnection between

modules (Newman, 2004), and is given by

$$y_i \doteq 1 - \sum_{m \in \mathcal{M}} \left(\frac{k_i(m)}{k_i} \right)^2 \tag{2.43}$$

where $\mathcal{M}$ denotes the set of all modules, and $k_i(m)$ is the number of edges between node i and all other nodes included in module m (Guimera & Amaral, 2005). A node with low participation coefficient tends to facilitate modular segregation while a node with high participation coefficient tends to promote interaction between modules. Lastly, how these network metrics are helpful to assess the topology of a network. For instance, a small-world network is defined as a network with high clustering and short path length similar with a random network (Watts & Strogatz, 1998). To measure how a network is close to the small-world topology, the small-worldness of a network G can be defined as

$$S = \frac{C/C_{\mathrm{rand}}}{L/L_{\mathrm{rand}}} \tag{2.44}$$

where C_{rand} and L_{rand} denote the clustering coefficient and characteristic path length of a random network (Humphries & Gurney, 2008). Among the above metrics, degree, shortest path length, betweenness centrality, and participation coefficient can be classified as local metrics. On the other hand, the characteristic path length, global efficiency, clustering coefficient, small-worldness can be regarded as global metrics. For more network metrics, refer to (Rubinov & Sporns, 2010; Sporns, 2011).

2.5 Wavelet-based analysis

The wavelet enables the variance of a time series to be decomposed over several scales. Especially, the wavelet is the natural tool to analyze the fractal property of a long memory process; in other words, it is appropriate to reveal scale-invariance (Bullmore et al., 2004; Vidakovic, 2009; Wornell, 1996, 1993). Therefore, the wavelets are useful to estimate the fractal parameter of a long memory process. this section provides a basic description of wavelet theories.

Definition 1 (Wavelet and scaling filters)**.** Let a sequence $\{h(l) : l = 0, \cdots, L-1\}$ satisfy the following condition

a) $h(l) \neq 0,\ h(L-1) \neq 0$

b) $\displaystyle\sum_{l=0}^{L-1} h(l) = 0,\ \sum_{l=0}^{L-1} h(l)^2 = 1$

c) $\displaystyle\sum_{l=0}^{L-1} h(l)h(l+2n) = \sum_{l=-\infty}^{\infty} h(l)h(l+2n) = 0,\ \ \forall n \in \mathbb{Z}.$

Also, $\{g(l)\}$ is a sequence satisfying

$$g(l) = (-1)^{l+1} h(L-1-l). \tag{2.45}$$

Then, $\{h(l)\}$ is called the *wavelet filter* of length L, and $\{g(l)\}$ the *scaling filter* corresponding to $\{h(l)\}$.

Definition 2 (Wavelet and scaling coefficients)**.** Let $h_j(l)$ and $g_j(l)$ be the dilated filters of length $2^{j-1}(L-1)+1$ defined by

$$h_j(l) = \begin{cases} h(l/2^{j-1}) & \text{if } l/2^{j-1} \in \{0, \cdots, L-1\} \\ 0 & \text{otherwise} \end{cases},\ \ \forall j \in \mathbb{N}. \tag{2.46}$$

For example, $\{h_2(l)\} = \{h(0), 0, h(1), \cdots, 0, h(L-1)\}$. $g_j(l)$ is also defined in the same manner. Let $x(t)$ be a real-valued discrete time process. Then, the jth level *wavelet coefficients* $W_j(t)$ and *scaling coefficients* $V_j(t)$ of $x(t)$ are defined by

$$W_j(t) = \sum_{l=0}^{L_j-1} h_j(l) x\left(2^j(t+1) - 1 - l\right), \tag{2.47}$$

$$V_j(t) = \sum_{l=0}^{L_j-1} g_j(l) x\left(2^j(t+1) - 1 - l\right), \tag{2.48}$$

where $L_j = (2^j - 1)(L-1) + 1$.

Remark 1. Let $\lambda_N \doteq 1/(2\Delta t)$ for the sample interval Δt denotes the Nyquist frequency. The wavelet filter $h_j(l)$ can be regarded as the approximate band-pass

filter with pass band $|\lambda| \leq \lambda_{\mathbb{N}}/2^{j+1}$ while the scaling filter $g_j(l)$ can be regarded as the low-pass filter with pass band $\lambda_{\mathbb{N}}/2^{j+1} \leq |\lambda| \leq \lambda_{\mathbb{N}}/2^j$.

Definition 3 (Transfer function and squared gain function)**.** Let $H(\lambda)$ be given by

$$H(\lambda) \doteq \sum_{l=-\infty}^{\infty} h(l)e^{-i2\pi\lambda l}. \tag{2.49}$$

Then, $H(\lambda)$ is called the transfer function of $\{h(l)\}$, and the squared gain function of $\{h(l)\}$ is defined by

$$\mathcal{H}(\lambda) \doteq |H(\lambda)|^2. \tag{2.50}$$

$G(\lambda)$ and $\mathcal{G}(\lambda)$ also denote the transfer function and squared gain function of $\{g(l)\}$.

Lemma 1 (Between-scale wavelet covariance)**.** *Let $x_1^{(L)}(t)$ and $x_2^{(L)}(t)$ be weakly stationary stochastic processes. Let $W_j^{(1)}(t)$ and $W_j^{(2)}(t)$ be the jth level wavelet coefficients for $x_1^{(L)}(t)$ and $x_2^{(L)}(t)$ respectively based on an wavelet filter $\{h(l)\}$ with transfer function $H(\lambda)$. Then,*

$$cov\left\{W_j^{(1)}(t), W_{j'}^{(2)}(t')\right\} = \int_{-1/2}^{1/2} H_j(\lambda)H_{j'}^*(\lambda)f_{1,2}(\lambda)e^{-i2\pi\lambda\left(2^j(t+1)-2^{j'}(t'+1)\right)}\mathrm{d}\lambda \tag{2.51}$$

where $f_{1,2}(\lambda)$ is the cross-spectral density of $x_1^{(L)}(t)$ and $x_2^{(L)}(t)$.

Proof. From Definition 2 on wavelet coefficients,

$$\text{cov}\left\{W_j^{(1)}(t), W_{j'}^{(2)}(t')\right\}$$

$$= \sum_{l=0}^{L_j-1}\sum_{l'=0}^{L_{j'}-1} h_j(l)h_{j'}(l')\text{cov}\left\{x_1^{(L)}\left(2^j(t+1)-1-l\right), x_2^{(L)}\left(2^j(t+1)-1-l\right)\right\}$$

$$= \sum_{l=0}^{L_j-1}\sum_{l'=0}^{L_{j'}-1} h_j(l)h_{j'}(l') \int_{-1/2}^{1/2} f_{1,2}(\lambda)e^{i2\pi\lambda(2^j(t+1)-2^{j'}(t'+1)+l'-l)}\mathrm{d}\lambda$$

$$= \int_{-1/2}^{1/2}\left(\sum_{l=0}^{L_j-1} h_j(l)e^{-i2\pi\lambda l}\right)\left(\sum_{l'=0}^{L'_j-1} h'_j(l')e^{-i2\pi\lambda l'}\right)^*$$

$$\times f_{1,2}(\lambda)e^{i2\pi\lambda(2^j(t+1)-2^{j'}(t'+1)+l'-l)}\mathrm{d}\lambda$$

$$= \int_{-1/2}^{1/2} H_j(\lambda)H_{j'}(\lambda)f_{1,2}(\lambda)e^{i2\pi\lambda(2^j(t+1)-2^{j'}(t'+1)+l'-l)} \tag{2.52}$$

$\square$

Corollary 1 (Spectral representation of wavelet covariance). *With the same conditions as Lemma 1,*

$$\text{cov}\left\{W_j^{(1)}(t), W_j^{(2)}(t)\right\} = \int_{-1/2}^{1/2} \mathcal{H}_j(\lambda)f_{1,2}(\lambda)\mathrm{d}\lambda, \tag{2.53}$$

where $\mathcal{H}_j(\lambda)$ denotes the squared gain function of $\{h_j(l)\}$.

Proof. From Lemma 1,

$$\text{cov}\left\{W_j^{(1)}(t), W_{j'}^{(2)}(t')\right\} = \int_{-1/2}^{1/2} H_j(\lambda)H_j^*(\lambda)f_{1,2}(\lambda)\mathrm{d}\lambda$$

$$= \int_{-1/2}^{1/2} |H_j(\lambda)|^2 f_{1,2}(\lambda)\mathrm{d}\lambda \tag{2.54}$$

$\square$

The wavelet covariance $\nu_{1,2}(j) \doteq \text{cov}[W_j^{(1)}(t), W_j^{(2)}(t)]$ can be estimated from wavelet coefficients. Suppose that $\mathbb{E}[W_j(t)] = 0$. Then, the following unbiased

25
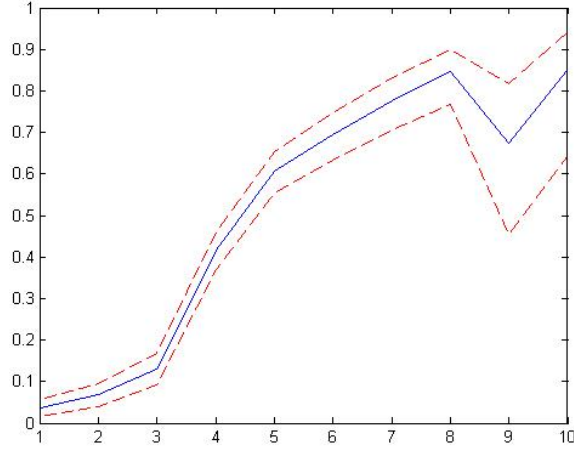
Figure 2.3: An example of wavelet correlations. The graph shows scale-dependent correlations between two time series. Dashed lines denote confidential intervals for the estimated wavelet correlations.

estimator of wavelet variance $\nu_{1,2}(j)$ is obtained:

$$\hat{\nu}_{1,2}(j) = \frac{1}{n_j 2^j} \sum_{k=1}^{n_j} W_j^{(1)}(k) W_j^{(2)}(k), \tag{2.55}$$

where n_j is the number of wavelet coefficients at the j-th scale. Likewise, the wavelet correlation $\rho_{1,2}(j) \doteq \text{cor}[W_j^{(1)}(t), W_j^{(2)}(t)]$ between $x_1(t)$ and $x_2(t)$ at the j-th scale can be estimated as follows

$$\rho_{1,2}(j) = \frac{\nu_{1,2}(j)}{[\nu_1(j)\nu_2(j)]^{1/2}}. \tag{2.56}$$

Unlike Pearson correlation, the wavelet correlation enables us to observe the distribution of cross-correlation over several octave frequency bands or scales as illustrated in Figure 2.3. Figure 2.4 illustrates an example of wavelet correlation matrices in a multivariate long memory process. A higher scale corresponds to a lower frequency band as discussed in Remark 1.
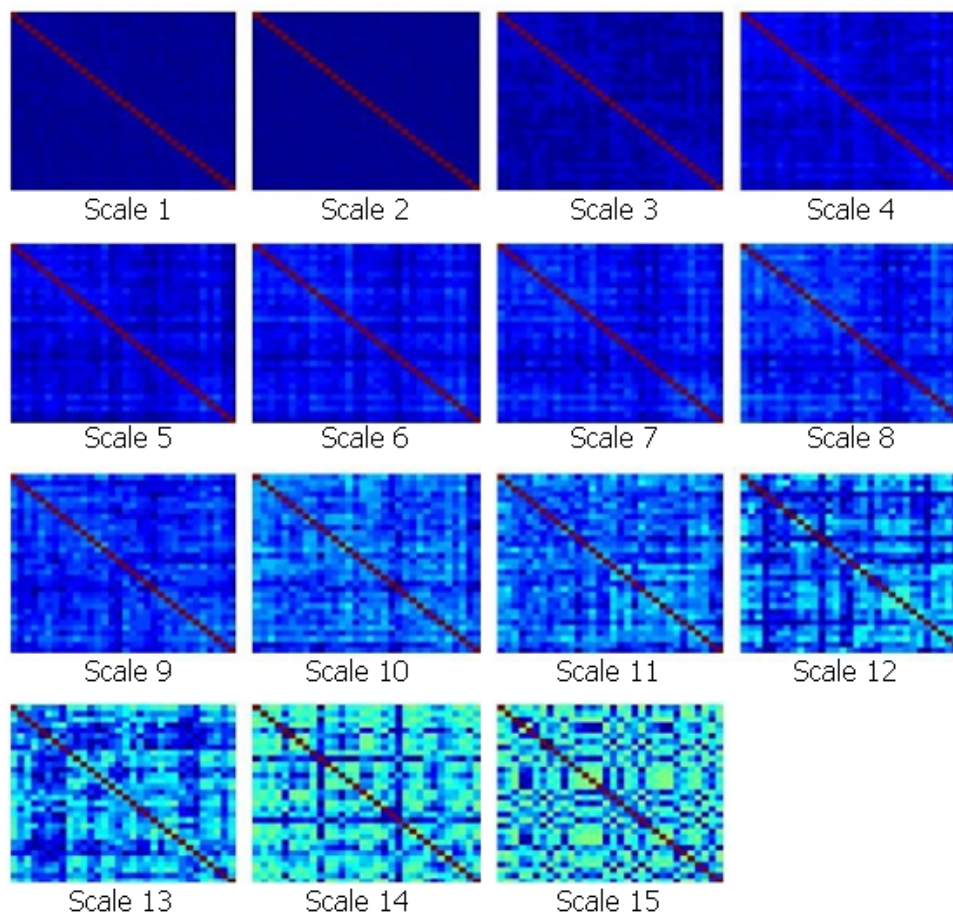
Figure 2.4: An example of wavelet correlation in a multivariate long memory process.

2.6 Stochastic processes

A time series can be regarded as a realization of a stochastic process $\{X_t\}$ - called a random variable. this section describes elementary theories on stochastic processes as a preliminary step to study the long memory processes discussed in Section 2.7.

2.6.1 Univariate random variables

Let X denote an random variable. If X is a discrete RV, the probability of the event X being x can be expressed as $\mathbf{P}[X = x]$. On the other hand, if X

is a continuous RV, the probability can be expressed as $\mathbf{P}\left[x < X < x + \Delta\right] = f_X\left(x\right)\Delta$ where $f_X\left(\cdot\right)$ is the *probability density function* (PDF) for X and Δ is an infinitesimal Percival & Walden (2006). The mean of X is defined as

$$E\left\{X\right\} = \int_{-\infty}^{\infty} x f_X\left(x\right) dx. \tag{2.57}$$

Likewise, the mean of a function $h\left(X\right)$ is

$$E\left\{X\right\} = \int_{-\infty}^{\infty} h\left(x\right) f_X\left(x\right) dx. \tag{2.58}$$

The variance of X is

$$var\left\{X\right\} \equiv E\left\{\left(X - E\left\{X\right\}\right)^2\right\} = \int_{-\infty}^{\infty} \left(x - E\left\{X\right\}\right)^2 f_X\left(x\right) dx \tag{2.59}$$

One of the typical PDF approximation is the Gaussian PDF where

$$f_X\left(x; \mu, \sigma\right) = \frac{1}{\sqrt{2\pi\sigma^2}} e^{-(x-\mu)^2/(2\sigma^2)} \tag{2.60}$$

where μ and σ are location and scale parameters which satisfy $-\infty < x, \mu < \infty$, $\sigma > 0$. It is the same expression as $X \overset{d}{=} \mathcal{N}\left(\mu, \sigma^2\right)$ which means that X has a Gaussian PDF with mean μ and variance σ^2.

2.6.2 Bivariate Random Variables

Let the joint PDF of random variables X_1 and X_2 be $f_{1,2}\left(x_1, x_2\right)$. The marginal PDFs $f_1\left(\cdot\right)$ and $f_2\left(\cdot\right)$ can be obtained from the join PDF as follows

$$f_1\left(x_1\right) = \int_{-\infty}^{\infty} f_{1,2}\left(x_1, x_2\right) \mathrm{d}x_2, \quad f_2\left(x_2\right) = \int_{-\infty}^{\infty} f_{1,2}\left(x_1, x_2\right) \mathrm{d}x_1. \tag{2.61}$$

Notice that X_1 and X_2 are independent if $f_{1,2}\left(x_1, x_2\right) = f_1\left(x_1\right) f_2\left(x_2\right)$ for all x_1 and x_2. The expected value or mean of a function $g\left(X_1, X_2\right)$ is

$$E\left\{g\left(X_1, X_2\right)\right\} = \int_{-\infty}^{\infty} \int_{-\infty}^{\infty} g\left(x_1, x_2\right) f_{1,2}\left(x_1, x_2\right) \mathrm{d}x_1 \mathrm{d}x_2. \tag{2.62}$$

The covariance of X_1 and X_2 is

$$
\begin{aligned}
\mathrm{cov}\left\{X_1, X_2\right\} &\equiv E\left\{\left(X_1 - \mu_1\right)\left(X_2 - \mu_2\right)\right\} \\
&= \int_{-\infty}^{\infty}\int_{-\infty}^{\infty}\left(x_1 - \mu_1\right)\left(x_2 - \mu_2\right)f_{1,2}\left(x_1, x_2\right)\mathrm{d}x_1\mathrm{d}x_2 \quad (2.63)
\end{aligned}
$$

where $E\left\{X_1\right\} = \mu_1$ and $E\left\{X_2\right\} = \mu_2$. The sum of two independent RVs X_1 and X_2 is identical to the convolution of their PDFs. In other words, if $Y_1 = X_1$ and $Y_2 = X_1 + X_2$,

$$
f_{Y_1}\left(y_1\right) = \int_{-\infty}^{\infty} f_{X_0}\left(y_0\right)f_{X_1}\left(y_1 - y_0\right)\mathrm{d}y_0. \quad (2.64)
$$

Let a multivariate random vector $\mathbf{X} = \left[X_1, X_2, \cdots, X_N\right]^T$ satisfy $\mathbf{Y} = \mathbf{M}\mathbf{X}$ where $\mathbf{M}$ is an $M \times N$ matrix. Then, the mean and covariance matrix of $\mathbf{Y}$ are given by

$$
\mu_{\mathbf{Y}} = \mathbf{M}\mu_{\mathbf{X}}, \quad (2.65)
$$

$$
\Sigma_{\mathbf{Y}} = \mathbf{M}\Sigma_{\mathbf{X}}\mathbf{M}^T \quad (2.66)
$$

If $\mathbf{M}$ is an orthonormal transform, the total variance is preserved as follows

$$
\sum_{t=0}^{N-1}\mathbb{E}\left\{Y_t^2\right\} = \sum_{t=0}^{N-1}\mathbb{E}\left\{X_t^2\right\}. \quad (2.67)
$$

2.6.3 Stationary Stochastic Processes

Stationarity The stochastic process $X(t)$ is said to be (second order) stationary if

1. $\mathbb{E}\left[X(t)\right] = \mu_X$ for $\forall t \in \mathbb{Z}$ and
2. $\mathrm{cov}\left[X(t), X(t+\tau)\right] = s_\tau$ for all integers $\forall t, \tau \in \mathbb{Z}$.

In this case, the variance of $X(t)$ is constant over t. The sequence s_τ is called the *autocovariance sequence* (ACVS). The ACVS can be described as a *spectral density function* $f(\cdot)$ (SDF) known as the power spectrum. Suppose that

$$
\sum_{\tau=-\infty}^{\infty} s_\tau^2 < \infty. \quad (2.68)
$$

Then, the *spectral density function* (SDF) of $X(t)$ can be defined as the Fourier transform of s_τ as follows

$$f(\lambda) = \Delta t \sum_{\tau=-\infty}^{\infty} s_\tau e^{-i2\pi\lambda\tau\Delta t} \quad, |\lambda| \leq \lambda_{\mathbb{N}}, \tag{2.69}$$

$$\int_{-\lambda_{\mathbb{N}}}^{\lambda_{\mathbb{N}}} f(\lambda) e^{-i2\pi\lambda\tau\Delta t} \mathrm{d}\lambda = s_\tau, \tag{2.70}$$

where $\lambda_{\mathbb{N}} = 1/(2\Delta t)$ is called the *Nyquist frequency*. Notice that both SDF and ACVS are even functions, i.e., $f(-\lambda) = f(\lambda)$ and $s_{-\tau} = s_\tau$. If $\tau = 0$,

$$\int_{-\lambda_{\mathbb{N}}}^{\lambda_{\mathbb{N}}} f(\lambda) \mathrm{d}\lambda = s_0 = \mathrm{var}\{X(t)\}. \tag{2.71}$$

It implies that $f(\cdot)$ decomposes the variance with respect to frequency. The requirements for stationarity are that $f(\lambda) \geq 0$ for all λ, that $f(\lambda) = f(-\lambda)$, and that $0 \leq \int_{-\lambda_{\mathbb{N}}}^{\lambda_{\mathbb{N}}} f(\lambda)\mathrm{d}\lambda < \infty$.

Linear filtering   Consider a linear filter $b(t)$ of width M. The *transfer function* of $b(t)$ is defined by

$$B(\lambda) \doteq \sum_{t=0}^{M-1} b(t) e^{-i2\pi\lambda t}. \tag{2.72}$$

Let $y(t)$ be a stochastic process such filtered linearly by $b(t)$ such that

$$y(t) \doteq \sum_{t=0}^{M-1} b(l) X(t-l). \tag{2.73}$$

Then its SDF is given by

$$f_Y(\lambda) = \mathcal{B}(\lambda) f(\lambda), \tag{2.74}$$

where $\mathcal{B}(\lambda) \equiv |B(\lambda)|^2$ defines the *squared gain function*. Since the integral of the SDF is always equal to the process variance,

$$\mathrm{var}[y(t)] = \int_{-1/2}^{1/2} f_Y(\lambda)\mathrm{d}\lambda = \int_{-1/2}^{1/2} \mathcal{B}(\lambda) f(\lambda)\mathrm{d}\lambda. \tag{2.75}$$

If the integral has a finite value, the filtered series $y(t)$ is also a stationary process.

Autoregressive process   A stochastic process $x(t)$ is said to be *autoregressive* (AR) of order p if it satisfies

$$\sum_{n=0}^{p} a_n x(t-n) = \varepsilon(t) \tag{2.76}$$

where $\varepsilon(t$ is a white Gaussian noise process with mean zero and variance σ_ε^2. It can be re-expressed as

$$\alpha(\mathcal{B}) x(t) = \varepsilon(t) \tag{2.77}$$

where $\mathcal{B}$ is the back-shift operator and $\alpha(\mathcal{B}) \doteq 1 + a_1\mathcal{B} + \cdots + a_p\mathcal{B}^p$. Let $\alpha(\mathcal{B}) = \prod_{n=1}^{p}(1 - \mu_n\mathcal{B})$. If $|\mu_n| < 1$, $x(t)$ is asymptotically stationary (Priestley, 1989) whose SDF is given by

$$f(\lambda) = \frac{\sigma_\varepsilon^2}{\left|1 - \sum_{n=1}^{p} a_n e^{-i2\pi\lambda n}\right|^2} \quad , |\lambda| \le 1/2. \tag{2.78}$$

2.7   Long memory statistics

The long memory phenomenon is the structure of slowly decaying self-similarity. It has been ubiquitously found in a variety of fields including stock market, hydrology, transportation network, and neuroimaging (Ledesma & Liu, 2000; Maxim et al., 2005; Molz et al., 1997; Willinger et al., 1999). A lot of mathematical methodologies regarding long memory have been developed since Mandelbrot suggested the concept of fractal (Cootner et al., 1997; Cox, 1984; Mandelbrot, 1977, 1983). In this section, a basic theory of long memory processes is summarized especially focusing on such long memory models as fractional Brownian motion (FBM) and fractionally integrated (FI) process. These models will be exploited as a background theory to investigate the long memory dynamics of hemodynamic response in Chapter 3. For detailed studies, refer to Beran (1992, 1994); Doukhan et al. (2010, 2002); Embrechts (2001); Lowen & Teich (2005); Rangarajan & Ding (2003); Robinson (2003).

2.7.1 Basic concepts

The definition of a stationary process with long memory is described according to (Beran, 1994).

Definition 4 (Stationary long memory process). Suppose that $x(t)$ is a stationary process with an SDF $f(\lambda)$. Then, $x(t)$ is said to be a stationary long memory process if there exist a real number β and a constant c_f satisfying $\beta \in (0,1)$ and $c_f > 0$ such that

$$\lim_{\lambda \to 0} \frac{f(\lambda)}{c_f \, |\lambda|^{-\beta}} = 1. \tag{2.79}$$

In other words, a stationary long memory process has the SDF $f(\lambda)$ such that $f(\lambda) \approx c_f \, |\lambda|^{-\beta}$ as $\lambda \to 0$. The above definition is equivalent to the description such that there exist $\alpha \in (0,1)$ and $c_s > 0$ which satisfy

$$\lim_{\tau \to \infty} \frac{s_\tau}{c_s \tau^{-\alpha}} = 1 \tag{2.80}$$

where s_τ is the ACVS of $x(t)$. The equation (2.80) implies that a stationary long memory process has slowly decaying autocorrelation.

Lots of robust methods have been proposed to estimate the fractal dimension or memory parameter in a long memory process. These include the Whittle estimator (Beran, 1994), periodogram (Robinson, 1995), Higuchi's method (Higuchi, 1988), R/S method (Mandelbrot & Taqqu, 1979; Taqqu et al., 1995), detrended fluctuation analysis (Peng et al., 1994, 1995), wavelet ML estimator Fadili & Bullmore (2002), and so on.

2.7.2 Long memory models

In this section, two long memory models which have been widely used in neuroimaging studies, are introduced: fractional Brownian motion (FBM) and fractionally integrated (FI) process. For example, the fractional Gaussian noise (FGN), as the increment process of FBM, has been usually exploited as a long memory model of resting state functional MRI time series which are positively autocorrelated and whose spectral densities follow power-law scaling (Maxim et al., 2005). The FI process has not been well introduced in the field of neuroscience,

but it was adopted as a primary model to describe fractal connectivity (Achard et al., 2008).

2.7.2.1   Fractional Brownian motion

Definition 5 (Vector fractional Brownian motion)**.** Let $\mathbf{B}_H(t)$ be a n-dimensional vector Gaussian process that is continuous for all t and satisfies for $c > 0$

$$\mathbf{B}_H(ct) = c^{\mathbf{H}}\mathbf{B}_H(t) \tag{2.81}$$

where $\mathbf{H}$ is a matrix with $H_{i,j} \in (0,1)$, $\forall i,j$ and

$$c^{\mathbf{H}} = \sum_{k=0}^{\infty} (\log c)^k \frac{\mathbf{H}^k}{k!}, \tag{2.82}$$

and its increments are stationary. Then, $\mathbf{B}_H(t)$ is said to be *operator self-similar* (o.s.s.) and is called the *vector fractional Brownian motion* (VFBM) with exponent $\mathbf{H}$.

Lemma 2 (Stochastic integral representation of VFBM)**.** *Let $\mathbf{B}_H(t)$ be a VFBM with exponent $\mathbf{H}$ whose eigenvalues h_k satisfies $0 < \Re(h_k) < 1$ and $\Re(h_k) \neq 1/2$ for $k = 1, \cdots, n$. Then, there exist the square matrices $\mathbf{A}_+$ and $\mathbf{A}_-$ such that*

$$\begin{aligned}
\mathbf{x}(t) \; = \; \int_{\mathbb{R}} \Big(& \Big((t-\tau)_+^{\mathbf{H}-1/2} - (-\tau)_+^{\mathbf{H}-1/2} \Big) \mathbf{A}_+ \\
& + \Big((t-\tau)_-^{\mathbf{H}-1/2} - (-\tau)_-^{\mathbf{H}-1/2} \Big) \mathbf{A}_- \Big) \, \mathrm{d}\mathbf{B}(\tau)
\end{aligned} \tag{2.83}$$

where $\mathbf{B}(t)$ is a vector process of independent Brownian motions.

For the proof of Lemma 2, refer to Theorem 3.2 in Didier & Pipiras (2011). According to Lemma 2, a vector self-similar process can be represented by stochastic integral. Especially, (2.83) implies that the vector fractional Brownian motion can be regarded as a causal linear transform of a Brownian motion (or a Wiener process) with a self-similarity kernel characterized by Hurst exponents (Coeurjolly et al., 2010). It is difficult to find out the solution of $\mathbf{A}_+$ and $\mathbf{A}_-$. Instead, two specific cases have been mainly focused: the causal case ($\mathbf{A}_- = 0$) and the

well-balanced case ($\mathbf{A}_+ = \mathbf{A}_-$). The causal case corresponds to the multivariate extension of integral representation suggested in Mandelbrot & Van Ness (1968) while the well-balanced case corresponds to the multifractional Brownian motion introduced by Stoev & Taqqu (2006).

Lemma 3. *Let* $\mathbf{A}_+\mathbf{A}_+^t = (A_{i,j}^{++})$, $\mathbf{A}_-\mathbf{A}_-^t = (A_{i,j}^{--})$, $\mathbf{A}_+\mathbf{A}_-^t = (A_{i,j}^{+-})$, *and* $\mathbf{A}_-\mathbf{A}_+^t = (A_{i,j}^{-+})$ *where* $\mathbf{A}_+ = (A_{i,j}^+)$ *and* $\mathbf{A}_- = (A_{i,j}^-)$ *are given in Lemma 2.*

(i) *The auto-covariance of* $X_i(t)$ *is*

$$\mathrm{E}\left[X_i(s), X_i(t)\right] = c_{i,i}\left|s\right|^{2H_i} + c_{i,i}\left|t\right|^{2H_i} - c_{i,i}\left|t-s\right|^{2H_i} \tag{2.84}$$

where

$$c_{i,i} = \frac{B(H_i + 1/2, H_i + 1/2)}{2\sin(\pi H_i)}\left(A_{i,i}^{++} + A_{i,i}^{--} - 2\sin(\pi H_i)A_{i,i}^{+-}\right). \tag{2.85}$$

(ii) *If* $i \neq j$ *and* $H_i + H_j \neq 1$, *the cross-covariance of* $X_i(s)$ *and* $X_j(t)$ *is*

$$\mathrm{E}\left[X_i(s), X_j(t)\right] = c_{i,j}s\left|s\right|^{H_i + H_j - 1} + c_{j,i}t\left|t\right|^{H_i + H_j - 1}$$
$$- c_{j,i}(t - s)\left|t - s\right|^{H_i + H_j - 1} \tag{2.86}$$

where

$$c_{i,j} = \frac{B(H_i + 1/2, H_j + 1/2)}{\sin(\pi(H_i + H_j))} \times \left(A_{i,j}^{++}\cos(\pi H_i)\right.$$
$$\left. + A_{i,j}^{--}\cos(\pi H_j) - A_{i,j}^{+-}\sin\left(\pi(H_i + H_j)\right)\right) \tag{2.87}$$

(iii) *If* $i \neq j$ *and* $H_i + H_j = 1$, *the cross-covariance of* $X_i(s)$ *and* $X_j(t)$ *is*

$$\mathrm{E}\left[X_i(s), X_j(t)\right] = d_{i,j}\left(\left|s\right| + \left|t\right| - \left|s - t\right|\right)$$
$$+ f_{i,j}\left(t\log\left|t\right| - s\log\left|s\right| - (t - s)\log\left|t - s\right|\right) \tag{2.88}$$

where

$$d_{i,j} \doteq \frac{B(H_i + 1/2, H_j + 1/2)}{2}$$
$$\times \left(\frac{\sin(\pi H_i) + \sin(\pi H_j)}{2} (A_{i,j}^{++} + A_{i,j}^{--}) - A_{i,j}^{+-} - A_{i,j}^{-+} \right), \quad (2.89)$$

$$f_{i,j} \doteq \frac{H_j - H_i}{2} \left(A_{i,j}^{++} - A_{i,j}^{--} \right) \quad (2.90)$$

The proof of Lemma 3 is provided by Proposition 3.1 in (Lavancier et al., 2009). The properties of vFBM can be exploited to figure out the theoretical relationship of Hurst exponents with functional connectivity of the brain (see Section 3.5).

Let $\Delta\mathbf{B}_H(t) \doteq \mathbf{B}_H(t+1) - \mathbf{B}_H(t)$ be the increments of vector fractional Brownian motion. In the well-balanced case ($\mathbf{A}_+ = \mathbf{A}_-$), the cross-covariance of $\Delta\mathbf{B}_H(t)$ becomes proportional to that of a *fractional Gaussian noise* from Lemma 3 as follows

$$\mathrm{E}\left[\Delta\mathbf{B}_H(t)\Delta\mathbf{B}_H(t+\tau)\right] = \frac{\sigma_{i,j}^2}{2} \left(|\tau - 1|^{H_i+H_j} - 2|\tau|^{H_i+H_j} + |\tau + 1|^{H_i+H_j} \right).$$
$$(2.91)$$

Therefore, the fractional Gaussian noise is considered as a special case of the increments of fractional Brownian motion.

2.7.2.2 Fractionally integrated process

The fractionally integrated (FI) process is a flexible long memory model which encompass several classes of long memory such as fractionally integrated noise (FIN) and ARFIMA(p, d, q) process Granger (1980); Hosking (1981); Moulines et al. (2007). In this section, both univariate and multivariate FI process models are introduced.

Univariate model A univariate FI process can be defined according to Shimotsu (2007) as follows.

Definition 6 (FI process)**.** Let $x(t)$ be a weakly stationary discrete process of

length N given by

$$u(t) = (1 - \mathcal{B})^d x(t) \tag{2.92}$$

where $d \in (-1/2, 1/2)$, $\mathcal{B}$ denotes the back-shift operator, and $u(t)$ (called *short memory*) is a stationary process whose spectral density $f_u(\lambda)$ is a non-negative symmetric function bounded on $(-1/2, 1/2)$ and bounded away from zero at $\lambda = 0$. Then, $x(t)$ is called a *fractionally integrated process* with memory parameter d or an *FI process*.

Lemma 4 (Convolution representation of an FI process)**.** *Let $x(t)$ be an FI process with memory parameter d. Then, $x(t)$ can be represented as the convolution of $u(t)$ with a long memory (LM) filter $g_L(t)$ as follows*

$$x(t) = \sum_{\tau=0}^{\infty} g_L(\tau) u(t - \tau) \tag{2.93}$$

where

$$g_L(t) := \frac{d\Gamma(d + t)}{\Gamma(d + 1)\Gamma(t + 1)}. \tag{2.94}$$

Lemma 5 (Spectral density of an FI process)**.** *If $-1/2 < d < 1/2$, the spectral density of $x(t)$ is given by*

$$S(\lambda) = \left|1 - e^{-i\lambda}\right|^{-2d} S_u(\lambda). \tag{2.95}$$

The fractal behavior is controlled by the memory parameter d. If $0 < d < 1/2$, the process $x(t)$ is said to be a stationary long memory process with memory parameter d while $x(t)$ is nonstationary if $d > 0.5$ (Moulines et al., 2007). If $d = 0$, the process becomes a white noise.

Multivariate model   Definition 6 of the univariate long memory model can be extended to the multivariate case.

Definition 7 (Multivariate FI process)**.** Consider a weakly stationary q-vector

process $\mathbf{x}(t)$ given by

$$
\begin{pmatrix} (1-\mathcal{B})^{d_1} & & 0 \\ & \ddots & \\ 0 & & (1-\mathcal{B})^{d_q} \end{pmatrix} \begin{pmatrix} x_1(t) \\ \vdots \\ x_q(t) \end{pmatrix} = \begin{pmatrix} u_1(t) \\ \vdots \\ u_q(t) \end{pmatrix}, \tag{2.96}
$$

where $d_k \in (-1/2, 1/2)$ f or $\forall k = 1, \cdots, q$, $\mathbf{u}(t) = (u_1(t), ..., u_q(t))$ is a multivariate stationary process whose spectral density $\mathbf{S}(f) = [S_{m,n}(f)]$ is bounded on $(-1/2, 1/2)$ and bounded away from zero at $\lambda = 0$. Then, $\mathbf{x}(t)$ is called a *multivariate fractionally integrated process* with memory parameter $\mathbf{d}$.

Lemma 6 (Spectral density of a multivariate FI process). *Let $\mathbf{x}(t)$ be a multivariate FI process with memory parameter $\mathbf{d}$. Then, the spectral density of $\mathbf{x}(t)$ is given by*

$$
\mathbf{S}(f) = \Phi(f) \mathbf{S}_u(f) \Phi^*(f) \tag{2.97}
$$

where

$$
\Phi(f) = \begin{pmatrix} (1-e^{if})^{-d_1} & & 0 \\ & \ddots & \\ 0 & & (1-e^{if})^{-d_q} \end{pmatrix}. \tag{2.98}
$$

In the case of $0 < d_k < 1/2$ for $1 \leq k \leq q$, $\mathbf{X}(t)$ is said to be a stationary long memory process with memory parameter $\mathbf{d} = (d_1, \cdots, d_q)$. If $\mathbf{u}(t)$ is a white noise, i.e., $\mathbf{u}(t) \overset{\text{i.i.d.}}{\sim} N(0, \Sigma_u)$, $\mathbf{X}(t)$ is called a *multivariate fractionally integrated noise* (mFIN). In this case, the cross-spectral density of $x_m(t)$ and $x_n(t)$ is given by

$$
f_{m,n}(\lambda) = \gamma_{m,n} \left(1 - e^{i\lambda}\right)^{-d_m} \left(1 - e^{-i\lambda}\right)^{-d_n} \tag{2.99}
$$

where $\gamma_{m,n}$ is identical to the (m, n)-th element of Σ_u. If $\mathbf{u}(t)$ is a vector ARMA process, $\mathbf{x}(t)$ becomes a multivariate ARFIMA process whose property is shown in Corollary 2.

Corollary 2 (Spectral density of a vector ARFIMA process). *Let $\epsilon_i(t)$ denote an independent identically distributed normal variable with $E[\epsilon_i(t)] = 0$ and $E[(\epsilon_i(t))^2] = E[(\epsilon_i(1))^2]$. Let $\mathbf{u}(t)$ be an ARMA process defined by $u_i(t) := \Phi_i(\mathcal{B})^{-1}\Psi_i(\mathcal{B})\epsilon_i(t)$ where $\Phi_i(\mathcal{B}) = -\sum_{j=0}^{r} \phi_i(j)\mathcal{B}^j$, $\phi_i(0) = -1$ and $\Psi_i(\mathcal{B}) =$*

$\sum_{j=0}^{q} \psi_i(j)\mathcal{B}^j$, $\psi_i(0) = 1$. *Then, the spectral density of* $\mathbf{u}(t)$ *is given by*

$$\mathbf{f}^{(u)}(\lambda) = \frac{1}{2\pi}\mathbf{\Phi}^{-1}(e^{i\lambda})\mathbf{\Psi}(e^{i\lambda})\mathbf{\Sigma}_\epsilon\mathbf{\Psi}(e^{-i\lambda})\mathbf{\Phi}^{-1}(e^{-i\lambda}) \qquad (2.100)$$

where $\mathbf{\Phi}(e^{i\lambda}) := \mathrm{diag}\left(\Phi_1(e^{i\lambda}), \cdots, \Phi_p(e^{i\lambda})\right)$, $\mathbf{\Psi}(e^{i\lambda}) := \mathrm{diag}\left(\Psi_1(e^{i\lambda}), \cdots, \Psi_p(e^{i\lambda})\right)$, *and* $\mathbf{\Sigma}_\epsilon := \left[\sigma^2_{\epsilon,(m,n)}\right]_{m,n}$ *with* $\sigma^2_{\epsilon,(m,n)} = E\left[\epsilon_m(t)\epsilon_n(t)\right]$. *Hence,*

$$f^{(u)}_{m,n}(\lambda) = \frac{\sigma^2_{\epsilon,(m,n)}}{2\pi}\frac{\psi_1(e^{i\lambda})\psi_2^*(e^{i\lambda})}{\phi_m(e^{i\lambda})\phi_n^*(e^{i\lambda})}. \qquad (2.101)$$

In this case, the multivariate process $\mathbf{x}(t)$ is called a *vector autoregressive fractionally integrated moving average (VARFIMA) process*.

Chapter 3

Long memory model of BOLD signals

3.1 Introduction

A time series with long memory has slowly decaying autocorrelation (see Section 2.7.1). Furthermore, the long-range dependence may be also found from cross-correlation between two time series. In that the functional connectivity among brain regions has been ordinarily defined as the cross-correlation coefficient of two time series, we are compelled to wonder the affinity of long memory to functional connectivity in a multivariate time series. Does the slowly-decaying cross-correlation of two BOLD signals taken at rest imply that the brain regions are functionally connected? Does the difference of memory parameter between two BOLD signals influence the functional connectivity? While the long memory phenomenon has been investigated independent of functional connectivity, it is significantly important to answer these questions since it would enable the theoretical interpretation of long memory in terms of functional connectivity.

The solution to these problems can be found by modeling the resting state BOLD signal with long memory. A few statistical models, such as autoregressive (AR) process and fractional Gaussian noise (FGN), have been widely used to describe long memory in BOLD signals (Bullmore et al., 1996, 2004, 2001; Dale, 1999; Locascio et al., 1997; Maxim et al., 2005; Purdon & Weisskoff, 1998; Worsley

et al., 2002; see Section 2.7.2 for the related theories). Since the theoretical relation of long memory to functional connectivity hinges on the statistical model of long memory (see Section 3.5.1), the choice of a long memory model for resting state BOLD signals is a prerequisite. However, the classical hypotheses of long memory based on either AR or FGN models have not been validated as the most felicitous model. In what manner can the best long memory model of resting state BOLD signals be determined? The criteria for the best long memory model may be established of the physical mechanism of long memory in BOLD signals.

The long memory phenomenon in resting state BOLD signals ensues from a diversity of physical and biological factors such as heart beat (Cordes et al., 2001; Schmitt & Ivanov, 2007), respiration (Birn et al., 2006; Cordes et al., 2001), cerebral hemodynamics, neuronal activity (Allegrini et al., 2009; Mazzoni et al., 2007), and instrumental noise. The variety of long memory sources makes it formidable for us to figure out the synthetic effect of intricate physical or biological processes on long memory.

Nevertheless, it is rational to assume that the cerebral hemodynamics has the most tremendous effect on long memory of resting state BOLD signals among all sources. This assumption is grounded in the previous reports which demonstrate not only that vasomotion and blood flow are the major sources of BOLD fluctuation (Buxton, 2002), but also that the cerebral hemodynamics exhibits fractal behavior at rest. The fractal behavior of cerebral blood volume (CBV) fluctuation at rest was found in low frequencies through both near-infrared spectroscopy and laser Doppler flowmetry (Herman et al., 2009), and the fractal properties of cerebral blood flow (CBF) was found through transcranial Doppler ultrasonography (Latka et al., 2005; West et al., 2003; Zhang et al., 2000) (see Figure 3.1). These observations jointly provide indirect evidence that the long memory phenomenon of resting state BOLD signals is most influenced by cerebral hemodynamics. Herman et al. (2009), hence, assumed that the fractal behavior found in BOLD signals has the common origin with that of CBV. This hypothesis indicates that the physical mechanism of long memory in BOLD signals can be effectively described through modeling cerebral hemodynamics.

The cerebral hemodynamics has been modeled by either the Balloon-Windkessel model or the hemodynamic response function (HRF) that describe the relation
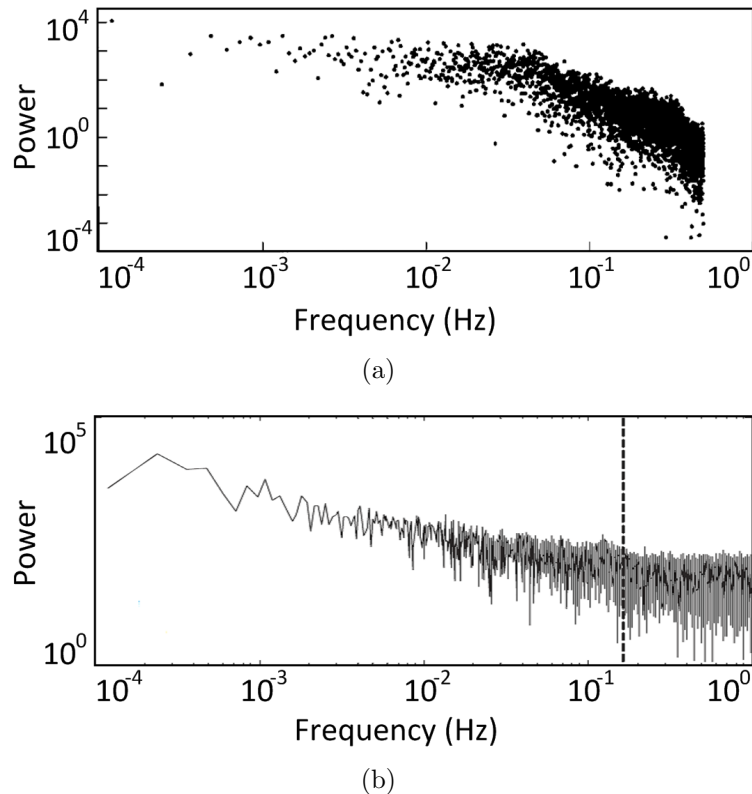
Figure 3.1: Power sepectrum of cerebral hemodynamic activities: (a) mean CBF velocity and (b) CBV fluctuation. The scale-invariant pattern is found from low frequencies of the power spectrum for both activities. Reproduced from Zhang et al. (2000) and Herman et al. (2009) with permission.

of BOLD signals to neuronal activities via hemodynamics (see Section 2.1). The equation (2.3), for instance, shows that a BOLD signal can be approximated as the linear convolution of neuronal activity with HRF. Although these models fit best into task-based BOLD signals which significantly correlate with neuronal activities responding to external stimuli, they also have been applied to analyze BOLD signals taken at rest as well. As an example, the typical HRF has been used to estimate the correlation between spontaneous neuronal activities and resting state BOLD signals by convolving either an LFP or EEG signal with HRF (Nir et al., 2007; Ramot et al., 2011; Rosa et al., 2010; see Figure 3.2), as well as to analyze self-organized criticality (Tagliazucchi et al., 2012).

However, it is questionable whether the typical models of hemodynamics suc-

Figure 3.2: An example of HRF applications for resting state fMRI. The BOLD signal responded to spontaneous eye movements (SEM) was predicted through convolving an EOG signal with HRF. Reproduced from Ramot et al. (2011) with permission.

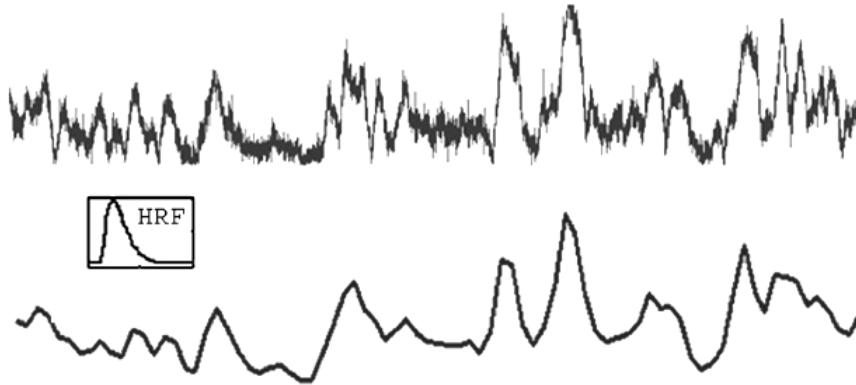cessfully describe the long-range dependence frequently found in resting state BOLD signals. To verify whether these models underlies the assumption that the long memory phenomenon in resting state BOLD signals can be caused by hemodynamic activities, a simulation study based on these models was performed (see Figure 3.3(a)). A BOLD signal was produced by convolving a Gaussian white noise process with HRF, however it did not exhibit the scale-invariance in low frequencies (see Figure 3.3(b)). The other BOLD signal along with its corresponding CBF and CBV activities were generated based on the Balloon model whose input is a Gaussian white noise process. Similar with the HRF-based simulation studies, no evidence for long memory phenomenon was found even at these signals simulated more elaborately based on the physical mechanism of hemodynamic activities (see Figure 3.3(c),(d),(e)). Such simulation results indicate that both HRF and the Balloon model may not be appropriate to describe the long memory effect caused by hemodynamic activities.

Along with these simulation studies, empirical observations have demonstrated that the typical HRF model does not describe an $1/f$ noise found in task-based BOLD signals. For example, it has been reported that the typical general linear model (GLM) of BOLD signals based on HRF is restricted to explain the $1/f$ noise (Fadili & Bullmore, 2002). To overcome this limitation of GLM, the noise component $\varepsilon \sim \mathcal{N}(0, \boldsymbol{\Sigma})$ in (2.1) was replaced by the $1/f$ noise $\varepsilon \sim \mathcal{N}(0, \boldsymbol{\Sigma}(\mathbf{H}))$ whose
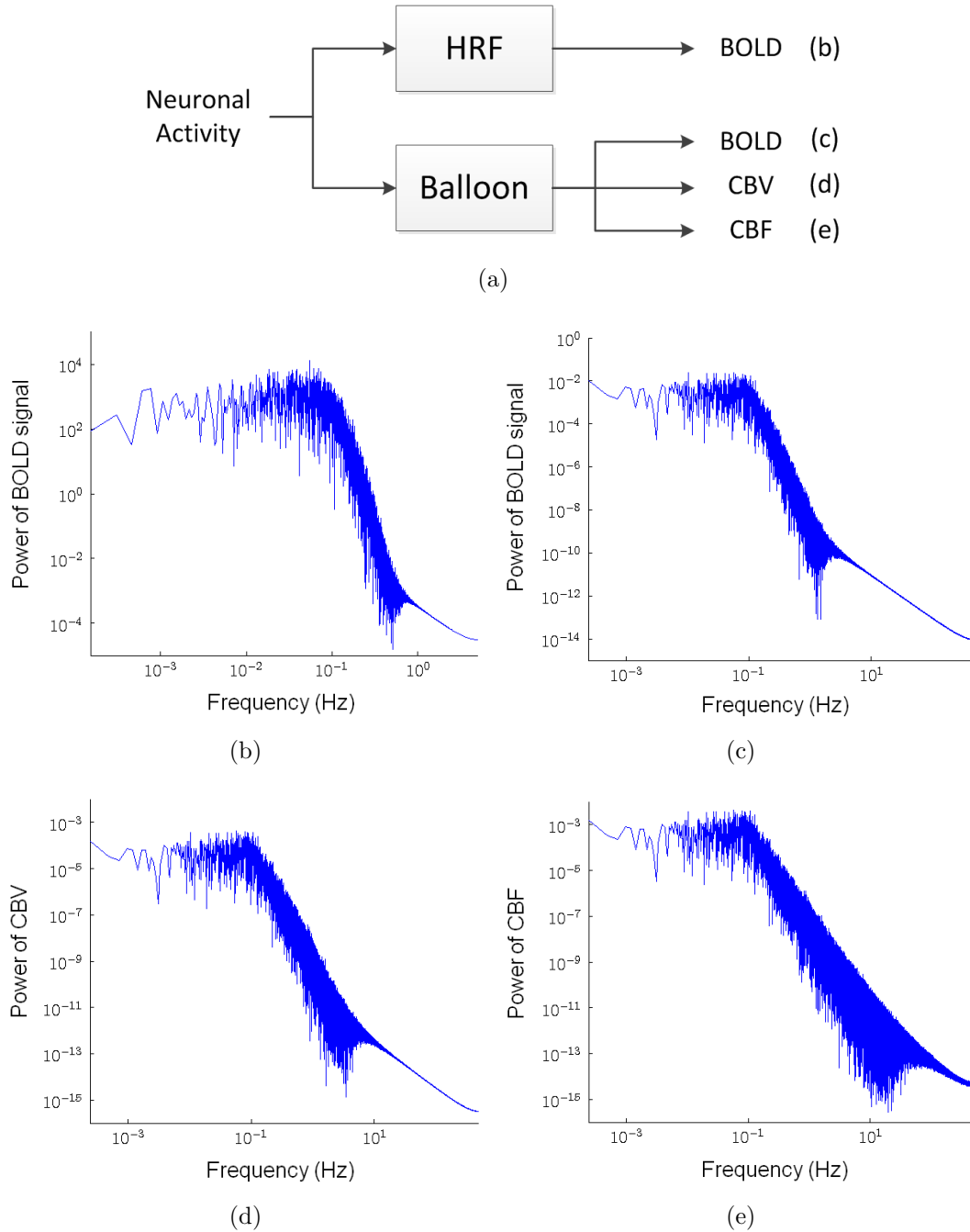
Figure 3.3: Power spectrums of BOLD signals simulated based on both HRF and the Balloon model. (a) The diagram of simulation procedures, (b) the periodograms of BOLD signal based on HRF, and (c-e) those of BOLD signal, CBV and CBF activities based on the Balloon model. These power spectrums do not exhibit fractal properties in low frequencies.
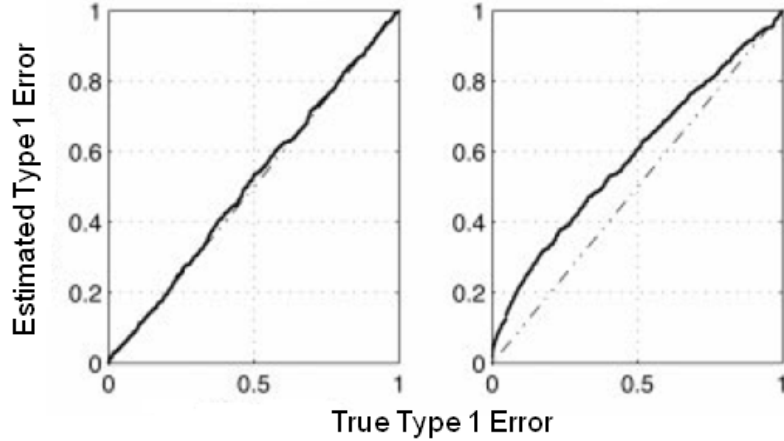
Figure 3.4: The performance of regression based on an $1/f$ noise model. BOLD signals were simulated with a variety of type I errors, and the performance of fractal-based regression methods such as WLS (Wavelet Least Squares) and OLS (Ordinary Least Squares) was evaluated by comparing true type I error with observed type I error. The WLS method has much better performance than the OLS method. Reproduced from Fadili & Bullmore (2002) with permission.

covariance is characterized by Hurst exponents $\mathbf{H}$; indeed, the regression performance of task-related BOLD responses was improved by applying the $1/f$ noise model such as fractional Gaussian noise (FGN) (see Figure 3.4). The $1/f$ noise model provides the statistical explanation on long-range dependence in BOLD signals, however it does not provide the explanation on how the phenomenon is caused especially by hemodynamic activities. Since the $1/f$ noise ε in the GLM framework is assumed to be generated regardless of hemodynamics characterized by the design matrix $\mathbf{X}$ in (2.1), the $1/f$ noise component is not attributed to the cerebral hemodynamics.

In synthetic consideration of these results, it can be concluded that the association between hemodynamic activity and long memory in resting state BOLD signals is not well clarified by either HRF or the Balloon model. These models do not predict the likelihood of long memory phenomenon induced by hemodynamic activities. The weakness of these hemodynamic models may not be serious in task-based BOLD signals since the long memory effect can be regressed out as an $1/f$ noise and the deterministic trend of BOLD responses correlated with stimulation is mainly considered. On the other hand, the long memory effect becomes

conspicuous in the resting state BOLD analyses since it is prominently observed in low frequencies of resting state BOLD signals while the temporal pattern of neuronal activities are unknown. Moreover, the strength of correlation between neuronal activity and BOLD response is likely to be affected by hemodynamic activities that intermediate between both of them and finally trigger the fractal pattern in BOLD signals. In other words, the functional connectivity in BOLD signals may not well reflect the original correlation of neuronal activities due to the corruption by hemodynamic fractal behavior. In these reasons, it is important to develop a novel model of hemodynamics that explains the long memory phenomenon in resting state BOLD signals.

Motivated by the restriction of the conventional hemodynamic model, the long memory model of hemodynamic response is proposed to describe the long memory phenomenon in resting state BOLD signals. Based on this novel hemodynamic model, it is shown that a stationary resting state BOLD signal with long memory can be better modeled as the fractionally integrated (FI) process than either FGN or AR processes. Furthermore, the effect of hemodynamic fractal behavior on resting state functional connectivity is derived theoretically and verified through simulation studies.

3.2 Linear long memory model of hemodynamic response

In this section, a novel linear model of hemodynamic response function (HRF) is proposed to describe long memory driven by hemodynamic activities in resting state BOLD signals. The long memory condition of hemodynamic response can be found from the generic HRF comprising lots of basis functions while the typical HRF consists of two basis functions. The long memory model of HRF implies that a resting state BOLD signal with long memory can be statistically modeled as a fractionally integrated process.

3.2.1 Generic hemodynamic response function

The conventional hemodynamic response function consists of two Gamma functions as introduced in (2.3). Let $u(t)$ be a neuronal activity and $x(t)$ be the hemodynamic response to $u(t)$. In this case, the hemodynamic response $x(t)$ has been modeled as the convolution of $u(t)$ with HRF which is a weighted combination of two Gamma functions (see Section 2.1). The HRF can be extended to comprise more than two arbitrary basis functions; in other words, a BOLD signal $x(t)$ is described as the linear convolution of neuronal activity $u(t)$ with HRF $g(t)$ by

$$x(t) = g(t) * u(t) \doteq \sum_{\tau=0}^{\infty} g(\tau)u(t - \tau) \tag{3.1}$$

where $u(t)$ denotes a neuronal activity, and $g(t)$ is represented as a linear sum of M basis functions as follows

$$g(t) \doteq \sum_{j=1}^{M} \kappa_j v_j(t). \tag{3.2}$$

The HRF $g(t)$ is called the *generic hemodynamic response function* with M basis functions (see Figure 3.5(b)). If $M = 2$ and $v_j(t)$ is a Gamma function, it becomes identical to the classical HRF model in (2.3) (see Figure 3.5(a)). This generic HRF had been first suggested by Henson & Friston (2006) to describe the variability of HRF shape either over brain regions or over individuals.

3.2.2 Long memory condition of HRF

The hemodynamic condition generating long memory in BOLD signals can be found on the basis of the generic hemodynamic response function in (3.2). Let us define the basis function $v_j(t)$ as the Poisson function as follows

$$v_j(t) = \frac{a_j^t e^{-a_j}}{\Gamma(t + 1)}. \tag{3.3}$$

Although the Gamma function has been widely used as the basis function, applying the Poisson function as a basis function may not be problematic since the
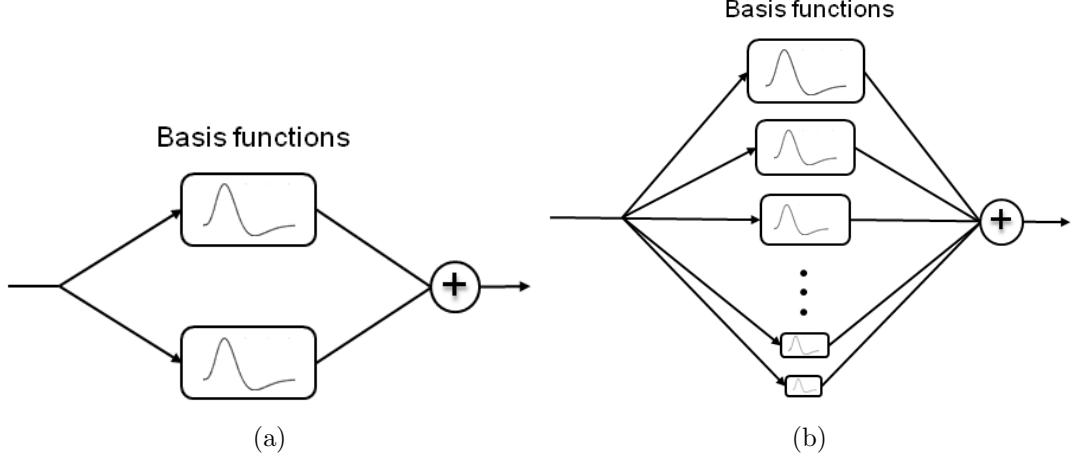
Figure 3.5: The structures of hemodynamic response functions: (a) typical HRF and (b) extended HRF. The extended HRF consists of many basis functions while the typical HRF comprises just two basis functions. The long memory condition of extended HRF in theorem 7 states that the coefficients of each basis functions slowly decrease.

Poisson function yields similar results with Gamma function when a BOLD signal is fitted into stimulation (Rajapakse et al., 1998). The following theorem 7 states the long memory condition of hemodynamic response.

Theorem 7 (Quasi long memory condition of HRF). *Suppose that the impulse function $g(t)$ in (3.2) consists of Poisson functions defined in (3.3) as basis functions. If the coefficient of each basis function satisfies for $d \in \mathbb{R}$*

$$\kappa_j = \frac{d}{\Gamma(d+1)} a_j^{d-1}, \tag{3.4}$$

and M is sufficiently large or $M \to \infty$ and $a_j = j + \alpha$ for $0 < \alpha \leq 1$, $g(t)$ in (3.2) can be approximated by

$$g(t) \approx \frac{d}{\Gamma(d+1)\Gamma(t+1)} \left(\Gamma(t+d) + \sum_{k=0}^{\infty} \zeta(-t-d-k+1, \alpha) \frac{(-1)^k}{k!} \right) \tag{3.5}$$

where ζ denotes the Hurwitz zeta function defined as

$$\zeta(s, q) = \sum_{k=0}^{\infty} (k + q)^{-s} \tag{3.6}$$

Proof. $g(t)$ is represented from (3.2), (3.3) and (3.4) by

$$
\begin{aligned}
g(t) &= \sum_{j=1}^{M} \left(\frac{d}{\Gamma(d+1)} a_j^{d-1} \right) \left(\frac{a_j^t e^{-a_j}}{\Gamma(t+1)} \right) \\
&= \frac{d}{\Gamma(d+1)\Gamma(t+1)} \sum_{j=1}^{M} a_j^{t+d-1} e^{-a_j} \\
&= \frac{d e^{-\alpha}}{\Gamma(d+1)\Gamma(t+1)} \sum_{j=1}^{M} (j + \alpha)^{t+d-1} e^{-j}.
\end{aligned} \tag{3.7}
$$

Let $p(t)$ is defined as

$$p(t) \doteq \sum_{j=1}^{\infty} (j + \alpha)^{t+d-1} e^{-j}. \tag{3.8}$$

Then, $p(t)$ can be represented by

$$p(t) = \Phi\left(e^{-1}, -t - d + 1, \alpha\right) \tag{3.9}$$

where Φ denotes the Lerch transcendent (Johnson, 1974) defined as

$$\Phi(z, s, q) \doteq \sum_{k=0}^{\infty} z^k (k + q)^{-s}. \tag{3.10}$$

According to the Erdélyi's formula (Erdélyi et al., 1953, vol.1, p. 29),

$$\Phi(z, s, q) = \Gamma(1 - s) z^{-\alpha} (-\log z)^{s-1} + z^{-\alpha} \sum_{k=0}^{\infty} \zeta(s - k, \alpha) \frac{(\log z)^k}{k!} \tag{3.11}$$

for $|\log z| < 2\pi$, $0 < \alpha \leq 1$, and $s \neq 1, 2, 3, \cdots$. Thus,

$$p(t) = e^{\alpha} \left(\Gamma(t + d) + \sum_{k=0}^{\infty} \zeta(-t - d - k + 1, \alpha) \frac{(-1)^k}{k!} \right). \tag{3.12}$$

As $M \to \infty$, $g(t)$ can be approximated from (3.7) and (3.12) by

$$g(t) \approx \frac{de^\alpha}{\Gamma(d+1)\Gamma(t+1)} \times p(t).$$ (3.13)

Hence, the claim follows from (3.12) and (3.13). $\qquad\square$

From theorem 7, the HRF can be split into two parts $r(t)$ and $q(t)$ as follows

$$g(t) \approx r(t) + q(t)$$ (3.14)

where

$$r(t) \doteq \frac{d\Gamma(t+d)}{\Gamma(d+1)\Gamma(t+1)}, \quad \text{and}$$ (3.15)

$$q(t) \doteq \frac{d}{\Gamma(d+1)\Gamma(t+1)} \sum_{k=0}^{\infty} \zeta\left(-t-d-k+1, \alpha\right) \frac{(-1)^k}{k!}.$$ (3.16)

Likewise, the output BOLD response $x(t)$ can be regarded as the sum of two components like

$$\begin{aligned} x(t) &= g(t) * u(t) = (r(t) + q(t)) * u(t) \\ &= r(t) * u(t) + q(t) * u(t) \\ &\doteq x^{(L)}(t) + x^{(N)}(t) \end{aligned}$$ (3.17)

Corollary 3. $x^{(L)}(t) \doteq r(t) * u(t)$ *given in* (3.17) *can be represented in terms of fractional difference as follows*

$$x^{(L)}(t) \doteq r(t) * u(t) = (1 - \mathcal{B})^{-d} u(t)$$ (3.18)

where $\mathcal{B}^\tau x(t) = x(t - \tau)$ *and*

$$(1 - \mathcal{B})^{-d} = \sum_{\tau=0}^{\infty} \binom{-d}{\tau} (-1)^\tau \mathcal{B}^\tau.$$ (3.19)

Proof. From (3.15),

$$r(t) = \frac{d\Gamma(t+d)}{\Gamma(d+1)\Gamma(t+1)} = \binom{-d}{t}(-1)^t \qquad (3.20)$$

since

$$\binom{-d}{t} = (-1)^t\binom{d+t-1}{t} \text{ and } \binom{t+d-1}{t} = \frac{d\Gamma(t+d)}{\Gamma(t+1)\Gamma(d+1)}.$$

From (3.17),

$$\begin{aligned}
x^{(L)}(t) &= \sum_{\tau=0}^{\infty} r(\tau)u(t-\tau) \\
&= \sum_{\tau=0}^{\infty}\binom{-d}{t}(-1)^{\tau}u(t-\tau) = \sum_{\tau=0}^{\infty}\binom{-d}{t}(-1)^{\tau}\mathcal{B}^{\tau}u(t). \quad (3.21)
\end{aligned}$$

Hence, the claim follows from (3.19) and (3.21). $\qquad\square$

In Corollary 3, the fractional difference representation of $x^{(L)}(t)$ resembles the definition of fractionally integrated (FI) process introduced in Section 2.7.2.2. Indeed, $x^{(L)}(t)$ becomes identical to the FI process in the case that $d \in (-0.5, 0.5)$ and $u(t)$ satisfies the short memory condition as defined below.

Definition 8 (Short memory process)**.** Let $u(t)$ be a real-valued discrete time weakly stationary process with zero mean whose correlation function $\gamma_u(\tau) = \mathbb{E}\left[u(t)u(t+\tau)\right]$ satisfies for all t and τ

$$\sum_{\tau=-\infty}^{\infty}\gamma_u(\tau) < \infty. \qquad (3.22)$$

Then, $u(t)$ is called the *short memory process* (Baillie, 1996). If the spectral density of $u(t)$ is nonzero, i.e. $f_u(\lambda) \neq 0$, $\forall\lambda \in (-1/2, 1/2)$, $u(t)$ is called the *short memory process with nonzero spectral density*.

Lemma 8 (Spectral density of short memory process)**.** *Let $u(t)$ be a short memory process with nonzero spectral density. The spectral density of $u(t)$ is bounded, bounded away from zero and continuous at $\lambda = 0$.*

Proof. Let $f_u(\lambda)$ be a spectral density of $u(t)$ defined by

$$f_u(\lambda) \doteq \int_{-\infty}^{\infty} \gamma_u(\tau) e^{-i\lambda\tau} \mathrm{d}\tau \tag{3.23}$$

where $\gamma_u(\tau)$ is the autocorrelation function of $u(t)$. Then, $f_u(\lambda)$ is continuous at $\lambda = 0$ because

$$\lim_{\lambda \to 0} f_u(\lambda) = \int_{-\infty}^{\infty} \gamma_u(\tau) \mathrm{d}\tau < \infty \tag{3.24}$$

from the definition 8 of short memory process. If there exists $\lambda_0 \in (-1/2, 1/2)$ such that $f_u(\lambda_0) = \infty$, it contradicts the assumption in (3.22) because

$$\gamma(\tau) = \frac{1}{2\pi} \int_{-\infty}^{\infty} f_u(\lambda) e^{i\lambda\tau} \mathrm{d}\lambda \to \infty \tag{3.25}$$

from Parseval's theorem. Hence, $f_u(\lambda_0) < \infty$ for all λ, and $f_u(\lambda)$ is bounded away from zero according to the definition of $u(t)$. $\qquad\square$

Remark 2. Let $r(t)$ be a function given in (3.15) with $d \in (-0.5, 0.5)$, and $u(t)$ be a short memory process with nonzero spectral density. Then, the filtered series $x^{(L)}(t)$ of $u(t)$ with $r(t)$ in (3.18) is an FI process with memory parameter d.

Proof. From Lemma 8, the short memory process $u(t)$ has the spectral density which is bounded, bounded away from zero and continuous at $\lambda = 0$. Since $d \in (-0.5, 0.5)$, $x^{(L)}(t) \doteq r(t) * u(t)$ satisfies the condition of being a FI process from Definition 6. $\qquad\square$

Remark 2 implies that $x^{(L)}(t)$ is perfectly described as an FI process. In particular, if $d \in (0, 0.5)$, the autocovariance of $x^{(L)}(t)$ satisfies $\rho(\tau) \propto |\tau|^{2d-1}$ as $|\tau| \to \infty$ and the spectral density of $x(t)$ satisfies $f_x(\lambda) \propto |\lambda|^{-2d}$ at the vicinity of origin. In this case, $x^{(L)}(t)$ is said to have *long memory* while $u(t)$ is called the *short memory* part. The long memory property is characterized by the memory parameter d. For mathematical definition and properties of the FI process, refer to Section 2.7.2.2.

Therefore, it is obvious that the long memory properties of the BOLD signal $x(t)$ driven by hemodynamics is attributed to the HRF component $r(t)$ in (3.15). However, the other component $q(t)$ of HRF disturbs the fractal pattern in $x(t)$
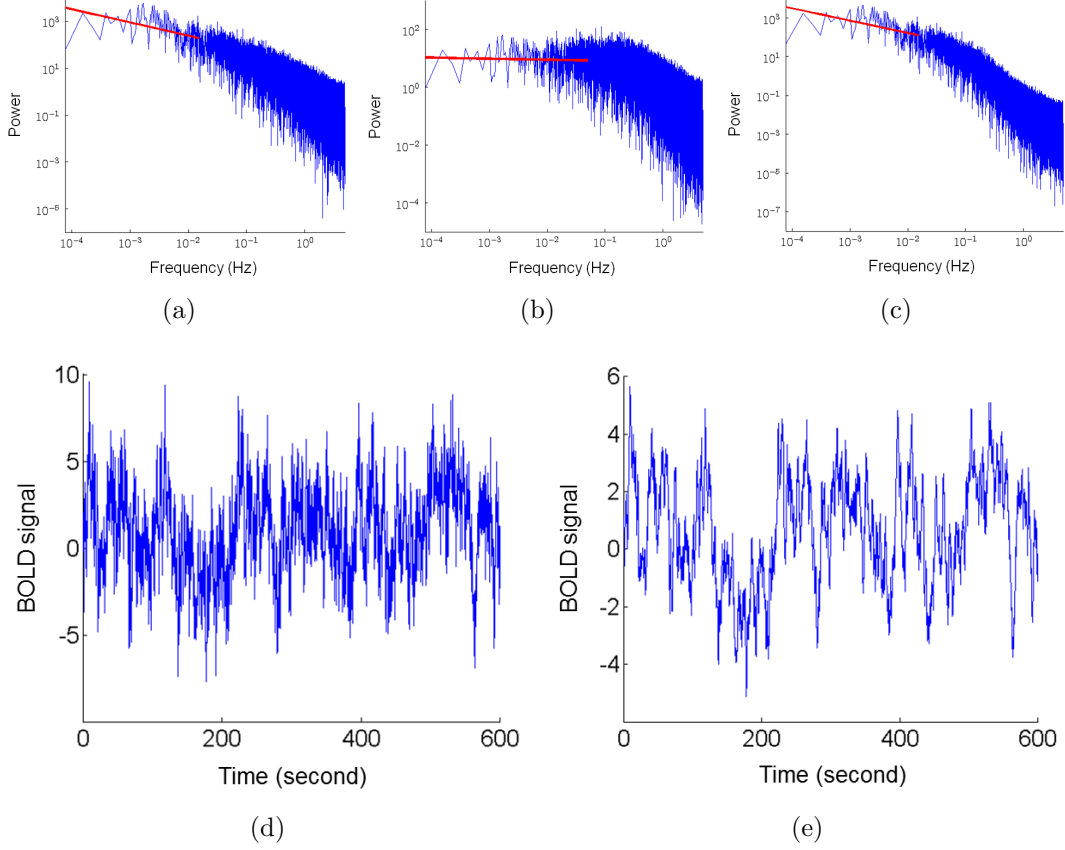
Figure 3.6: The split of memory and noise components in HRF: the power spectrums (a) of memory part $x^{(L)}(t)$, (b) of noise part $x^{(N)}(t)$, and (c) of their sum $x(t)$ when the HRF $g(t)$ was set with $M = 100$ and $d = 0.3$. The values of memory parameter estimated by the periodogram method were acceptably similar: $\hat{d} = 0.3166$ and $\hat{d}^{(L)} = 0.2812$. (d) and (e) show the time series of $x^{(L)}(t)$ and $x(t)$ respectively.

since it does not have fractal properties. Indeed, when $u(t)$ is given as a Gaussian white noise, the power spectral density (PSD) of $x^{(N)}(t)$ has the Lorentzian pattern while that of $x^{(L)}(t)$ exhibits the scale-invariance over frequencies (see Figure 3.6(a),(b)). The disturbance caused by $x^{(N)}(t)$ leads to the discrepancy between $x^{(L)}(t)$ and $x(t)$ in high frequencies; in other words, it distracts the output BOLD response $x(t)$ from fractal pattern (see Figure 3.6(c)). In this reason, $q(t)$ is called the *noise component* of HRF $g(t)$ while $r(t)$ is called the *memory component*. When $r(t)$ is dealt as an approximation of HRF, it is called the *long memory filter* (LMF).
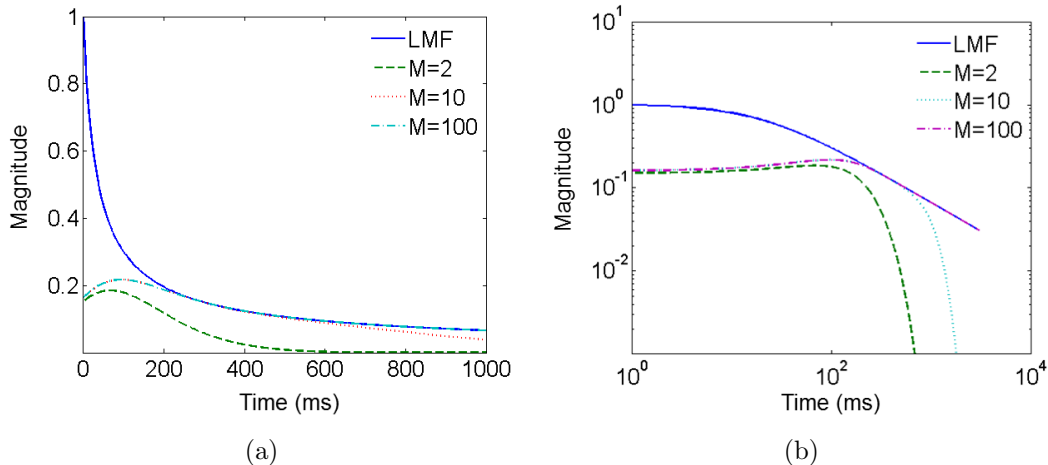
Figure 3.7: Effects of the number of basis functions on the curve of HRF with long memory. HRFs $g(t)$ with a variety of M were compared with LMF $r(t)$ (a) in time domain and (b) in log-scale.

In spite of this perturbation of fractal behavior, the scale-invariance is less affected in low frequencies by the noise component $q(t)$. In the simulation study, the estimated memory parameter of $x(t)$ was nearly equal to that of $x^{(L)}(t)$ (see Figure 3.6). Therefore, the condition of HRF given in theorem 7 can be regarded as the *quasi long memory condition* because the pure memory part is disturbed in high frequencies by the additive noise component and the fractal pattern can be detected just in low frequencies.

Figure 3.7 illustrates how the time curve of HRF $g(t)$ is different from that of LMF $r(t)$. There exists a large gap in initial time points between HRF and LMF; the gap is not made narrow even when the number of basis functions is sufficiently larger, however it exerts an influence on high frequency activities of BOLD responses (see Figure 3.6). The gap is propagated over longer time as the number of basis functions decreases. Finally, the decrease in M deteriorates the fractal function in HRF $g(t)$.

The curve of HRF $g(t)$ given in (3.2) is also dissimilar with the typical HRF in (2.3) (see Figure 3.8(a)). The curve of HRF satisfying the long memory condition in Theorem 7 has no undershoot but longer tail while the typical HRF has undershoot. How such a difference can be described by an unified theory is discussed in
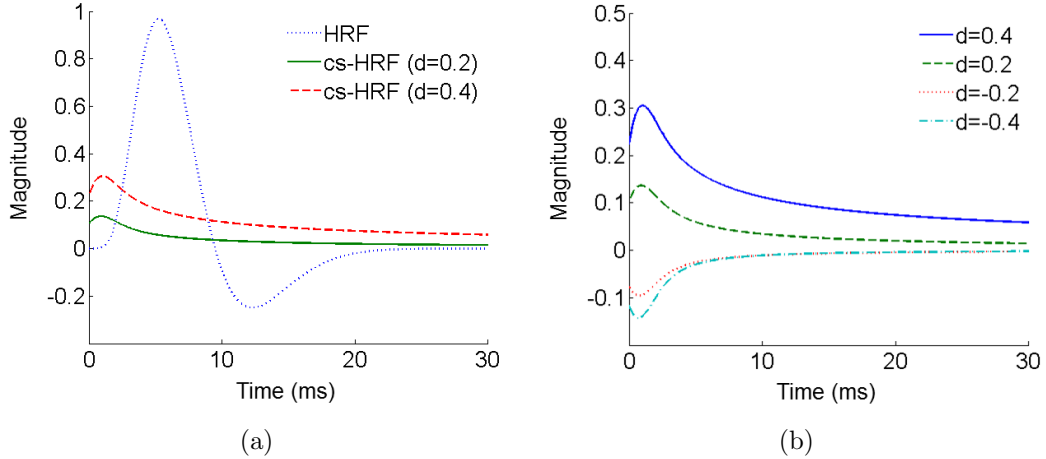
Figure 3.8: Effects of long memory condition on HRF curves: (a) the comparison of typical HRF and long memory HRF, and (b) variation of HRF curves controlled by the memory parameter.

Section 3.3. The curve of HRF is also controlled by the memory parameter d. As the absolute memory parameter $|d| \in (0, 0.5)$ increases, the degree of dispersion also increases, which strengthens the long memory effect in BOLD responses (see Figure 3.8(b)).

3.3 History dependent excitability of HRF

In Section 3.2.2, it was inferred that the long memory condition of HRF given in Theorem 7 is fairly different from that of typical HRF which has been broadly exploited for fMRI data analyses. It implies that the shape of impulse hemodynamic response may alter depending upon the previous history of brain activities. In the task-related hemodynamic response which is noticeably correlated with external stimuli, just two basis functions in the extended HRF (3.2) are most considerable and the others are negligible by suppressing their coefficients as shown in equation (2.3). On the other hand, more than two basis functions become relatively important in resting state since the coefficients κ_j of basis function in (3.2) decay slowly according to (3.4) so that the corresponding BOLD response exhibits long memory.

The assumption that the state of impulse hemodynamic response may be subject to the history of neuronal activity indicates that the hemodynamic system is no longer approximated as a linear time-invariant (LTI) system. Therefore, $x(t)$ in (3.1) can be rewritten as follows

$$x(t) = h(u(t), u(t-1), \cdots) \approx \sum_{\tau=0}^{\infty} g(\tau; \mathcal{H}_t) u(t-\tau), \qquad (3.26)$$

where $\mathcal{H}_t$ denotes the history of $u(t)$ since $t = 0$, and and $g(\tau; \mathcal{H}_t)$ is called the *dynamic hemodynamic response function* (dHRF) whose shape is dynamically determined depending on $\mathcal{H}_t$. This hypothesis is called the *history dependent excitability* (HDE) of hemodynamic response[1], and states that a BOLD response is produced through history-dependent hemodynamics. The HDE may be one of causes of either between-session or between-subject variability in task-related BOLD responses; in other words, BOLD responses to stimulation may differ in a brain region over time according to the past resting state.

It is unclear how the dependence of hemodynamic response on history is quantified and what attributes of neuronal history directly change the parameters of HRF. A possible assumption is that the hemodynamic response is adapted to the history of neuronal activities and always check the predictability of input at the subsequent time. If the current input were predictable based on history, it does not lead to the change of HRF. For example, when neuronal activity has no significant deterministic trend but stationary random work (such as Poisson point process), the state of HRF may approach to the quasi long memory condition described in Theorem 7 (see Figure 3.9(a),(b),(c)). On the other hand, an abrupt change in deterministic trend of neuronal activity $u(t)$ deteriorates the predictability of input, and may make the shape of HRF more similar with typical HRF given in (2.3) (see Figure 3.9(d),(e),(f)).

In spite of the ambiguity of dependent relationship between neuronal activities and hemodynamics, a particular condition implying the strong dependence

---

[1] The terminology of history dependent excitability was originally coined by Baroni et al. (2010) to describe the propensity to transient neuronal firing dependent on history. In this thesis, this concept is adopted to describe the dependence of hemodynamic state on the history of neuronal activities.
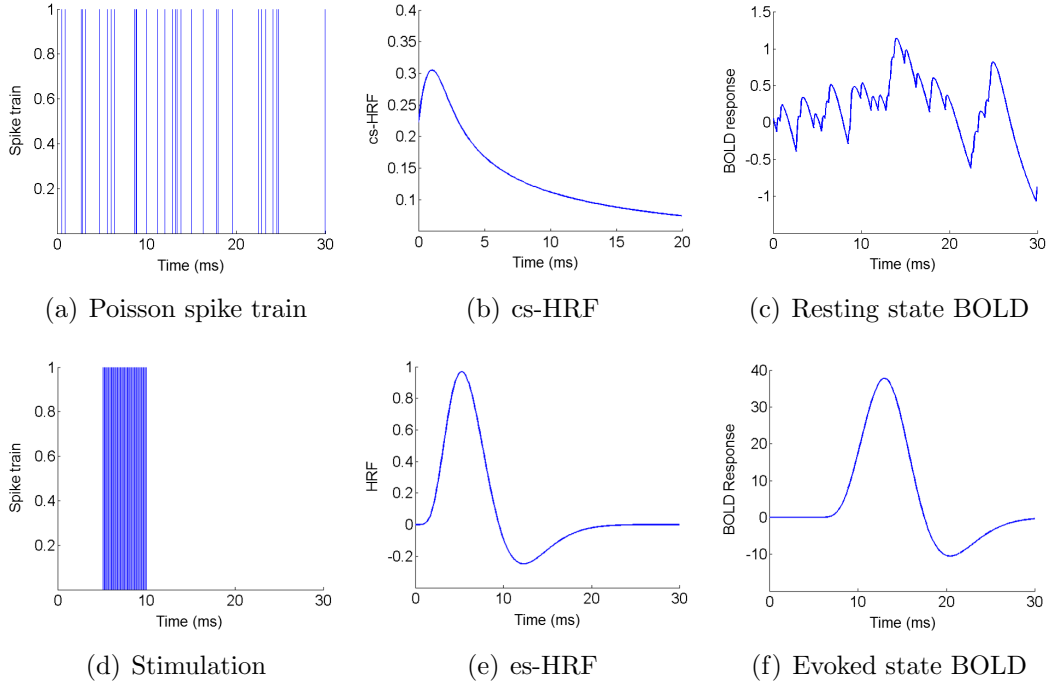
Figure 3.9: Examples of history dependent excitability of hemodyamic response. (a-c) Stationary spike trains discharged with Poisson rate induces the quasi long memory condition of HRF (called the cs-HRF), and results in long memory in the corresponding BOLD signal. (d-f) The 5 second stimulation changes the shape of HRF from cs-HRF to the typical evoked state HRF.

between them can be inferred from the following proposition 9.

Proposition 9 (Inference of hemodynamic long memory state). *Let $u(t)$ be a short memory function and $x(t)$ be a filtered series of $u(t)$ with a real-valued function $r_{(G)}(t)$; that is, $x(t) = r_{(G)}(t) * u(t)$. If there exist $d \in (-0.5, 0.5)$ such that the spectral density of $x(t)$ satisfies*

$$f(\lambda) \propto \lambda^{-2d}, \quad \lambda \to 0_+, \tag{3.27}$$

the filter $r_{(G)}(t)$ can be represented in low frequencies by the convolution of a short memory function $\beta(t)$ with $r(t)$ given in (3.15) as follows

$$r_{(G)}(t) \sim r(t) * \beta(t). \tag{3.28}$$

Proof. The condition (3.27) can be rewritten by

$$f(\lambda) \approx \alpha(\lambda)\lambda^{-2d}, \quad \lambda \to 0_+, \tag{3.29}$$

where $\alpha(\lambda)$ is a positive continuous bounded function satisfying $\alpha(\lambda) \to \kappa$ as $\lambda \to 0_+$ for $\kappa \in \mathbb{R}$. Since $\left(1 - e^{-i\lambda}\right)^\alpha = \lambda^\alpha e^{i\pi\alpha/2}\left(1 + O(\lambda)\right)$,

$$
\begin{aligned}
f(\lambda) &\approx \alpha(\lambda)\lambda^{-2d} = \left(\lambda^{-d}e^{i\pi d/2}\right)\alpha(\lambda)\left(\lambda^{-d}e^{-i\pi d/2}\right) \\
&\sim \left(1 - e^{-i\lambda}\right)^{-d}\alpha(\lambda)\left(1 - e^{i\lambda}\right)^{-d}
\end{aligned}
\tag{3.30}
$$

From the condition $x(t) = r_{(G)}(t) * u(t)$, $f(\lambda)$ satisfies

$$f(\lambda) = f_g(\lambda)f_u(\lambda) \tag{3.31}$$

where $f_g(\lambda)$ and $f_u(\lambda)$ denote spectral densities for $r_{(G)}(t)$ and $u(t)$ respectively. From (3.30) and (3.31),

$$
\begin{aligned}
f_g(\lambda) &\sim \left(1 - e^{-i\lambda}\right)^{-d} f_\beta(\lambda) \left(1 - e^{i\lambda}\right)^{-d} \\
&= \left(\sum_{k=0}^\infty \frac{\Gamma(t+d)}{\Gamma(d)k!}e^{-i\lambda k}\right) f_\beta(\lambda) \left(\sum_{k=0}^\infty \frac{\Gamma(t+d)}{\Gamma(d)k!}e^{i\lambda k}\right)
\end{aligned}
\tag{3.32}
$$

where $f_\beta(\lambda) = \alpha(\lambda)/f_u(\lambda)$. Since $f_\beta(\lambda)$ is continuous at $\lambda = 0$, bounded and bounded away from zero, $f_\beta(\lambda)$ can be regarded as the spectral density of a short memory function $\beta(t)$. Therefore, (3.28) follows because (3.32) is equivalent to

$$r_{(G)}(t) = \sum_{k=0}^\infty \frac{\Gamma(d+k)}{\Gamma(d)k!}\beta(t-k) = \sum_{k=0}^\infty r(k)\beta(t-k) \tag{3.33}$$

(Hannan, 1970). □

Proposition 9 states that the the HRF $r_{(G)}(t)$ can be represented by a sequence of short memory $\beta(t)$ and long memory filters $r(t)$ if the neuronal activity $u(t)$ is a short memory function and the corresponding BOLD response $x(t)$ exhibits long memory in low frequencies. Hence, $r_{(G)}(t)$ can be considered as the generalization of the memory part $r(t)$ of HRF in (3.15) since the HRF $r_{(G)}(t)$ includes short

memory $\beta(t)$ as well as long memory component $r(t)$ while $r(t)$ contains just long memory component. The short memory component $\beta(t)$ of HRF may hinder us from estimating the short memory properties of neuronal activities from resting state BOLD signals since the neuronal activity may be blended with short memory induced by hemodynamics and cannot be easily separated as shown in

$$x_L(t) = r_{(G)}(t) * u(t) = r(t) * (\beta(t) * u(t)). \tag{3.34}$$

Proposition 9 also has important implication such that the short memory condition of neuronal activities always leads to the long memory condition of hemodynamics as long as the long memory phenomenon is observed in BOLD signals. The long memory in BOLD signals does not always indicate that neuronal activity consists of short memory attributes; indeed, it may comprise both short memory and long memory components.

The dependence of hemodynamic response upon the history of neuronal activities has been discussed so far. It is clear that the HDE makes it difficult to simplify the hemodynamics as an LTI system. However, if the impulse response $g(\tau; \mathcal{H}_t)$ is kept approximately constant over a time interval, in other words, $g(t; \mathcal{H}_t) \approx [g(t)]_{t=t_A}$ for $t \in [t_A, t_B]$, the hemodynamic kernel can be regarded as an LTI system for the given period. It is reasonable to assume that the impulse response $g(\tau; \mathcal{H}_t)$ would be nearly constant during a normal fMRI-scanning period unless an unpredictable change in neuronal activities happens due to sudden interference or irregular endogenous cognitive behavior. This assumption allows us to regard the hemodynamic system as an LTI system during one fMRI measurement.

Now let us go back to Theorem 7 on the long memory condition of cerebral hemodynamics. If the dHRF in (3.26) satisfies the quasi long memory condition of Theorem 7 and the input neuronal activity satisfies the short memory condition given in Definition 8, the dHRF is said to be *at the critical state* where the output BOLD signal exhibits fractal behavior in low frequencies, and is called the *critical-state hemodynamic response function* (cs-HRF). As its contrary concept, the typical HRF in (2.3) is called the *evoked-state hemodynamic response function* (es-HRF). Hence, both es-HRF and cs-HRF are special cases of dHRF. At the
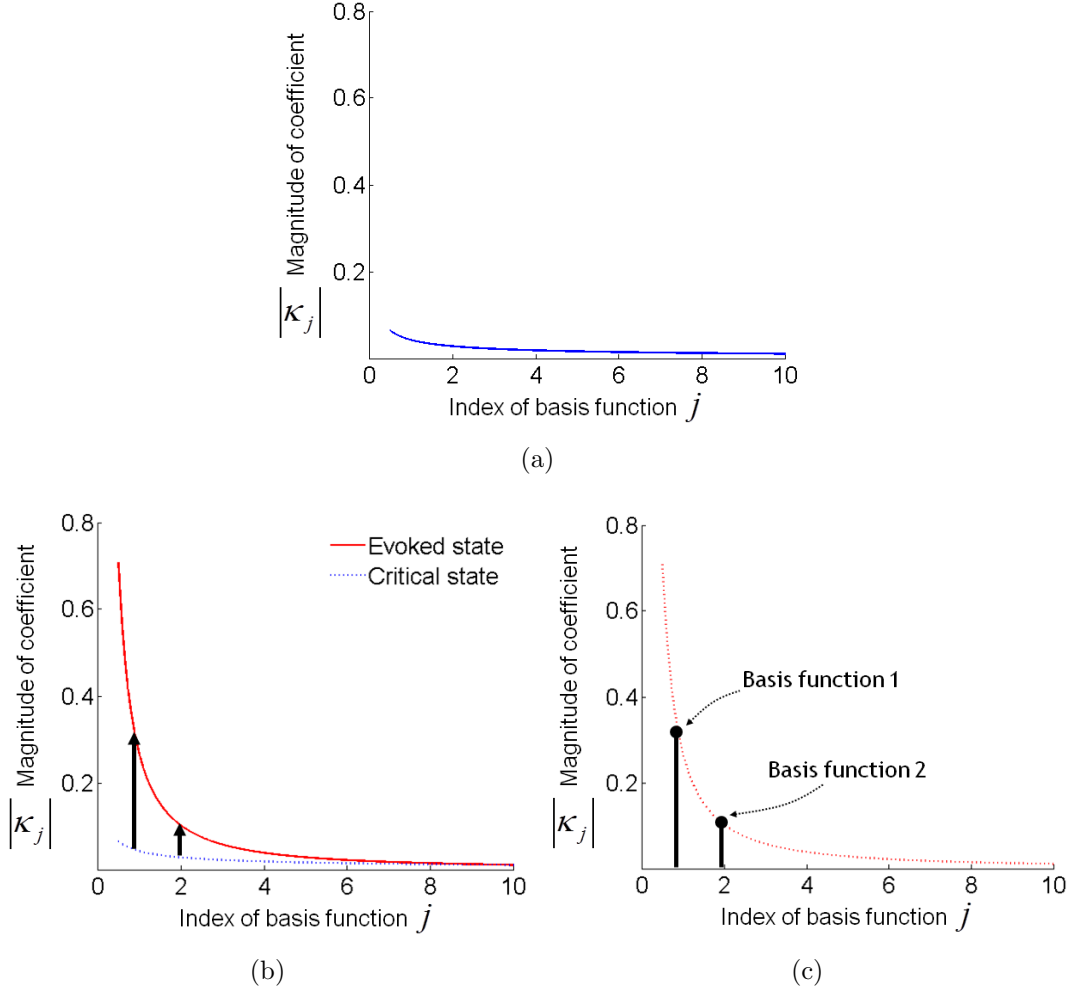
Figure 3.10: Properties of the resting state HRF. (a) the effect of the number of basis functions, and (b) the plots of rs-HRF with different memory parameter.

critical state, the coefficients of basis functions is arranged according to (3.4) (see Figure 3.10(a)). As a stimulation is assigned to the brain region, the coefficients of some basis functions increase abruptly (see Figure 3.10(b)), and finally the HRF can be approximated as the sum of two basis functions like the typical HRF (see Figure 3.10(c)).

Let us remind a remark in Section 1 such that a resting state BOLD signal tends to exhibit fractal behavior or scale invariance. Based on this remark and the assumption that the fractal behavior is mainly caused by cerebral hemodynamics,

it can be supposed that dHRF tends to approach to the critical state when the output BOLD signal is taken at rest. However, it should be noticed that a resting state BOLD signal does not necessarily exhibit such long memory phenomenon; the long-range dependence is sometimes interfered by endogenous brain activities, which makes the BOLD signal to be nonstationary and irregular. The state of dHRF wanders usually in the vicinity of the critical point of hemodynamics. Strictly speaking, a resting state BOLD signal is not always regarded as a fractal process in the statistical view.

3.4 Nonlinear long memory model of hemodynamic response

In Section 3.2, a special long memory condition of resting state BOLD signal has been modeled as a linear convolution of short memory neuronal activity with cs-HRF. In reality, the cerebral hemodynamics is not such a linear system, but can be regarded as a dynamic system through which a BOLD signal is nonlinearly correlated with neuronal population activities. From the statistical point of view, any nonlinear physiological system can be nonparametrically represented by the Volterra series (Marmarelis, 2004). Likewise, a BOLD signal can be described as a nonlinear convolution of neuronal population activities with Volterra kernels. The Volterra series representation of BOLD signals has been established by Friston et al. (1998); Josephs & Henson (1999). The nonlinear model is independent from the physical mechanism of hemodynamics while the Balloon/Windkessel model consists of differential equations associated with blood volume, flow and deoxyhemoglobin quantity (see Section 2.1.2). Nonetheless, it is useful to figure out the influence of nonlinearity on long memory properties of resting state BOLD signals.

Let $x'(t)$ be a predicted BOLD signal corresponding to neuronal population activity $u(t)$ at a time t. If we assume that the output $x(t)$ depends only on past values of inputs, the output $x'(t)$ can be written as a nonlinear convolution of

input $u(t)$ and the n-th order Volterra kernel $h_n(\tau_1, \cdots, \tau_n)$ as follows

$$
\begin{aligned}
x'(t) &= h\left(u(t), u(t-1), \cdots\right) \\
&= \sum_{n=1}^{\infty} \left(\sum_{\tau_1=0}^{\infty} \cdots \sum_{\tau_n=0}^{\infty} h_n(\tau_1, \cdots, \tau_n) \prod_{j=1}^{n} u(t-\tau_j) \right)
\end{aligned}
\tag{3.35}
$$

The expansion of the Volterra kernels with M basis functions $\{v_1(t), \cdots, v_M(t)\}$ produces

$$
h_n(\tau_1, \cdots, \tau_n) = \sum_{b_1=1}^{M} \cdots \sum_{b_n=1}^{M} \kappa_{b_1, \cdots, b_n} \prod_{j=1}^{n} v_{b_j}(\tau_j)
\tag{3.36}
$$

where M is the number of basis functions, $\kappa_{b_1, \cdots, b_n}$ denotes an *expansion coefficient* and $v_b(t)$ represents the bth basis function ([Marmarelis, 2004](#)).

Proposition 10 (Approximated Volterra series). *If the expansion coefficients in* (3.36) *satisfy the following condition*

$$
\kappa_{b_1, \cdots, b_n} \approx a_n \prod_{k=1}^{n} \kappa_{b_k},
\tag{3.37}
$$

$x'(t)$ *can be approximated by*

$$
\begin{aligned}
x'(t) &\approx \sum_{n=1}^{\infty} a_n \left(x(t)\right)^n \\
&= a_1 x(t) + a_2 \left(x(t)\right)^2 + a_3 \left(x(t)\right)^3 + \cdots \\
&\doteq \mathcal{V}\left[x(t)\right]_{\mathbf{a}}
\end{aligned}
\tag{3.38}
$$

where $x(t)$ *is given in* (3.1), *and* $\mathcal{V}\left[\cdot\right]_{\mathbf{a}}$ *is called the approximate Volterra operator with order coefficients* $\mathbf{a} = \{a_1, a_2, \cdots\}$.

Proof.

$$
\begin{aligned}
x'(t) &= \sum_{n=1}^{\infty}\sum_{\tau_1=0}^{\infty}\cdots\sum_{\tau_n=0}^{\infty}\left(\sum_{b_1=1}^{M}\cdots\sum_{b_n=1}^{M}\kappa_{b_1,\cdots,b_n}\prod_{j=1}^{n}v_{b_j}(\tau_j)\right)\prod_{j=1}^{n}u(t-\tau_j) \\
&= \sum_{n=1}^{\infty}\sum_{b_1=1}^{M}\cdots\sum_{b_n=1}^{M}\kappa_{b_1,\cdots,b_n}\left(\sum_{\tau_1=0}^{\infty}\cdots\sum_{\tau_n=0}^{\infty}\prod_{j=1}^{n}v_{b_j}(\tau_j)u(t-\tau_j)\right) \\
&= \sum_{n=1}^{\infty}\sum_{b_1=1}^{M}\cdots\sum_{b_n=1}^{M}\kappa_{b_1,\cdots,b_n}\prod_{j=1}^{n}\left(\sum_{\tau=0}^{\infty}v_{b_j}(\tau)u(t-\tau)\right)
\end{aligned}
$$

From (3.37), $x'(t)$ can be rearranged as follows

$$
\begin{aligned}
x'(t) &= \sum_{n=1}^{\infty}\sum_{b_1=1}^{M}\cdots\sum_{b_n=1}^{M}\left(a_n\prod_{k=1}^{n}\kappa_{b_k}\right)\prod_{j=1}^{n}\left(\sum_{\tau=0}^{\infty}v_{b_j}(\tau)u(t-\tau)\right) \\
&= \sum_{n=1}^{\infty}a_n\sum_{b_1=1}^{M}\cdots\sum_{b_n=1}^{M}\prod_{k=1}^{n}\left(\sum_{\tau=0}^{\infty}\kappa_{b_k}v_{b_k}(\tau)u(t-\tau)\right) \\
&= \sum_{n=1}^{\infty}a_n\prod_{k=1}^{n}\sum_{b_k=1}^{M}\left(\sum_{\tau=0}^{\infty}\kappa_{b_k}v_{b_k}(\tau)u(t-\tau)\right) \\
&= \sum_{n=1}^{\infty}a_n\prod_{k=1}^{n}\sum_{\tau=0}^{\infty}\left(\sum_{b_k=1}^{M}\kappa_{b_k}v_{b_k}(\tau)\right)u(t-\tau) \\
&= \sum_{n=1}^{\infty}a_n\prod_{k=1}^{n}\left(\sum_{\tau=0}^{\infty}g(\tau)u(t-\tau)\right) = \sum_{n=1}^{\infty}a_n\prod_{k=1}^{n}x(t) \qquad (3.39)
\end{aligned}
$$

$\square$

The equation (3.38) shows that $x'(t)$ can be decomposed into powers of linear component $x(t)$ and can be reduced into a linear component $x(t)$ if the higher-order Volterra kernels are ignored. Now the following question can be settled: does the nonlinearity in cerebral hemodynamics influence the fractal behavior in resting state BOLD signals? Theorem 11 gives an answer for this question.

Theorem 11 (Long memory in nonlinear time series). *Suppose that $x(t)$ has the spectral density where $f(\lambda) \propto |\lambda|^{-2d}$ as $\lambda \to 0$ where $d \in (0, 1/2)$. Then,*

$x'(t) \doteq \mathcal{V}\left[x(t)\right]_A$ *also has the spectral density such that*

$$f'(\lambda) \propto |\lambda|^{-2d}, \quad \lambda \to 0. \tag{3.40}$$

Proof. The claim can be proved by showing that $f'(\alpha\lambda) \propto \alpha^{-2d} f'(\lambda)$. From the assumption, the spectral density $f(\lambda)$ can be rewritten by $f(\lambda) \approx a_f |\lambda|^{-2d}, \quad \lambda \to 0$. From (3.38),

$$f'(\lambda) = \sum_{n=1}^{\infty} a_n \underbrace{(f(\lambda) * \cdots * f(\lambda))}_{n \text{ times}} = \sum_{n=1}^{\infty} a_n C_n(\lambda) \tag{3.41}$$

where $C_n(\lambda) \doteq f(\lambda) * \cdots * f(\lambda)$. Then,

$$C_n(\lambda) = \int_{-1/2}^{1/2} \cdots \int_{-1/2}^{1/2} f(\lambda_{b_{n-1}}) \prod_{j=2}^{n-1} f(\lambda_{b_{j-1}} - \lambda_{b_j}) f(\lambda - \lambda_{b_1}) d\lambda_{b_1} \cdots d\lambda_{b_{n-1}}. \tag{3.42}$$

Likewise,

$$
\begin{aligned}
C_n(\alpha\lambda) &= \int_{-1/2}^{1/2} \cdots \int_{-1/2}^{1/2} f(\lambda_{b_{n-1}}) \prod_{j=2}^{n-1} f(\lambda_{b_{j-1}} - \lambda_{b_j}) f(\alpha\lambda - \lambda_{b_1}) d\lambda_{b_1} \cdots d\lambda_{b_{n-1}} \\
&= \int_{-1/2}^{1/2} f(\alpha\lambda - \lambda_{b_1}) C_{n-1}(\lambda_{b_1}) d\lambda_{b_1}.
\end{aligned}
\tag{3.43}
$$

Since $f(\alpha\lambda - \lambda_{b_1}) \to a_f |\alpha\lambda|^{-2d}$ as $\lambda_{b_1} \to 0$ while $f(\alpha\lambda - \lambda_{b_1}) \to 0$ as $\lambda_{b_1} \to \infty$,

$$
\begin{aligned}
C_n(\alpha\lambda) &\approx \int_{-\delta}^{\delta} a_f |\alpha\lambda|^{-2d} C_{n-1}(\lambda_{b_1}) d\lambda_{b_1} \\
&= c_f |\lambda|^{-2d} \alpha^{-2d} = \kappa_f \alpha^{-2d} C_n(\lambda)
\end{aligned}
\tag{3.44}
$$

for a small positive number δ where $c_f \doteq a_f \int_{-\delta}^{\delta} C_{n-1}(\lambda_{b_1}) d\lambda_{b_1}$. Hence,

$$
\begin{aligned}
f'(\alpha\lambda) &= \sum_{n=1}^{\infty} a_n C_n(\alpha\lambda) \\
&\approx \kappa_f \alpha^{-2d} \sum_{n=1}^{\infty} a_n C_n(\lambda) = \kappa_f \alpha^{-2d} f'(\lambda)
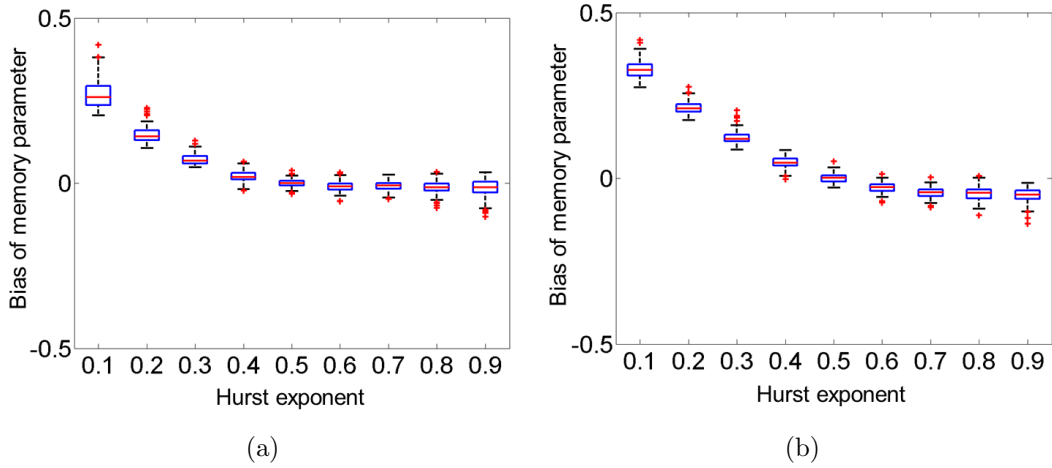\end{aligned}
\tag{3.45}
$$

Figure 3.11: Effects of nonlinear hemodynamics on fractal behavior: the bias of memory parameters (a) in the case of decreasing order coefficients $\mathbf{a} = \left\{1, e^{-1}, e^{-2}\right\}$, and (b) in the case of increasing coefficients $\mathbf{a} = \left\{1, e, e^2\right\}$.

$\square$

Theorem 11 indicates that the nonlinearity in a physiological system has little influence on the long memory phenomenon. Therefore, the sum $x(t)$ of all nonlinear components in (3.38) is no longer an FI process, but still has long memory with the memory parameter $d \in (0, 1/2)$. A simulation study, as illustrated in Figure 3.11, demonstrates that the memory parameter estimated from nonlinear long memory processes given in (3.38) is less affected by the distribution of order coefficients. Figure 3.11, however, shows that the nonlinearity can have significant impacts on the fractal behavior of FI processes when $d \in (-1/2, 0)$.

3.5   Long memory and functional connectivity

The long memory models of hemodynamic response, discussed in sections 3.2 to 3.4, enable us to figure out how the fractal behavior of cerebral hemodynamics has an effect on resting state functional connectivity in fMRI. In this section, the association between long memory and functional connectivity is theoretically inferred based on the proposed statistical model of resting state hemodynamic response. In special, the FI process model is compared with the FGN model fo-

cusing on the relevance with functional connectivity. These theoretical inferences are demonstrated through simulation studies.

3.5.1 Theoretical inference

Let $\mathbf{x}(t) = \{x_1(t), \cdots, x_N(t)\}$ be a set of N resting state BOLD signals. In practice, its corresponding neuronal population activities are either a nonstationary or stationary process, but cannot be simply modeled as an *i.i.d.* process.

In spite of the nonstationarity, let us consider a virtual case such that the neuronal activities $\mathbf{u}(t) = \{u_1(t), \cdots, u_N(t)\}$ can be approximated as a set of Gaussian white noise processes so as to facilitate theoretical inference for the impact of fractal behavior on functional connectivity. In this case, the memory component $x^{(L)}(t)$ of a resting state BOLD signal, acquired by convolving $\mathbf{u}(t)$ with HRF $\mathbf{g}(t) = \{g(t; d_i); i = 1, \cdots, p\}$ in (3.2), can be modeled as a multivariate fractionally integrated noise (FIN) (see Section 2.7.2.2).

Theorem 12 (Connectivity distortion in FI processes)**.** *Let* $\mathbf{u}(t) \doteq \{u_i(t); i = 1, \cdots, p\}$ *be a vector white noise process, and* $\mathbf{x}^{(L)}(t) \doteq \left\{x_i^{(L)}(t); i = 1, \cdots, p\right\}$ *be a vector weakly stationary process such that* $x_i^{(L)}(t) = r(t; d_i) * u_i(t)$ *where* $r(t; d_i)$ *is given in* (3.15) *with* $|d_i| < 1/2$*. Then,* $\mathbf{x}^{(L)}(t)$ *is a multivariate fractionally integrated noise with memory parameter* $\mathbf{d} = [d_i]$*, and satisfies*

$$\frac{\gamma_{i,j}^{(x)}}{\gamma_{i,j}^{(u)}} \approx \frac{2^{d_i+d_j}}{1 - d_i - d_j} \cos\left(\frac{\pi}{2}(d_i - d_j)\right), \quad and \tag{3.46}$$

$$\frac{\rho_{i,j}^{(x)}}{\rho_{i,j}^{(u)}} \approx \frac{\sqrt{(1 - 2d_i)(1 - 2d_j)}}{1 - d_i - d_j} \cos\left(\frac{\pi}{2}(d_i - d_j)\right), \tag{3.47}$$

where $\gamma_{i,j}^{(u)} \doteq \mathrm{cov}\left\{u_i(t), u_j(t)\right\}$*,* $\rho_{i,j}^{(u)} \doteq \mathrm{cor}\left\{u_i(t), u_j(t)\right\}$*, and* $\gamma_{i,j}^{(x)}$ *and* $\rho_{i,j}^{(x)}$ *are also defined for* $x_i^{(L)}(t)$ *and* $x_j^{(L)}(t)$ *in the same manner.*

Proof. From the definition, $\mathbf{x}^{(L)}(t)$ is a vector fractionally integrated noise. Let $f_{i,j}(\lambda)$ be the cross-spectral density for $u_i(t)$ and $u_j(t)$, and $f'_{i,j}(\lambda)$ be the cross-spectral density for $x_i^{(L)}(t)$ and $x_j^{(L)}(t)$. Since $x_i^{(L)}(t) = r(t; d_i) * u_i(t)$,

$$f'_{i,j}(\lambda) = R_i(\lambda)R_j^*(\lambda)f_{i,j}(\lambda), \tag{3.48}$$

where $R_i(\lambda)$ denotes the transfer function of $r_i(t)$. Since $R_i(\lambda) = \left(1 - e^{-i\lambda}\right)^{-d_i}$ from Proposition 5,

$$
\begin{aligned}
f'_{i,j}(\lambda) &= \left(1 - e^{-i\lambda}\right)^{-d_i} \left(1 - e^{i\lambda}\right)^{-d_j} f_{i,j}(\lambda) \\
&= \left| 2 \sin \frac{\lambda}{2} \right|^{-d_1 - d_2} e^{i(d_i - d_j)(\lambda - \pi)/2} f_{i,j}(\lambda).
\end{aligned}
\tag{3.49}
$$

From the assumption on $\mathbf{u}(t)$, $f_{i,j}(\lambda) = \gamma_{i,j}^{(u)}$ for $|\lambda| \leq 1/2$. $f_{i,j}(\lambda)$ is bounded in $\lambda \in (-1/2, 1/2)$, bounded away from zero, and continuous at $\lambda = 0$. From (3.49), $\mathbf{x}^{(L)}(t)$ is a multivariate fractionally integrated noise with memory parameter $\mathbf{d}$ according to Definition 6. We also obtain the following approximation of $f'_{i,j}(\lambda)$ through the Taylor expansions

$$
\begin{aligned}
\Re\left[f'_{i,j}(\lambda)\right] &= \gamma_{i,j}^{(u)} \left| 2 \sin \frac{\lambda}{2} \right|^{-d_i - d_j} \cos\left(\frac{d_i - d_j}{2}(\lambda - \pi)\right) \\
&= \gamma_{i,j}^{(u)} \left(\left(\frac{\lambda}{2}\right)^{-\Sigma_d} + \frac{\Sigma_d}{6}\left(\frac{\lambda}{2}\right)^{2-\Sigma_d} + O(\lambda^3)\right) \\
&\quad \times \left(\cos(\Delta_d \pi) + \Delta_d \lambda \sin(\Delta_d \pi) + O(\lambda^2)\right) \\
&\approx \gamma_{i,j}^{(u)} \bigg(\cos(\Delta_d \pi)\lambda^{-\Sigma_d} + \Delta_d \sin(\Delta_d \pi)\lambda^{1-\Sigma_d} \\
&\quad + \frac{\Sigma_d}{24}\cos(\Delta_d \pi)\lambda^{2-\Sigma_d} + \frac{\Sigma_d}{6}\Delta_d \sin(\Delta_d \pi)\lambda^{3-\Sigma_d}\bigg),
\end{aligned}
\tag{3.50}
$$

where $\Sigma_d \doteq d_i + d_j$ and $\Delta_d \doteq (d_i - d_j)/2$. Hence, (3.46) follows from

$$
\begin{aligned}
\gamma_{i,j}^{(x)} &= \int_{-1/2}^{1/2} \Re\left[f'_{i,j}(\lambda)\right] \mathrm{d}\lambda \\
&\approx \gamma_{i,j}^{(u)} 2^{\Sigma_d} \bigg(\frac{\cos(\Delta_d \pi)}{1 - \Sigma_d} + \frac{1}{2}\frac{\Delta_d \sin(\Delta_d \pi)}{2 - \Sigma_d} \\
&\quad + \frac{\Sigma_d}{96}\frac{\cos(\Delta_d \pi)}{3 - \Sigma_d} + \frac{\Sigma_d}{48}\frac{\Delta_d \sin(\Delta_d \pi)}{4 - \Sigma_d}\bigg).
\end{aligned}
\tag{3.51}
$$

Likewise, (3.47) also follows from $\rho_{i,j}^{(x)} = \gamma_{i,j}^{(x)} / (\gamma_{i,i}^{(x)} \gamma_{j,j}^{(x)})^{1/2}$. $\qquad \square$

Theorem 12 shows that the correlation of BOLD signals between two brain

66

regions may differ from that of neuronal activities depending on the difference of memory parameters. In (3.47), the correlation $\rho_{i,j}^{(x)}$ of BOLD signals becomes zero when the memory difference is equal to one, i.e. $|d_i - d_j| = 1$. On the other hand, the correlation of BOLD signals becomes identical to that of neuronal activities in the case that the corresponding memory parameters are equal each other. Therefore, Theorem 12 states that the heterogeneous fractal behavior among brain regions causes the discrepancy in functional connectivity between BOLD signals and neuronal activities. It also implies that the maximum correlation of BOLD signals is limited depending on their memory parameters as shown in the following inequality

$$\rho_{i,j}^{(x)} \leq \frac{\sqrt{(1 - 2d_i)(1 - 2d_j)}}{1 - d_i - d_j}. \tag{3.52}$$

In other words, the heterogeneity of fractal behavior between two brain regions brings about the decrease in correlation of BOLD signals. Even though the correlation of neuronal activities is equal to one, the corresponding BOLD signals may have the lower correlation. In results, Pearson correlation, as the traditional definition of functional connectivity, may not well reflect the correlation of neuronal population activities due to deflection by fractal behavior.

However, the relevance of long memory to functional connectivity may differ in the other long memory models. Now let us consider the fractional Gaussian noise (FGN) model that has been widely used in resting state neuroimaging analyses but whose effects on connectivity distortion has not been well understood so far. As introduced in Section 2.7.2.1, the FGN process can be considered as a special case of the increment process of the fractional Brownian motion (FBM). Let us remind that FBM can be regarded as a causal linear transform of a Wiener process with a self-similarity kernel as shown in Lemma 2. It implies that an FGN process can be viewed as the filtered time series of a Gaussian white noise via the self-similarity kernel, which enables us to use the same framework as illustrated in Figure 4.2(c). Lemma 13 shows that a vector fractional Brownian motion can be viewed as a linear transform of a multivariate time series consisting of correlated Brownian motions with the self-similarity kernel. However, the FGN-based representation of resting state BOLD signals is less flexible than the FI process model since neuronal activity is always assumed to be a Gaussian white

noise process while the FI process model embraces more various types of neuronal activities.

Lemma 13. *Let $\mathbf{x}(t)$ be a vector fractional Brownian motion given in the equation, and $\mathbf{u}(t) = \mathbf{B}_c(t)$ be a correlated Brownian motion with correlation matrix Σ_u. Then, there exist the $p \times p$ matrices $\mathbf{M}_+$ and $\mathbf{M}_-$ such that*

$$
\mathbf{x}(t) = \int_{\mathbb{R}} \left(\left((t - \tau)_+^{\mathbf{H}-1/2} - (-\tau)_+^{\mathbf{H}-1/2} \right) \mathbf{A}'_+ \right.
$$
$$
\left. + \left((t - \tau)_-^{\mathbf{H}-1/2} - (-\tau)_-^{\mathbf{H}-1/2} \right) \mathbf{A}'_- \right) d\mathbf{u}(\tau) \qquad (3.53)
$$

where $\mathbf{H} = \mathrm{diag}\,(H_i)$ for $H_i \in (0,1)$.

Proof. Let $\mathbf{M}$ be a $p \times p$ matrix satisfying $\Sigma_u = \mathbf{M}\mathbf{M}^t$. Then, $\mathbf{u}(t) = \mathbf{M}\mathbf{B}(t)$. In Lemma 2, there exist $\mathbf{A}'_+$ and $\mathbf{A}'_-$ such that $\mathbf{A}_+ = \mathbf{A}'_+\mathbf{M}$ and $\mathbf{A}_- = \mathbf{A}'_-\mathbf{M}$. Hence, (3.53) follows from (2.83). $\qquad \square$

Proposition 14 (Connectivity distortion in FGN). *Let $\mathbf{z}(t) \doteq \{z_i(t); i = 1, \cdots, p\}$ be the increments of a multivariate fractional Brownian motion with Hurst exponents $\mathbf{H} = \mathrm{diag}\,(H_i)$ for $H_i \in (0,1)$ as represented as stochastic integral in (3.53). For the causal case ($A_- = 0$),*

$$
\frac{\gamma_{i,j}^{(x)}}{\gamma_{i,j}^{(u)}} = \begin{cases} \dfrac{B(H_i + 1/2, H_j + 1/2)(\cos(\pi H_i) + \cos(\pi H_j))}{\sin(\pi H_i + \pi H_j)} & \text{if } H_i + H_j \neq 1 \\ \dfrac{1}{2} B(H_i + 1/2, H_j + 1/2)\left(\sin(\pi H_i) + \sin(\pi H_j)\right) & \text{if } H_i + H_j = 1 \end{cases},
$$
$$(3.54)$$

$$
\frac{\rho_{i,j}^{(x)}}{\rho_{i,j}^{(u)}} = \frac{D_{i,j}}{\sqrt{D_{i,i}D_{j,j}}} \qquad (3.55)
$$

where $B(\cdot)$ denotes the beta function and

$$
D_{i,j} = \begin{cases} \dfrac{\cos(\pi H_i) + \cos(\pi H_j)}{\Gamma(H_i + H_j + 1)\sin\left(\pi(H_i + H_j)\right)} & \text{if } H_i + H_j \neq 1 \\ \dfrac{\sin(\pi H_i) + \sin(\pi H_j)}{\Gamma(H_i + H_j + 1)} & \text{if } H_i + H_j = 1 \end{cases}. \qquad (3.56)
$$

Proof. In the case of $H_i + H_j \neq 1$, (2.86) in Lemma 3 can be represented by

$$\gamma_{i,j}^{(x)} = \frac{B(H_i + 1/2, H_j + 1/2)}{\sin(\pi(H_i + H_j))}(A_{ij} + A_{ji}) \tag{3.57}$$

where $\mathbf{A} = (A_{i,j})$ is given by

$$\begin{aligned}\mathbf{A} &= \cos(\pi\mathbf{H})\mathbf{A}_+\mathbf{A}_+^t + \mathbf{A}_-\mathbf{A}_-^t\cos(\pi\mathbf{H}) \\ &\quad - \sin(\pi\mathbf{H})\mathbf{A}_+\mathbf{A}_-^t\cos(\pi\mathbf{H}) - \cos(\pi\mathbf{H})\mathbf{A}_+\mathbf{A}_-^t\sin(\pi\mathbf{H}),\end{aligned} \tag{3.58}$$

and $\cos(\pi\mathbf{H}) = \mathrm{diag}\left(\cos(\pi H_i)\right)$. Assume that $\mathbf{A}_+ = \mathbf{M}$ and $\mathbf{A}_- = \mathbf{0}$. Then,

$$\mathbf{A} = \cos(\pi\mathbf{H})\mathbf{M}\mathbf{M}^t = \cos(\pi\mathbf{H})\Sigma_u. \tag{3.59}$$

where $\Sigma_u = (\gamma_{i,j}^{(u)})$. In the case that $H_i + H_j = 1$, we have from (2.88) in Lemma 3

$$\gamma_{i,j}^{(x)} = \frac{1}{2}B(H_i + 1/2, H_j + 1/2)\left(\sin(\pi H_i) + \sin(\pi H_j)\right)A_{i,j}^{(0)}, \tag{3.60}$$

where

$$\mathbf{A}^{(0)} = \mathbf{A}_+\mathbf{A}_+^t = \mathbf{M}\mathbf{M}^t = \Sigma_u. \tag{3.61}$$

Hence, (3.54) follows from (3.57) and (3.60). Likewise, (3.55) follows from (3.54) and $B(a,b) = \Gamma(a)\Gamma(b)/\Gamma(a+b)$. $\qquad\square$

Proposition 14 states that the correlation of BOLD signals between two brain regions may be distorted depending on the difference of Hurst exponents. However, the pattern of connectivity distortion in the FGN model is quite different from that of the FI process. Figure 3.12 illustrates the comparison of connectivity distortion between FGN and FI process models. It is common, in both FGN and FI process, that the discrepancy between correlation of BOLD signals and correlation of neuronal activities deteriorates as the difference of memory parameters increases. This pattern is called the fractal-driven *connectivity distortion*. When $1/2 < H_i, H_j < 1$, the FGN has similar pattern of connectivity distortion over the bivariate distribution of Hurst exponents with the FI process. In other words, the fractal behavior based on the FGN model has similar effects on functional connectivity with the FI process model in the long memory area
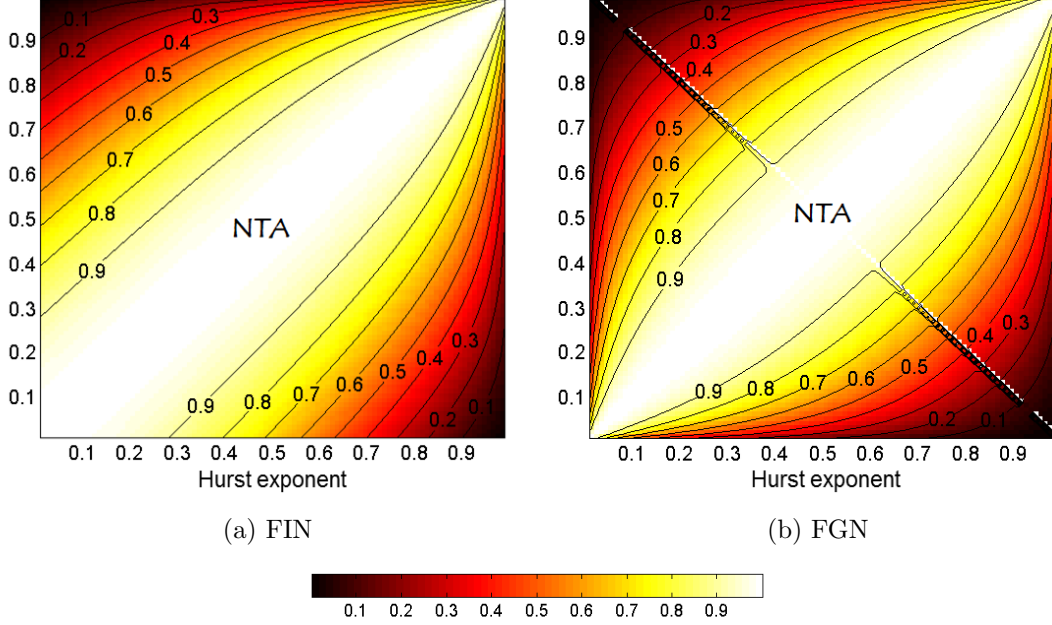
Figure 3.12: The ratio of long memory correlation to short memory correlation in both fractionally integrated noise (FIN) and fractional Gaussian noise (FGN).

$(1/2 < H_i, H_j < 1)$. On the other hand, the connectivity distortion in the FI processes is more alleviated than in the FGN model for other cases of memory distribution -especially when $0 < H_i, H_j < 1/2$. It means that, in the short memory area $(0 < H_i, H_j < 1/2)$, the functional connectivity based on the FI process model is less sensitive to heterogeneous fractal behavior than that based on the FGN model. The area of Hurst exponents such that $\rho_{i,j}^{(x)}/\rho_{i,j}^{(u)} > 0.9$ is called the *nonfractal transmission area* (NTA). In Figure 3.12, the size of NTA for the FIN processes is more spacious and asymmetric while the NTA is symmetric in the FGN processes.

3.5.2 Simulation studies

In Section 3.5.1, the relevance of long memory to functional connectivity has been theoretically inferred on the basis of the multivariate FI process model. The theories expect that the difference of memory parameters causes the discrepancy

between correlation of BOLD signals and correlation of neuronal activities. On the other hand, the theories do not provide any inference about the influence of long memory on the brain network obtained by thresholding the correlation matrix (see Section 2.4 for details on graph-theoretical analysis). The complexity of the brain network makes it difficult to explain the impacts of long memory on global network dynamics. Here an inductive method based on simulation studies is suggested to figure out the association between long memory and network properties.

The whole procedure of the simulation studies are summarized in Figure 3.14. First, the structural network based on anatomical connections of the macaque brain was adopted from Honey et al. (2007); the network consists of 47 regions with 505 connections (see Figure 3.13). Then, the spontaneous neuronal population activities were simulated based on the neural field model (see Section 2.2 for the related theories, and see Figure 3.14(a)). Each brain region was set to consist of 8 neurons, and each neuron was forced to burst random spikes independently. The mutual population activity among regions is nonlinearly self-organized through network connections. From the simulated neuronal population activities, the corresponding BOLD signals with long memory are generated by convolving them with the cs-HRF filter $r(t)$ in (3.15) (see Figure 3.14(a)). The memory parameters of the cs-HRF filters were randomly assigned with the Gaussian distribution.

Afterwards, functional connectivity and information flow were computed from both the neuronal population activities and the BOLD signals (see Figure 3.14(b)). Functional connectivity was defined based on Pearson correlation (PC) while information flow was measured based on either mutual information (MI) or transfer entropy (TE) (see Section 2.3). Both PC and MI are undirectional measures while TE is related to directional information flow. Especially, it is known that TE is more appropriate to specify the directional information flow in a coupled system such as neuronal population (Kaiser & Schreiber, 2002). Finally, three types of network were obtained: PC, MI, and TE networks.

One of network properties useful for the topological diagnosis is the node centrality. In this study, the *weighted betweenness centrality* (abbreviated to centrality in this section), quantifying the fraction of all shortest paths passing

Figure 3.13: The structural connectivity of macaque neocortex. Reproduced from Honey et al. (2007) with permission.

through the given node, was computed from the given connectivity matrices by using the brain connectivity toolbox (BCT) (Brandes, 2001; Rubinov & Sporns, 2010). Any brain region (or node in graph terminology) with high centrality can be regarded as a hub region connecting different communities of nodes.

Figure 3.15 illustrates how the centrality is affected by fractal behavior. The first (Case A) and second columns (Case B) in the figure correspond to the scenarios such that memory parameters of cs-HRF filter are Gaussian distributed with standard deviation 0.1 and 0.3 respectively. Therefore, The heterogeneity of fractal behavior among brain regions is greater in Case B than in Case A. In the PC network, there was a weak discrepancy in centrality between neuronal activities and BOLD signals as the regression slopes were $r^2 = 0.85$ and $r^2 = 0.72$ for Case A and Case B (see Figures 3.15(a) and 3.15(b)). Although the discrepancy grows worse as the heterogeneity of fractal behavior increases, the centrality in BOLD signals is acceptably correlated with that in neuronal activities. However the correlation of centrality between neuronal activities and BOLD signals becomes weaker in the MI network as the corresponding regression slopes were $r^2 = 0.53$ and $r^2 = 0.6$ for Case A and Case B (see Figures 3.15(c) and 3.15(d)). However, unlike the PC network, the correlation is enhanced as the brain regions exhibit more heterogeneous fractal behaviors. The TE network is excessively sensitive to fractal behaviors as $r^2 = 0.46$ and $r^2 = -0.04$ for Case
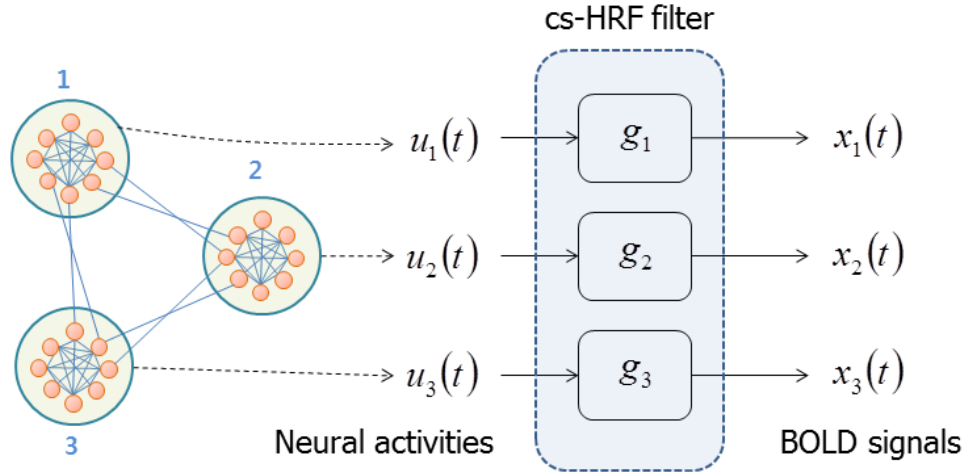
(a)
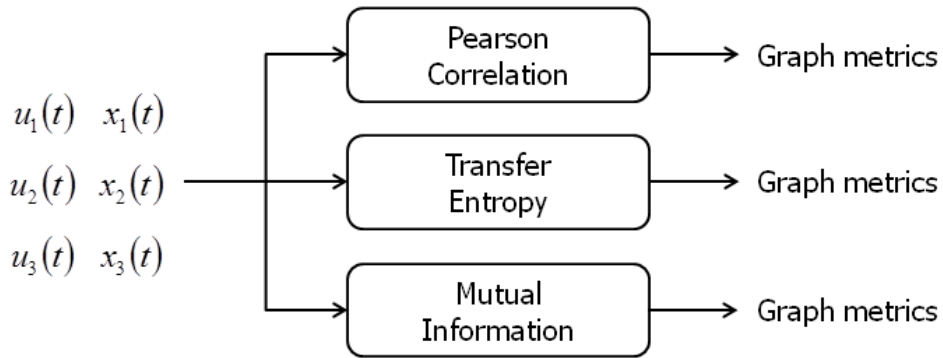
(b)

Figure 3.14: Simulation process of resting state BOLD signals.

A and Case B (see Figures 3.15(e) and 3.15(f)). The correlation of centrality between neuronal activities and BOLD signals is seriously destroyed by heterogeneous fractal behaviors in the TE network. All of these results suggest not only that the information flow such as MI and TE is more sensitively perturbed by fractal behaviors than functional connectivity, but also that the fractal-driven perturbation is more serious in directional information flow than in undirectional measures.

Unlike the PC, MI, and TE networks, the wavelet correlation (WC) enables

us to observe the scale-dependent correlation over several frequency bands (see Section 2.5 for the related theories). Figure 3.16 shows the impacts of fractal behavior on the WC network over scales (where high scale corresponds to low frequencies). In a node with low centrality in the structural network, the mean relative difference in wavelet correlation between neuronal activities and BOLD signals was greater in low frequencies while such a significant difference was alleviated in a node with high centrality (see Figures 3.16(a) and 3.16(b)). In addition, the degree of relative deviation in low frequency wavelet correlations was dependent on the heterogeneity of fractal behaviors as well as the node centrality. The discrepancy of node centrality in the WC network between neuronal activities and BOLD signals was also prominent in low frequency scales for a node with small centrality in the structural network (see Figures 3.16(c) and 3.16(d)). The degree of discrepancy was reduced as the heterogeneity of fractal behaviors increases. However, the reduced discrepancy should not be attributed to the heterogeneity of fractal behaviors since it might be caused by the reduction of wavelet correlations as shown in Figures 3.16(a) and 3.16(b). Consequently, these results overall indicate that both the wavelet correlations and their node centralities corresponding to low frequencies are more affected by heterogeneous fractal behaviors in a node with small centrality in the structural network.

3.6 Summary and Discussion

It has been supposed, based on empirical observations, that the main source of long memory in resting state BOLD signals is cerebral hemodynamic activities. However, simulation studies suggest that the conventional hemodynamic models such as HRF and Balloon model do not well predict long memory in resting state BOLD signals.

In this chapter, a novel long memory model of hemodynamic response has been suggested to effectively describe long memory in resting state BOLD signals in terms of hemodynamic response function (HRF). The long memory may be caused when the coefficients of several basis functions comprising the HRF are arranged with slowly-decaying pattern. This theoretical inference can be an indirect evidence that the fractal behavior is associated with physical mechanism of

hemodynamic activities. The proposed model also implies that the FI process is more appropriate model for resting state BOLD signals with long memory than the FGN process. This linear long memory model of hemodynamic response can be extended to the nonlinear case based on the Volterra series expansion. Theories suggest that the long memory phenomenon is not almost influenced by nonlinearity of the hemodynamic system. Note that the nonlinearity of hemodynamics may have an effect on functional connectivity, and thus would increase the difference of statistical properties between neuronal activities and BOLD signals.

This hemodynamic response model has an important implication such that the HRF is not static over time and may be subject to the current and past states of neuronal activity. The dependence of hemodynamic response on the history of neuronal activities was named the history dependent excitability (HDE). The physical and biological mechanism that links the dynamic change of HRF with the history of neuronal activities has been unrevealed. Nevertheless, it can be concluded that the hemodynamic activity is in the critical state generating its fractal behavior when input neuronal activity satisfies the short memory condition and the corresponding BOLD signal has long memory.

Finally, the relation of long memory with functional connectivity has been revealed through theoretical inferences and simulation studies. In the case that a resting state BOLD signal is modeled as an FI process, there exists a difference between correlation of neuronal activity and correlation of BOLD signals, and the gap becomes wider as the heterogeneity of fractal behaviors increases. The different fractal behaviors between two brain regions result in the distortion of functional connectivity. Such a connectivity distortion is inevitable even in the FGN process model, but the distortion pattern is determined depending on what type of long memory model is applied. Moreover, simulation studies indicate not only that the long memory driven by hemodynamic activities gives rise to the change in network properties especially in directional information flow such as transfer entropy, but also that connectivity distortion is more serious in low frequencies at a region with small centrality of the structural network.
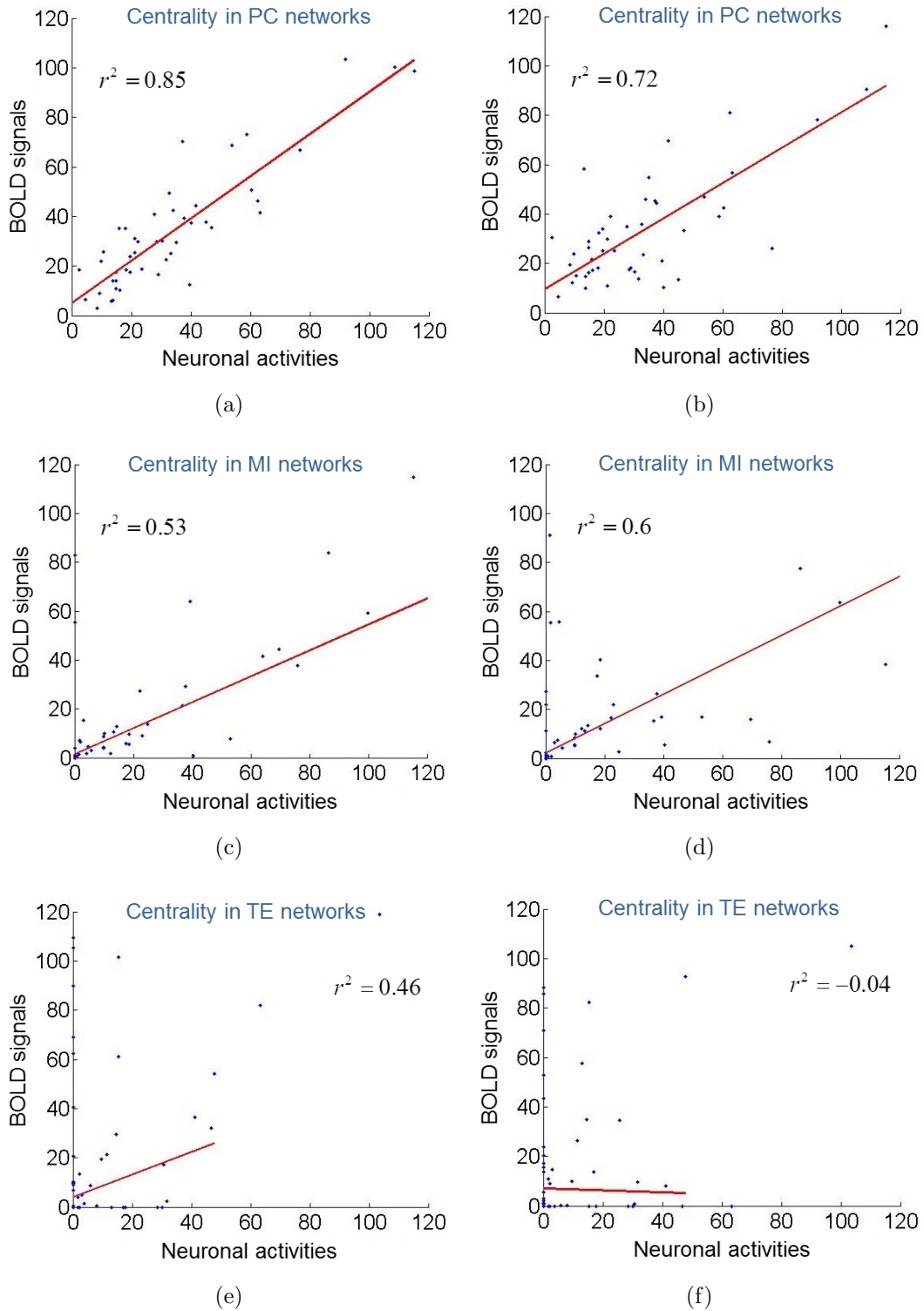
Figure 3.15: Scatter plots which illustrate the differences of centrality in three types of functional networks -such as Pearson correlation (PC), transfer entropy (TE), and mutual information (MI)- between neuronal activities and BOLD signals. Left and right correspond to the cases when the standard deviation of fractal exponents is 0.1 and 0.3 respectively.

(a)

(b)

(c)

(d)

Figure 3.16: The spectrum of connectivity distortion based on wavelet correlation across frequency scales. (a-b) The Euclidean distance of wavelet correlations over scales (where high scale corresponds to low frequencies) between neuronal activities and BOLD signals. (c-d) The Euclidean distance of centrality over scales. Left and right correspond to $SD(d) = 0.1$ and 0.3 respectively.

Chapter 4

Fractal-based analyses

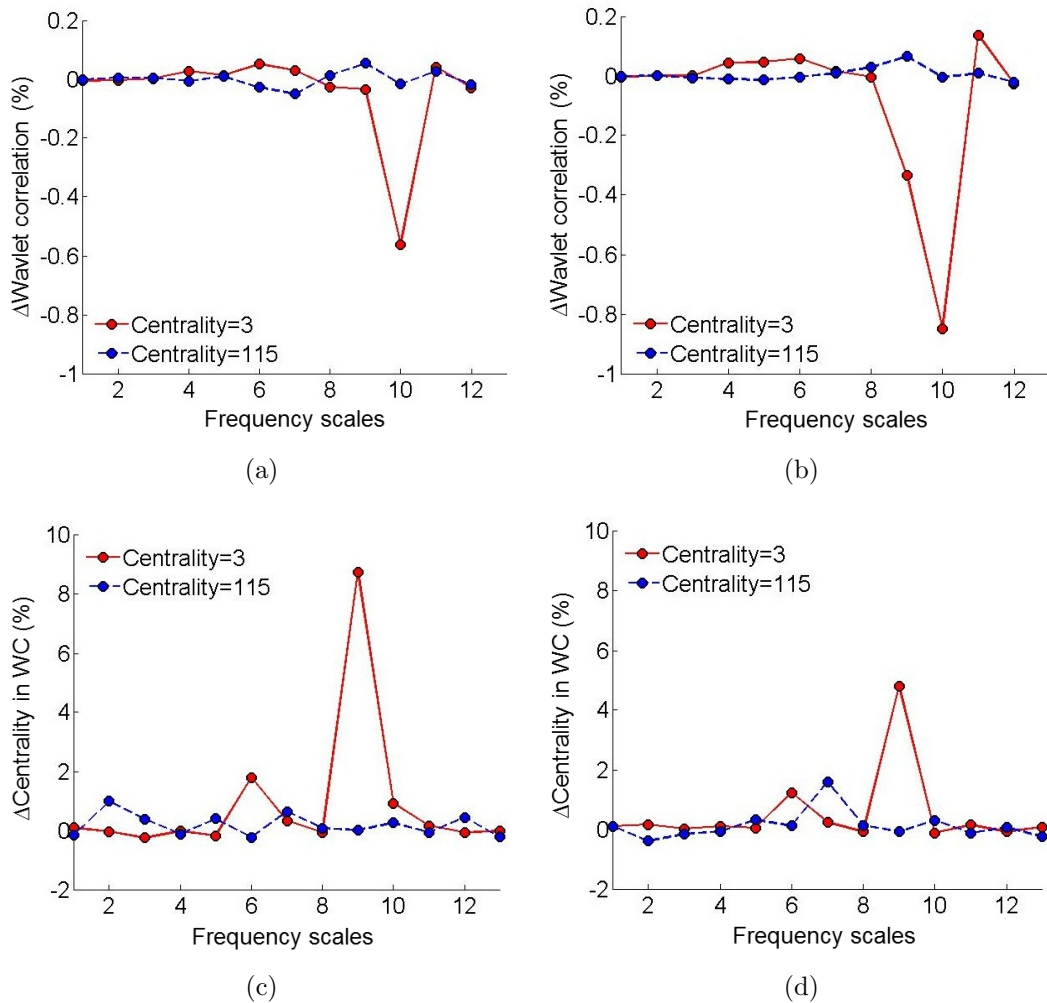## 4.1 Introduction

In the previous chapter the association between long memory and functional connectivity in resting state BOLD signals was theoretically inferred on the basis of the proposed long memory model of hemodynamic response (see Section 3.5). The heterogeneity of hemodynamic fractal behaviors between brain regions incurs the discrepancy between functional connectivity of neuronal activities and that of the corresponding BOLD signals. The fractal-driven distortion of resting state functional connectivity is depicted in Figure 4.1(b). The long memory may also lead us to wrong observations on network properties of BOLD signals in low frequencies. The connectivity distortion is commonly expected regardless of which statistical model of long memory is applied. This fact indicates that Pearson correlation, widely used as a definition of functional connectivity, may not well reflect functional interactions among spontaneous neuronal populations implicit in BOLD signals especially when the brain regions exhibit heterogeneous fractal behaviors.

The stimulation to the brain facilitates the analysis of functional connectivity by reducing the gap of connectivity between neuronal activities and BOLD signals. The change in the BOLD signal is supposed to reflect the change in synaptic activity activated by stimulation (Fox & Raichle, 2007; see Figure 4.1(a)). It implies that the hemodynamics has little impacts on functional connectivity in

(a) Evoked state
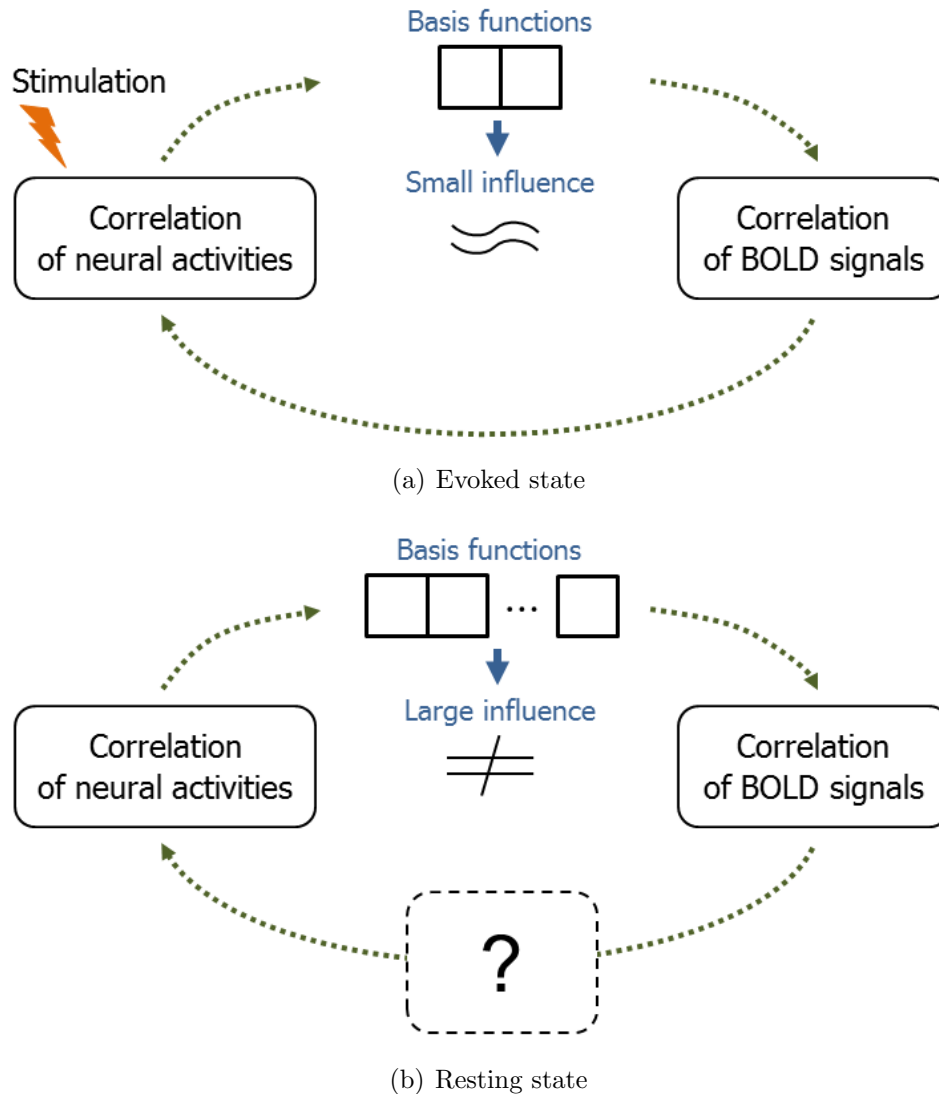
(b) Resting state

Figure 4.1: The comparison between evoked state connectivity and resting state connectivity. (a) Evoked state connectivity well reflects functional connectivity of neuronal activities while (b) resting state connectivity tends to be highly affected by the hemodynamic kernel consisting of lots of basis functions.

evoked state (Honey et al., 2007). Notice that the difference of hemodynamic condition between evoked state and resting state is associated with the number of basis functions as well as the arrangement of these coefficients. The impulse hemodynamic response in resting state is composed of a large number of basis functions whose coefficients are slowly decaying according to the quasi long

memory condition of Theorem 7 while the evoked state hemodynamic response function is approximated as a combination of just two basis functions (see Figure 4.1). These hemodynamic properties increase the complexity of resting state hemodynamics, and promote the connectivity distortion as the heterogeneity of fractal behaviors between brain regions increases. As a result, the resting state hemodynamics characterized by long memory acts as an artifact which disturbs estimating the functional dynamics of neuronal activities from resting state BOLD signals.

In this chapter new methods for resting state functional connectivity analyses are proposed to suppress the distortion of functional connectivity caused by fractal behavior. The basic idea underlying these methods is to split a resting state BOLD signal into long memory and short memory components by approximating the signal as a fractionally integrated (FI) process in low frequencies. The long memory model of hemodynamic response proposed in Chapter 3 indicates that a resting state BOLD signal can be approximated as the output of a long memory (LM) filter whose nonfractal input is a neuronal activity; in other words, a resting state BOLD signal $x(t)$ is assumed to be $x(t) \approx x^{(L)}(t) \doteq r(t; d) * u(t)$ from (3.17) where $r(t; d)$ denotes a hemodynamic LM filter with memory parameter d defined in (3.15) and $u(t)$ is a neuronal activity. A neuronal activity is linearly transformed into a long memory process through long memory filtering as depicted in Figure 4.2(a). This FI process model enables us to correct the connectivity distortion caused by hemodynamic fractal behavior by estimating the cross-correlation of neuronal activities $\mathbf{u}(t)$ as well as memory parameters.

In practice, both the nonfractal input and the LM filter do not exactly represent neuronal activity and hemodynamics respectively. A resting state BOLD signal may be also interrupted by physiological processes (such as cardiac motion and breathing) and instrumental noise as well as hemodynamic activity. Hence, the LM filter may be a sequence of filters associated with several factors (see Figure 4.2(b)). Moreover, neuronal activity may exhibit long memory properties (Lowen & Teich, 1991, 2005; see Section 2.2). In general, all physical sources influencing the BOLD contrast consist of short memory as well as long memory components; for example, it was inferred in Proposition 9 that the hemodynamic filter can be split into long memory and short memory elements. The complexity

80

(a) Linear BOLD model

(b) Practical BOLD model

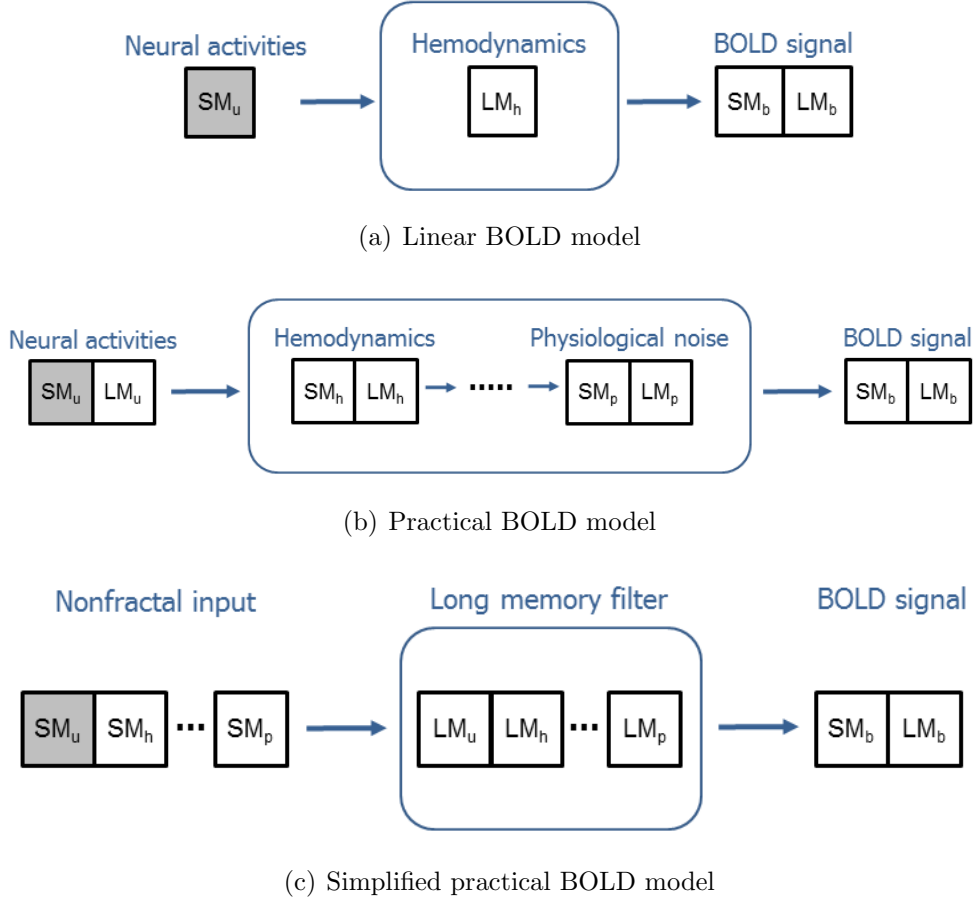

(c) Simplified practical BOLD model

Figure 4.2: The generalized long memory model of resting state BOLD signals. (a) The long memory model of hemodynamic response, (b) the extended long memory model of resting state BOLD signals, and (c) its simplified representation. Each process or filter consists of short memory (SM) and long memory (LM) components.

of physical mechanism underlying the long memory phenomenon makes it difficult to estimate the endogenous functional dynamics among neuronal populations from resting state BOLD signals.

In spite of these intricately entangled factors, the practical model can be simplified by combining all long memory components as an unified LM filter as shown in Figure 4.2(c). In this case, the combination of short memory components is called the *nonfractal signal* (equivalently called the short memory process). Therefore, a resting state BOLD signal can be represented as the linear convolution of an unified nonfractal signal with the unified LM filter as given as

follows

$$x(t) = \overbrace{\left[r(t; d_r) * p_L(t; d_p) * e_L(t; d_e) * u_L(t; d_u) * \cdots \right]}^{\text{LM filters } L(t)}$$
$$* \underbrace{\left[\beta(t) * p_S(t) * e_S(t) * e_s(t) * u_S(t) * \cdots \right]}_{\text{Short memory } S(t)}$$
$$= L(t) * S(t) \tag{4.1}$$

where r and β is given in (3.28), p_L, e_L, u_L denote the LM filters modulated by physiological noise, equipment, and neuronal processes respectively while p_S, e_S, u_S denote short memory components in these factors. $L(t)$ and $S(t)$ denotes the unified LM filter and the unified nonfractal signal respectively. The equation (4.1) indicates that a resting state BOLD signal with long memory can be split into two independent components: a long memory filter and a short memory process.

The assumption that a resting state BOLD signal can be split into long memory and short memory leads us to take the correlation of nonfractal signals into account as a novel concept of resting state functional connectivity. This particular correlation independent of fractal behavior is called the *nonfractal connectivity*. Its mathematical definition is described in Section 4.2.1. The notion of nonfractal connectivity is comparable to *fractal connectivity* which was first proposed in Achard et al. (2008) as the asymptotic value of wavelet correlations over low frequency scales. The wavelet correlations of two long memory processes converge on a particular value which is determined by memory parameters as well as short memory components. The theoretical relevance of nonfractal connectivity to fractal connectivity is described in Section 4.2.2.

Note that the nonfractal signal $S(t)$ in (4.1) is not exactly identical to neuronal activity $u_S(t)$ because of influences from other factors. Likewise, the aggregated LM filter $L(t)$ represents not just an HRF filter but the combined long memory effects of all possible sources. Strictly speaking, both the LM filter $L(t)$ and the nonfractal signal $S(t)$ are abstract concepts that do not exist physically while the long memory model of resting state BOLD signals has been deductively proposed in Section 3.2 on the basis of the hypotheses on physical properties of hemodynamic response and spontaneous neuronal activities. In these reasons, nonfractal

connectivity does not directly reflect actual correlation of neuronal activities. Nevertheless, the nonfractal connectivity may give us better information on functional dynamics of spontaneous neuronal activities than the ordinary correlation of BOLD signals since the it is independent from fractal behavior of cerebral hemodynamics. In other words, the fractal-driven connectivity distortion can be corrected by eliminating the effect of long memory components $L(t)$.

The nonfractal connectivity can be effectively estimated by modeling a resting state BOLD signal as an FI process (see Figure 4.3). According to the simplified practical model, the effects of all factors on long memory can be easily summarized in the spectral domain. Let us assume that a resting state BOLD signal can be well approximated as an FI process. Then, the spectral density of $x(t)$ is obtained as follows

$$f'(\lambda) = \left|1 - e^{-i\lambda}\right|^{-2(d_r + d_p + d_e + d_u + \cdots)} f_S(\lambda) \tag{4.2}$$

where $f_S(\lambda)$ is the multiplication of short memory spectral densities from all factors; $f_S(\lambda) \doteq f_\beta(\lambda) f_p(\lambda) f_e(\lambda) f_u(\lambda)$. In (4.2), the joint contributions of lots of factors to long memory are simply represented as a sum of memory parameters in the spectral density. Therefore, although the remaining short memory component is still corrupted by other noise factors, the unified effect of long memory on connectivity distortion can be effectively compensated by estimating the summation of memory parameters using one of the conventional estimators.

Notice that the fractional Gaussian noise (FGN) model could be adopted as a long memory model of the resting state BOLD signal. However, this model is not appropriate for complicated dynamic systems such as the brain because its basic assumption is that the short memory input is just a white noise process; indeed, neuronal activities are not just white noises but should be described by more general time series model. On the other hand, the FI process model allows a diversity of nonfractal signals as an input as discussed in Section 2.7.2.2. For instance, the FI process becomes an ARFIMA process in the case that the short memory process is given as an autoregressive (AR) process. Moreover, the model is fit for the long memory model of hemodynamic response proposed in Chapter 3. In these reasons, the FI process model is used in this chapter to develop the techniques for fractal-based connectivity analysis.
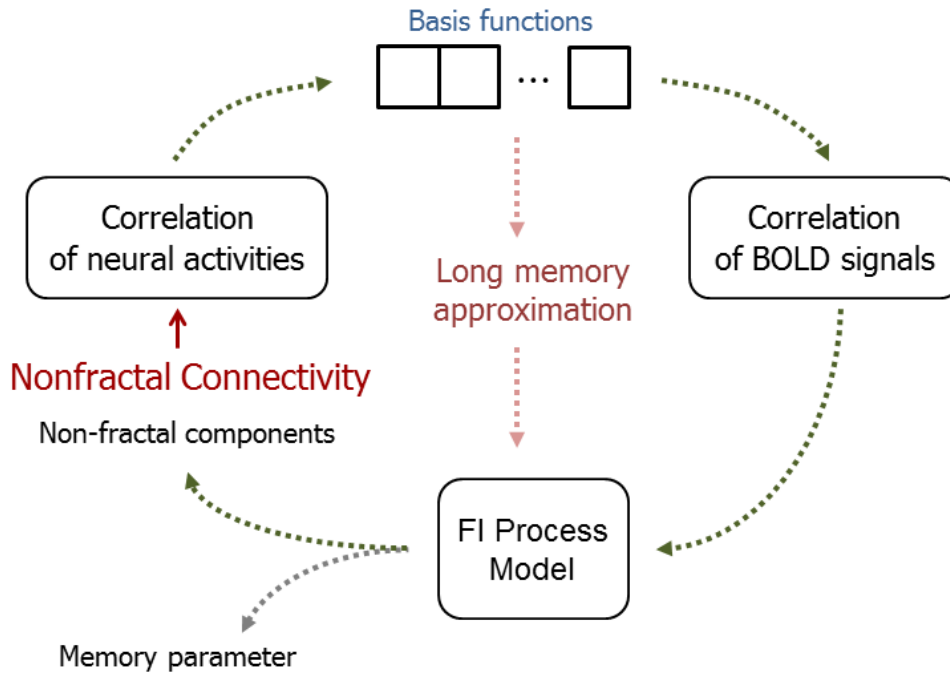
Figure 4.3: The physical implication of nonfractal connectivity.

This chapter is organized as follows. In Section 4.2, the nonfractal connectivity and fractal connectivity are theoretically defined, and their relationship is described. Then, several wavelet-based methods for estimating both nonfractal connectivity and fractal connectivity along with memory parameters are proposed in Section 4.3. The performance of these estimators for fractal-based connectivity was evaluated through simulation studies.

4.2 Fractal-based connectivities

It was stated in the previous section that a resting state BOLD signal with long memory can be separated into long memory and short memory components on the basis of the multivariate FI process model. In this section, nonfractal connectivity and fractal connectivity are defined from this theoretical expectation as novel measures of resting state functional connectivity. While fractal connectivity is based on the asymptotic behavior of wavelet correlations, nonfractal connectivity is associated with the covariance of short memory.

4.2.1 Nonfractal connectivity

Let $\mathbf{x}(t)$ be a vector FI process with memory parameter $\mathbf{d}$. Then, the process can be represented as follows in terms of fractional difference as defined in Section 2.7.2.2

$$\mathbf{D}\mathbf{x}(t) = \mathbf{u}(t) \tag{4.3}$$

where $\mathbf{D} = \text{diag}\left[(1-\mathcal{B})^{d_i}\right]$ denotes a fractional difference operator matrix and $\mathbf{u}(t) = [u_i(t)]$ is a multivariate nonfractal signal which consists of weakly stationary short memory processes. The *nonfractal connectivity* of two FI processes $x_m(t)$ and $x_n(t)$ is defined as

$$\xi_{m,n} = \frac{\gamma_{m,n}^{(u)}}{\sqrt{\gamma_{m,m}^{(u)}\gamma_{n,n}^{(u)}}} \tag{4.4}$$

where $\gamma_{m,n}^{(u)} = \mathbb{E}\left[u_m(1)u_n(1)\right]$ denotes the covariance of $u_m(t)$ and $u_n(t)$. Therefore, the nonfractal connectivity is equal to the correlation coefficient $\rho_{m,n}^{(u)} = \text{cor}\left[u_m(1)u_n(1)\right]$. As mentioned in Section 4.1, the nonfractal connectivity does not directly represent the correlation of neuronal activities but that of nonfractal components split from resting state BOLD signals.

4.2.2 Fractal connectivity

The notion of fractal connectivity was first suggested by Achard et al. (2008), and motivated from a study on wavelet correlation of a multivariate long memory process. Theorem 15 states the scale-invariance of wavelet correlation in long memory processes over low frequencies.

Theorem 15 (Asymptotic wavelet correlation). *Let $\mathbf{u}(t) \doteq \{u_i(t); i = 1, \cdots, p\}$ be a vector Gaussian white noise process with correlation matrix $\Sigma^{(u)} = \left(\gamma_{m,n}^{(u)}\right)$, and $\mathbf{x}^{(L)}(t) \doteq \left\{x_i^{(L)}(t); i = 1, \cdots, p\right\}$ be a vector weakly stationary process such that $x_i^{(L)}(t) = r(t; d_i) * u_i(t)$ where $r(t; d_i)$ is given in (3.15) with memory parameter $|d_i| < 1/2$. Let $W_j^{(m)}(t)$ and $W_j^{(n)}(t)$ be the jth level wavelet coefficients for $x_m^{(L)}(t)$ and $x_n^{(L)}(t)$ respectively based on an wavelet filter $\{h(l)\}$ with transfer function $H(\lambda)$. Suppose that the squared gain function of $h_j(l)$ defined in (2.46)*

is approximated by

$$\mathcal{H}_j(\lambda) \approx \begin{cases} 2^j & \text{if } 1/2^{j+1} \leq |\lambda| \leq 1/2^j, \\ 0 & \text{otherwise.} \end{cases} \tag{4.5}$$

Then, the jth level wavelet covariance $\nu_{m,n}(j) \doteq \text{cov}\left\{W_j^{(m)}(t), W_j^{(n)}(t)\right\}$ *and the jth level wavelet correlation* $\rho_{m,n}^{(x)}(j) \doteq \text{cor}\left\{W_j^{(m)}(t), W_j^{(n)}(t)\right\}$ *can be approximated as* $j \to \infty$ *by*

$$\nu_{m,n}^{(x)}(j) \approx \gamma_{m,n}^{(u)} B_1(d_m, d_n) \cos\left(\frac{\pi}{2}(d_m - d_n)\right) 2^{j(d_m + d_n)}, \tag{4.6}$$

$$\varrho_{m,n} \doteq \rho_{m,n}^{(x)}(\infty) \approx \rho_{m,n}^{(u)} \frac{B_1(d_m, d_n)}{\sqrt{B_1(d_m, d_m) B_1(d_n, d_n)}} \cos\left(\frac{\pi}{2}(d_m - d_n)\right) \tag{4.7}$$

where
$$B_k(d_m, d_n) = \frac{2(1 - 2^{d_m + d_n - k})}{k - d_m - d_n}. \tag{4.8}$$

Proof. Since $\Im\left[f'_{m,n}(\lambda)\right] = -\Im\left[f'_{m,n}(-\lambda)\right]$, we obtain from Corollary 1 and (4.5)

$$\nu_{m,n}(j) = 2 \int_{1/2^{j+1}}^{1/2^j} \mathcal{H}_j(\lambda) f'_{m,n}(\lambda) \mathrm{d}\lambda$$

$$\approx 2^{j+1} \int_{1/2^{j+1}}^{1/2^j} f'_{m,n}(\lambda) \mathrm{d}\lambda = 2^{j+1} \int_{1/2^{j+1}}^{1/2^j} \Re\left[f'_{m,n}(\lambda)\right] \mathrm{d}\lambda. \tag{4.9}$$

Let $\Sigma_d \doteq d_m + d_n$ and $\Delta_d \doteq (d_m - d_n)/2$. Based on the assumption on $\mathbf{u}(t)$, $f_{i,j}(\lambda) = \gamma_{i,j}^{(u)}$ for $|\lambda| \leq 1/2$, we have the same approximation as (3.50) through the Taylor expansions

$$\Re\left[f'_{m,n}(\lambda)\right] \approx \gamma_{i,j}^{(u)} \Bigg(\cos(\Delta_d \pi) \lambda^{-\Sigma_d} + \Delta_d \sin(\Delta_d \pi) \lambda^{1-\Sigma_d}$$

$$+ \frac{\Sigma_d}{24} \cos(\Delta_d \pi) \lambda^{2-\Sigma_d} + \frac{\Sigma_d}{6} \Delta_d \sin(\Delta_d \pi) \lambda^{3-\Sigma_d} \Bigg). \tag{4.10}$$

Hence, we have the following approximation of $\nu_{m,n}(j)$ from (4.9) and (4.10)

$$\nu_{m,n}(j) \approx \gamma_{i,j}^{(u)} 2^{j\Sigma_d} \left[\cos(\Delta_d\pi)B_1 + \Delta_d \sin(\Delta_d\pi)B_2 \frac{1}{2^j} \right.$$
$$\left. + \frac{\Sigma_d}{24}\cos(\Delta_d\pi)B_3\frac{1}{2^{2j}} + \frac{\Sigma_d}{6}\Delta_d \sin(\Delta_d\pi)B_4\frac{1}{2^{3j}} \right]. \qquad (4.11)$$

Then, (4.6) follows from (4.11). If the first-order term in (4.11) is taken, (4.7) follows from $\varrho_{m,n}^{(x)} = \nu_{m,n}^{(x)}/(\nu_{m,m}^{(x)}\nu_{n,n}^{(x)})^{1/2}$. $\qquad\square$

The asymptotic wavelet correlation $\varrho_{m,n}$ is called the *fractal connectivity* of $x_m^{(L)}(t)$ and $x_n^{(L)}(t)$. Similar with nonfractal connectivity, the fractal connectivity is dependent on the difference of memory parameters. Notice that the nonfractal signal $u_i(t)$ in Theorem 15 is assumed to be a white noise process. The scale-invariance of wavelet correlation in low frequencies was also proved by Achard et al. (2008) based on the Taylor series expansion for more general case of nonfractal signals, however the difference between long memory correlation and short memory correlation has not been studied.

Theorem 15 can be interpreted in terms of how the fractal behavior has an impact on functional connectivity. The ratio of fractal connectivity to nonfractal connectivity is given from (4.7) in Theorem 15 by

$$\frac{\varrho_{m,n}}{\xi_{m,n}} \approx \frac{B_1(d_m, d_n)}{\sqrt{B_1(d_m, d_m)B_1(d_n, d_n)}} \cos\left(\frac{\pi}{2}(d_m - d_n)\right). \qquad (4.12)$$

Likewise, the ratio of functional connectivity to fractal connectivity is given from (4.12) and (3.47) in Theorem 12 as follows

$$\frac{\rho_{m,n}^{(x)}}{\varrho_{m,n}} \approx \frac{\sqrt{\left(1 - 2^{2d_m-1}\right)\left(1 - 2^{2d_n-1}\right)}}{1 - 2^{d_m+d_n-1}} \doteq \vartheta\left(d_m, d_n\right). \qquad (4.13)$$

It has an important implication on the upper bound of Pearson correlation $\rho_{m,n}^{(x)}$ given by

$$\rho_{m,n}^{(x)} < \vartheta\left(d_m, d_n\right) < 1. \qquad (4.14)$$

In other words, the heterogeneity of fractal behaviors leads to the reduction of correlation between two BOLD signals. The ratios $\varrho_{m,n}/\xi_{m,n}$ and $\rho_{m,n}^{(x)}/\varrho_{m,n}$ are

(a) $\varrho_{m,n}/\xi_{m,n}$
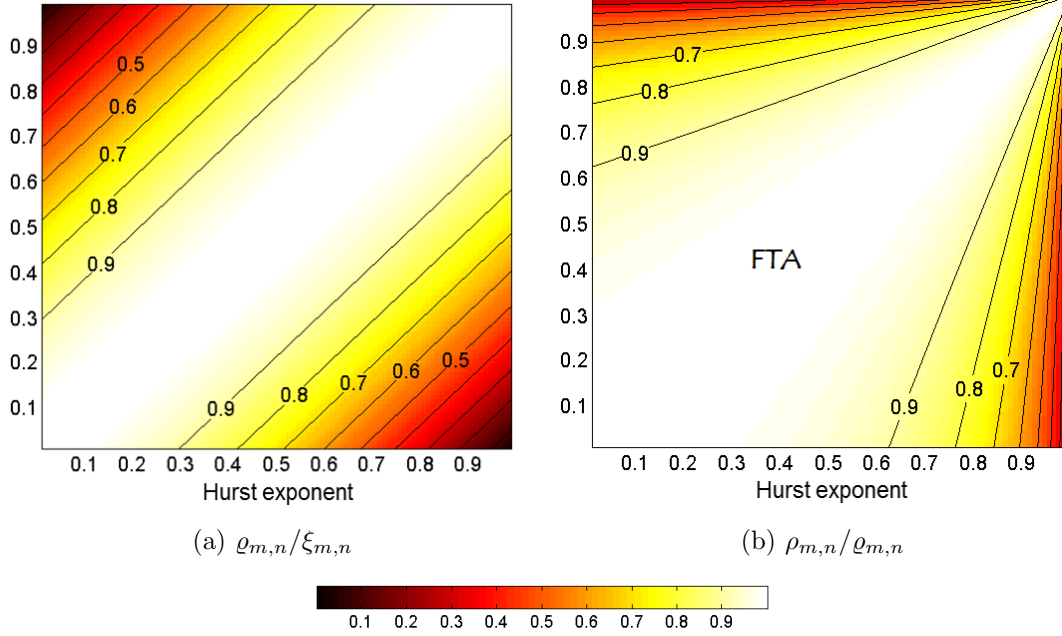
(b) $\rho_{m,n}/\varrho_{m,n}$

Figure 4.4: The comparison of fractal connectivity with nonfractal connectivity and Pearson correlation: (a) the ratio of fractal connectivity to nonfractal connectivity over Hurst exponents, and (b) the ratio of Pearson correlation to fractal connectivity.

depicted in Figure 4.4. When the memory parameters are similar, the fractal connectivity $\varrho_{m,n}$ makes little difference with the nonfractal connectivity $\xi_{m,n}$ and the Pearson correlation $\rho_{m,n}^{(x)}$. As the heterogeneity of memory parameters increases, the difference between fractal connectivity and nonfractal connectivity becomes also larger. However, the difference of fractal connectivity with Pearson correlation is negligible when two time series have memory parameters less than $1/2$. Moreover, the difference between fractal connectivity and Pearson correlation is not significant even in the long memory area where $H_m > 1/2$ and $H_n > 1/2$. The area of Hurst exponents such that $\rho_{i,j}/\varrho_{m,n} > 0.9$ is called the *fractal transmission area* (FTA). When two resting state BOLD signals have fractal behaviors inside the FTA, it can be interpreted as that their correlation is similar with the correlation of nonfractal components. FTA in Figure 4.4 is broader than NTA in Figure 3.12, which implies that nonfractal connectivity has larger difference with Pearson correlation than fractal connectivity has.

4.3 Wavelet-based estimation

In this section a diversity of wavelet-based methods for estimating both nonfractal connectivity and fractal connectivity from resting state BOLD signals are proposed. The wavelet transform can act as a natural tool to analyze long memory processes (Bullmore et al., 2004; Percival & Walden, 2006; Wornell, 1993; Wornell & Oppenheim, 1992). Especially, the transform is indispensable to estimate fractal connectivity which is based on the asymptotic property of wavelet correlation. The other benefit of wavelets is that it splits a time series over several scales (where large scales correspond to low frequencies). It enables us to skip some scales which are liable to be seriously corrupted by additive noises. For instance, the nonfractal connectivity might be directly computed from (3.47) if the covariance of resting state BOLD signals is known *a priori*. However, in the case that the BOLD signal is perturbed by a white noise, the nonfractal connectivity is greatly influenced by the noise since it changes the value of correlation coefficients $\hat{\rho}_{i,j}^{(x)}$ as well as the estimate of memory parameters $\hat{d}_i$. Therefore, it is instrumental to consider wavelet coefficients just in low frequencies by eliminating wavelet scales corresponding to high frequencies relatively sensitive to additive noise.

The wavelet-based estimation of nonfractal connectivity and fractal connectivity is based on Theorem 15 on wavelet covariance and wavelet correlation in (4.6) and (4.7). Notice that one basic assumption in the theorem is that the short memory components of resting state BOLD signals are given as Gaussian white noise processes. In reality, the short memory is not always represented as such a white noise. To overcome this limitation, let us assume that a multivariate resting state BOLD signal $\mathbf{x}(t)$ can be modeled as a vector FI process with memory parameter $\mathbf{d}$ whose dth order difference process $u(t) = (1 - \mathcal{B})^d x(t)$ is a short memory process and its spectral density satisfies

$$f_u(\lambda) \sim \mathbf{Q}, \ \ \lambda \to 0 \tag{4.15}$$

where $\mathbf{Q}$ is a symmetric positive definite matrix. This assumption allows us to exploit Theorem 15 for more various types of short memory components in low

fMRI Signals

Estimation of
memory parameter

- Wavelet maximum likelihood (**ML**)
- Wavelet least-mean-squares (**LMS**)

Estimation of
short memory
covariance

- SDF-based method (**SDF**)
- Covariance-based method (**COV**)
- Linearity-based method (**LIN**)
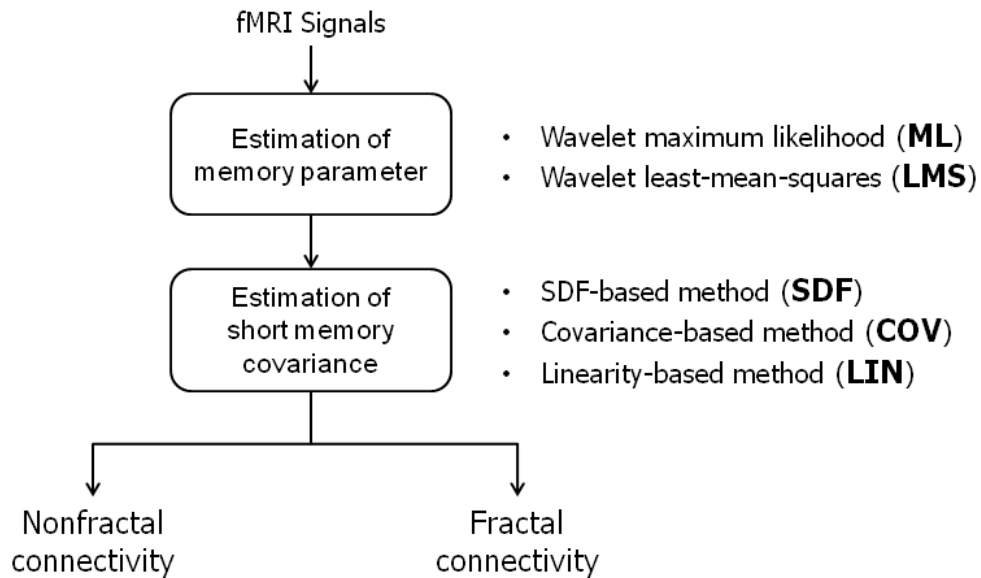
Nonfractal
connectivity

Fractal
connectivity

Figure 4.5: The process of estimating fractal connectivity and nonfractal connectivity.

frequencies. All estimators proposed in this section are based on this assumption.

The overall estimation procedure is depicted in Figure 4.5. It is organized as two steps: (1) the estimation of memory parameters and (2) the estimation of short memory covariance matrix. Based on these information, either nonfractal connectivity or fractal connectivity can be computed. It should be noticed that memory parameters should be estimated *a priori* as a prerequisite to estimating fractal-based connectivities. In Section 4.3.1, two wavelet-based univariate estimators of memory parameter are introduced: the least-mean-squares (LMS) method and the maximum likelihood (ML) method. Along with these univariate method, a novel multivariate LMS method is proposed. The performance of all estimators was evaluated through simulation studies. In Section 4.3.2, three wavelet-based estimation methods for both nonfractal connectivity and fractal connectivity are proposed: (1) the SDF(Spectral density function)-based method, (2) the covariance-based method, and (3) the linearity-based method. These estimators are comparatively evaluated through simulation studies.

4.3.1 Estimation of memory parameters

Several estimators of memory parameter have been introduced in Section 2.7.1. Here a new class of long memory estimators based on the wavelet transform are introduced. One is the *parametric* estimation based on maximum likelihood while the other is the *semi-parametric* estimation based on least-mean-square (LMS) residuals. In addition, the effect of multivariate extension of the wavelet-based LMS estimator is verified by comparing it with the univariate estimators such as ML and LMS methods.

4.3.1.1 Maximum likelihood estimation

Let $\mathbf{x} = [x_1, \cdots, x_n]^T$ be the realization of a Gaussian FI process with memory parameter d where $\mathbb{E}[x(t)] = 0$ and $n = 2^J$ for $J \in \mathbb{Z}$, and whose dth order difference process $u(t) = (1 - \mathcal{B})^d x(t)$ is a Gaussian white noise process with variance γ. Then, the likelihood function for memory parameter d and short memory variance γ is given by

$$L\left(\hat{d}, \hat{\gamma} \,|\mathbf{x}\right) \doteq \frac{1}{(2\pi)^{n/2} \,|\mathbf{\Sigma}|^{1/2}} e^{-\mathbf{x}^T \mathbf{\Sigma}^{-1} \mathbf{x}/2}. \tag{4.16}$$

where $\mathbf{\Sigma}$ is a $n \times n$ matrix whose (i, j)th element is $\mathbb{E}[x(i)x(i + j)]$ (Percival & Walden, 2006). Then, the optimal values of $\hat{d}$ and $\hat{\gamma}$ can be obtained as the values which maximize the likelihood function $L\left(\hat{d}, \hat{\gamma} \,|\mathbf{x}\right)$. It is called the *exact maximum likelihood (ML) estimator*. However, this exact ML estimator requires high computational complexity and becomes more unstable to compute the likelihood function as $d \to 1/2$.

Let $\mathcal{W}$ be a wavelet transform matrix of $x(t)$ (see Chapter 4.6 in Percival & Walden (2006)) and $\mathbf{\Lambda} = \text{diag}[\Lambda_j]$ be a wavelet variance matrix with $\Lambda_j = \mathbb{E}[W_{j,t}^2]$ for $j = 1, ..., J$. As an alternative to the exact ML estimator, the matrix $\mathbf{\Sigma}$ can be approximated based on the wavelet transform as follows

$$\mathbf{x}^T \mathbf{\Sigma}^{-1} \mathbf{x} \approx \mathcal{W}^T \mathbf{\Lambda} \mathcal{W} = \frac{1}{\gamma} \left(\frac{V_J^2}{C_{J+1}(d)} + \sum_{j=1}^{J} \frac{1}{C_j(d)} \sum_{t=0}^{n_j-1} W_{j,t}^2 \right) \tag{4.17}$$

where $W_j = [W_{j,t}]$ for $t = 1, \cdots, n_j$ denotes the jth level wavelet coefficients of $x(t)$ and V_{J+1} is the scaling coefficients at scale $J + 1$, and $C_j(d)$ is given by

$$
\begin{aligned}
C_j(d) &\doteq \int_{-1/2}^{1/2} \mathcal{H}_j(\lambda) \left| 1 - e^{-i\lambda} \right|^{-2d} \mathrm{d}\lambda \\
&= 2^{j+1} \int_{1/2^{j+1}}^{1/2^j} \left| 1 - e^{-i\lambda} \right|^{-2d} \mathrm{d}\lambda
\end{aligned}
\tag{4.18}
$$

with the squared gain function $\mathcal{H}_j(\lambda)$ of the jth level wavelet filter given in (4.5). Then, the log-likelihood function is given from (4.16) and (4.17) by

$$
\begin{aligned}
l\left(d, \gamma \,|\mathbf{x}\right) &\doteq -2 \log L\left(d, \gamma | \mathbf{x}\right) - n \log(2\pi) \\
&= N \log \gamma + \log C_{J+1}(d) + \sum_{j=1}^{J} N_j \log C_j(d) + \frac{\hat{\gamma}}{\gamma}
\end{aligned}
\tag{4.19}
$$

where $\hat{\gamma}$ can be regarded as the estimate of γ as follows

$$
\hat{\gamma} \doteq \frac{1}{n} \left(\frac{V_J^2}{C_{J+1}(d)} + \sum_{j=1}^{J} \frac{1}{C_j(d)} \sum_{t=0}^{n_j-1} W_{j,t}^2 \right).
\tag{4.20}
$$

Therefore, d and γ can be estimated by minimizing the log-likelihood function $l\left(d, \gamma \,|\mathbf{x}\right)$. It is called the *wavelet-based maximum likelihood (WML) estimator*. The log-likelihood function in (4.19) can be simplified as the *reduced log-likelihood function* from the Brockwell and Davis' method (Brockwell & Davis, 2009) by skipping the estimation of γ:

$$
\begin{aligned}
\tilde{l}(d|\mathbf{x}) &\doteq \tilde{l}\left(d, \hat{\gamma} \,|\mathbf{x}\right) - n \\
&= N \log \hat{\gamma}(d) + \log C_{J+1}(d) + \sum_{j=1}^{J} n_j \log C_j(d).
\end{aligned}
\tag{4.21}
$$

4.3.1.2 LMS estimation

The scale-dependent variance equation (4.6) indicates that the wavelet variance $\nu(j)$ exhibits approximately linear trend in the log-log plot as j increases. In other words, the following linear equation is obtained by taking logarithm to both sides

of (4.6):

$$\log_2 [\nu(j)] \approx 2dj + c. \tag{4.22}$$

It enables us to nonparametrically estimate the memory parameters $\hat{d}$ by linear regression over a given scale interval $\mathcal{J} = J_1 \rightarrow J_2$ on the basis of the biased estimator of wavelet variance given by

$$\widehat{\nu}_m(j) = \frac{1}{n_j 2^j} \sum_{t=1}^{n_j} W_{j,t}^2 \tag{4.23}$$

where $n_j = n/2^j$ is the number of coefficients in scale j Percival & Walden (2006). The optimal values of d and c can be selected to minimize the sum of squares of residuals as follows

$$\sigma_{\text{LS}}^2 = \frac{1}{\Delta J} \sum_{j=J_1}^{J_2} \left[\log_2 \hat{\nu}(j) - 2\hat{d}j - \hat{c} \right]^2. \tag{4.24}$$

for $\Delta J = J_2 - J_1 + 1$. Therefore, $\hat{d}$ and $\hat{c}$ can be numerically calculated by

$$\hat{d} = \frac{\mathbf{L}^T}{2 \|\mathbf{L}\|^2} \left[\log \nu(j) \right]_j, \tag{4.25}$$

$$\hat{c} = \overline{[\log \nu(j)]}_j - \frac{\hat{d}}{2} (J_2 - J_1 + 1)(J_1 + J_2) \tag{4.26}$$

where $\mathbf{L} = [L_j]_j$ with $L_j = \log j - \sum_{j=J_1}^{J_2} \log j / \Delta J$. This method is called the *wavelet-based least-mean-squares (WLMS) estimator* (Percival & Walden, 2006). The scale interval $\mathcal{J}$ can be automatically determined in a similar manner with Achard et al. (2008) by

$$\mathcal{J}_{\text{opt}} = \arg \min_{\mathcal{J} \subset \mathbb{J}} \sigma_{\text{LS}}^2(\mathcal{J}) \tag{4.27}$$

where $\mathbb{J}$ is the space of all scale intervals. The scale interval which minimizes the minimum LMS residual is selected as the optimum scale range. This strategy is called the *automatic scale selection* for the LMS estimator. Specifying the *minimum scale interval* (MSI) ΔJ_{min} or the *lower scale bound* (LSB) J_L, such that $\mathcal{J}_{\text{opt}} \geq \Delta J_{min}$ and $J_1 \geq J_L$, is sometimes useful. In the case of a multivariate long memory process, the LMS residual criteria in (4.24) can be extended as

follows

$$\sigma_{\mathrm{LS}}^2(\mathcal{J}) = \frac{1}{\Delta J} \sum_{j=J_1}^{J_2} \sum_{m=1}^{q} \left\{ \log_2\left[\widehat{\nu}_m\right] - 2\hat{d}_m j - \hat{c}_m \right\}^2. \tag{4.28}$$

In (4.28), all memory parameters are simultaneously determined but without considering either covariance or correlation among long memory processes. In this reason this extended estimator is called the *semi-multivariate WLMS estimator*. An extension of the semi-multivariate WLMS estimator is proposed in the subsequent Section by considering the covariance and correlation between two time series.

4.3.1.3 Multivariate WLMS estimation

In this section, an advanced multivariate least mean squares (LMS) estimator for a vector FI process is proposed as a multivariate extension of the bivariate estimator suggested by Achard et al. (2008). Let $\mathbf{x}(t)$ be a vector FI process with memory parameter $\mathbf{d}$. Then, the following linear system is obtained from (4.6) and (4.7):

$$\log_2\left(\nu_{m,n}(j)\right) = (d_m + d_n)j + c_{m,n}, \tag{4.29}$$

$$\log_2\left(\rho_{m,n}(j)\right) = c_{m,n} - \frac{1}{2}\left(c_{m,m} + c_{n,n}\right), \tag{4.30}$$

The *multivariate WLMS estimator* can be made over a given scale interval $\mathcal{J} = J_1 \rightarrow J_2$ by

$$\begin{aligned}
\sigma_{\mathrm{LS}}^2(\mathcal{J}) &= \frac{1}{J_2 - J_1 + 1} \sum_{j=J_1}^{J_2} \left[\sum_{m=1}^{p} \sum_{n=m}^{p} \left(\log_2 \gamma_{m,n}^{(j)} - (d_m + d_n)j - c_{m,n} \right)^2 \right. \\
&\quad \left. + \sum_{m=1}^{p-1} \sum_{n=m+1}^{p} \left(\log_2 \rho_{m,n}^{(j)} - c_{m,n} + \frac{1}{2}(c_{m,m} + c_{n,n}) \right)^2 \right].
\end{aligned} \tag{4.31}$$

The solution $\mathbf{p} := [d_1, \cdots, d_p, c_1, \cdots, c_p, c_{1,2}, \cdots, c_{m,n}, \cdots, c_{p-1,p}]^T$ can be numerically found from

$$\mathbf{p} = \mathbf{A}^{-1}\mathbf{e} \tag{4.32}$$

where

$$\mathbf{A} = \begin{pmatrix} 2S_2\mathbf{L}_1 & 4S_1\mathbf{I}_{p\times p} & 2S_1\mathbf{L}_2 \\ 4S_1\mathbf{I}_{p\times p} & (\Delta_J/2)\mathbf{L}_1 & -\Delta_J\mathbf{L}_2 \\ 2S_1\mathbf{L}_2^T & -\Delta_J\mathbf{L}_2^T & 4\Delta_J\mathbf{I}_{r\times r} \end{pmatrix}, \tag{4.33}$$

$$e(k) := \begin{cases} \displaystyle\sum_{j=J_1}^{J_2} \left(4j\log_2 \gamma_{k,k}^{(j)} + 2j \sum_{l\in\mathbb{K}/k} \log_2 \gamma_{k,l}^{(j)} \right) & \text{if } 1 \le k \le p \\[2em] \displaystyle\sum_{j=J_1}^{J_2} \left(2\log_2 \gamma_{k-p,k-p}^{(j)} - \sum_{l\in\mathbb{K}/k-p} \log_2 \rho_{k-p,l}^{(j)} \right) & \text{if } p+1 \le k \le 2p \\[2em] \displaystyle\sum_{j=J_1}^{J_2} \left(2\log_2 \gamma_{k-2p,k-2p}^{(j)} + 2\log_2 \rho_{k-2p,k-2p}^{(j)} \right) & \text{if } 2p+1 \le k \le p(p+3)/2. \end{cases} \tag{4.34}$$

with $S_1 := \sum_{j=J_1}^{J_2} j$, $S_2 := \sum_{j=J_1}^{J_2} j^2$, $\Delta_J = J_2 - J_1 + 1$. The $p \times p$ matrix $\mathbf{L}_1 := [L_1(k,l)]_{k,l}$ and the $r \times r$ matrix $\mathbf{L}_2 := [L_2(k,l)]_{k,l}$ with $r = p(p-1)/2$ are defined by

$$L_1(k,l) := \begin{cases} p+3 & \text{if } k = l, \\ 1 & \text{otherwise.} \end{cases} \tag{4.35}$$

$$L_2(k,l) = \begin{cases} 1 & \text{if } \alpha = k \text{ or } \alpha + \beta = k, \\ 0 & \text{otherwise.} \end{cases} \tag{4.36}$$

where α denotes the maximum integer satisfying $\lfloor l/\varrho(\alpha) \rfloor = 1$ and $\varrho(\alpha) = (p - \alpha)(p + \alpha - 1)/2$, and $\beta = \alpha + l - \varrho(\alpha)$.

4.3.2 Estimation of fractal-based connectivities

The theory on asymptotic wavelet covariance and wavelet correlation in (4.6) and (4.7) suggests that both nonfractal connectivity and fractal connectivity can be approximately estimated if memory parameters are known. Therefore, it is a necessary step to estimate the memory parameters of resting state BOLD signals by using one of estimators in Section 4.3.1 in advance before starting fractal-based connectivity analyses. In this section, two univariate wavelet-based

estimators of memory parameter are adopted: maximum-likelihood (ML) and least-mean-squares (LMS) methods. Given the memory parameters, the short memory covariance matrix is estimated by using one of three wavelet-based techniques: SDF-based (SDF), covariance-based (COV), and linearity-based (LIN) methods. In results, six pairs of estimation methods are made by combining a memory parameter estimator with a short memory covariance estimator: LMS-SDF, LMS-COV, LMS-LIN, ML-SDF, ML-COV, and ML-LIN. After both the memory parameter $\hat{\mathbf{d}}$ and the short memory covariance $\hat{\boldsymbol{\Sigma}}_u = [\hat{\gamma}_{m,n}]$ are estimated, the nonfractal connectivity $\hat{\xi}_{m,n}$ between $x_m(t)$ and $x_n(t)$ can be calculated by using (4.4) as follows

$$\hat{\xi}_{m,n} = \frac{\hat{\gamma}_{m,n}}{\sqrt{\hat{\gamma}_{m,m}\hat{\gamma}_{n,n}}}. \tag{4.37}$$

Likewise, the fractal connectivity $\hat{\varrho}_{m,n}$ can be estimated from (4.7) as follows

$$\hat{\varrho}_{m,n} = \hat{\xi}_{m,n}\psi(\hat{d}_m, \hat{d}_n) \tag{4.38}$$

where

$$\psi(\hat{d}_m, \hat{d}_n) \doteq \frac{B_1(\hat{d}_m, \hat{d}_n)}{\sqrt{B_1(\hat{d}_m, \hat{d}_m)B_1(\hat{d}_n, \hat{d}_n)}} \cos\left(\frac{\pi}{2}(\hat{d}_m - \hat{d}_n)\right). \tag{4.39}$$

In this section, three wavelet-based estimators of short memory covariance are described minutely.

4.3.2.1 SDF-based method

The estimator $\hat{\gamma}_{m,n}$ of short memory covariance can be parametrically computed by (4.20). If $\mathbb{E}[\mathbf{x}(t)] = 0$, the scaling coefficients are eliminated; $(V_J^{(m)})^T V_J^{(n)} = 0$ since $V_{J,0} = \overline{x}(t)\sqrt{N}$ where $\overline{x}(t)$ is the sample mean of $x(t)$. In final, the following estimator is obtained

$$\hat{\gamma}_{m,n} \doteq \frac{1}{N} \sum_{j=1}^{J} \frac{1}{C_j(\hat{d}_m, \hat{d}_n)} \sum_{t=0}^{N_j-1} W_{j,t}^{(m)} W_{j,t}^{(n)} \tag{4.40}$$

where $C_j(\hat{d}_m, \hat{d}_n)$ is given from (4.18) by

$$C_j(\hat{d}_m, \hat{d}_n) \doteq 2^{j+1} \int_{1/2^{j+1}}^{1/2^j} \Re\left[\left(1 - e^{-i\lambda}\right)^{-\hat{d}_m} \left(1 - e^{i\lambda}\right)^{-\hat{d}_n}\right] \mathrm{d}\lambda. \qquad (4.41)$$

Since the short memory covariance $\hat{\gamma}_{m,n}$ is parametically computed based on the template of cross-spectral density function (SDF) for a vector FIN process, this approach is called the *SDF-based method*.

4.3.2.2 Covariance-based method

The alternative approach to estimating the short memory covariance $\hat{\gamma}_{m,n}$ is to exploit the properties such that the sum of wavelet covariances over all scales is identical to the covariance of a time series as follows

$$\hat{\nu}_{m,n} = \frac{\mathbb{E}\left(V_{J,0}^{(m)} V_{J,0}^{(n)}\right)}{N} + \sum_{j=1}^{J} \frac{\mathbb{E}\left(W_{j,t}^{(m)} W_{j,t}^{(n)}\right)}{2^j} \qquad (4.42)$$

where $\hat{\nu}_{m,n}$ is the sample covariance of $x_m(t)$ and $x_n(t)$ (see Chapter 9.2 in Percival & Walden (2006)). If $\mathbb{E}[\mathbf{x}(t)] = 0$, the following approximation on the partial sum of wavelet covariances over the scale range $\mathcal{J} = J_1 \rightarrow J_2$ is satisfied

$$\hat{\nu}_{m,n}(\mathcal{J}) \approx \hat{\gamma}_{m,n} B_1\left(\hat{d}_m, \hat{d}_n\right) \cos\left(\frac{\pi}{2}(\hat{d}_m - \hat{d}_n)\right) \sum_{j=J_1}^{J_2} 2^{j(\hat{d}_m + \hat{d}_n - 1)} \qquad (4.43)$$

where

$$\hat{\nu}_{m,n}(\mathcal{J}) = \frac{1}{N} \sum_{j=J_1}^{J_2} 2^{-j} \sum_{t=0}^{N_j - 1} W_{j,t}^{(m)} W_{j,t}^{(n)}. \qquad (4.44)$$

Hence, the following estimator of $\hat{\gamma}_{m,n}$ can be obtained from (4.43):

$$\hat{\gamma}_{m,n} \approx \frac{\hat{\nu}_{m,n}(\mathcal{J})}{B_1\left(\hat{d}_m, \hat{d}_n\right) \cos\left(\frac{\pi}{2}(\hat{d}_m - \hat{d}_n)\right) \sum_{j=J_1}^{J_2} 2^{j(\hat{d}_m + \hat{d}_n - 1)}}. \qquad (4.45)$$

This approach is called the *covariance-based method* since it is based on the sum of wavelet covariances. If $J_1 = 1$, $J_2 \to \infty$, and $d_m + d_n < 1$,

$$\hat{\gamma}_{m,n} \approx \frac{\hat{\nu}_{m,n}(1 - 2^{\hat{d}_m + \hat{d}_n - 1})}{B_1\left(\hat{d}_m, \hat{d}_n\right) \cos\left(\frac{\pi}{2}(\hat{d}_m - \hat{d}_n)\right) 2^{\hat{d}_m + \hat{d}_n - 1}} \tag{4.46}$$

since

$$\sum_{j=1}^{J} 2^{j(d_m + d_n - 1)} = \frac{2^{d_m + d_n - 1}(1 - 2^{J(d_m + d_n - 1)})}{1 - 2^{d_m + d_n - 1}}. \tag{4.47}$$

Therefore, (4.46) corresponds to (3.46) in the case that $d_m + d_n < 1$.

4.3.2.3 Linearity-based method

The other wavelet-based estimator of short memory covariance $\hat{\gamma}_{m,n}$ can be obtained based on the linearity of wavelet covariance over scales. The equation (4.6) in Theorem 15 can be extended to the multivariate case that implies the approximate linearity in log scale as follows

$$\log_2\left[\nu_{m,n}(j)\right] \approx (d_m + d_n)\,j + c_{m,n} \tag{4.48}$$

where

$$c_{m,n} = \log_2\left[\gamma_{m,n}B_1(d_m, d_n) \cos\left(\frac{\pi}{2}(d_m - d_n)\right)\right]. \tag{4.49}$$

Therefore, we have the following estimator of $\gamma_{m,n}$ from (4.49)

$$\hat{\gamma}_{m,n} = \frac{2^{\hat{c}_{m,n}}}{B_1(\hat{d}_m, \hat{d}_n) \cos\left(\frac{\pi}{2}(\hat{d}_m - \hat{d}_n)\right)} \tag{4.50}$$

where $\hat{c}_{m,n}$ is determined from (4.26) as the sample mean of $\hat{c}_{m,n}(j)$ over the scale range $\mathcal{J} = J_1 \to J_2$ as follows

$$\hat{c}_{m,n} = \frac{1}{J_2 - J_1 + 1} \sum_{j=J_1}^{J_2} \left[\log_2 \hat{\nu}_{m,n}(j) - (\hat{d}_m + \hat{d}_n)j\right]. \tag{4.51}$$

This approach is called the *linearity-based method*, and classified as a semiparametric estimator because the short memory covariance $\hat{\gamma}_{m,n}$ is determined based

on the asymptotic property of wavelet covariance for a vector FI process as well as the nonparametric estimation of $\hat{c}_{m,n}$ as shown in (4.50).

4.4 Simulation studies

In this section the proposed wavelet-based estimators of memory parameter and nonfractal connectivity are statistically evaluated through simulation studies. First, the performance of the multivariate WLMS estimator of memory parameter proposed in Section 4.3.1.3 is compared with the univariate wavelet-based estimators such as WML and WLMS methods especially in the case of serious contamination due to additive noises. Next, three wavelet-based estimators of nonfractal connectivity proposed in Section 4.3.2 are comparatively evaluated.

4.4.1 Estimation of memory parameters

To compare the performance of the multivariate WLMS estimator (abbreviated as MS) with those of univariate WLMS estimator (US) and the maximum likelihood estimator (ML) (see Section 4.3.1), a special type of vector FI processes were simulated through Monte Carlo method with 100 repetition as follows. Let $\mathbf{x}^{(L)}(t) = \{x_1, x_2, x_3, x_4\}$ be a vector FI process with memory parameter $\mathbf{d}$ whose dth order difference process $\mathbf{u}(t) = (1 - \mathcal{B})^{\mathbf{d}}\mathbf{x}^{(L)}(t)$ is a vector Gaussian white noise process is given by

$$\mathbf{u}(t) = \mathbf{A}\varepsilon(t) \tag{4.52}$$

where $\varepsilon_i(t)$ for $i = 1, \cdots, q$ is an *i.i.d.* random variable where

$$\mathrm{cov}(\varepsilon_m(t), \varepsilon_n(t)) = \begin{cases} 1 & \text{if } m = n \\ 0 & \text{if } m \neq n, \quad \text{and} \end{cases} \tag{4.53}$$

$$\mathbf{A} = \begin{pmatrix} 1 & 0 & \cdots & \cdots & 0 \\ 0 & 1 & a & \cdots & a \\ \vdots & a & \ddots & & \vdots \\ \vdots & \vdots & & 1 & a \\ 0 & a & \cdots & a & 1 \end{pmatrix}. \tag{4.54}$$

for $a = (1 \pm \sqrt{1 - b\rho})/b$ and $b = \rho(q - 2) - (q - 3)$. In this case, $\mathbf{u}(t)$ has cross-correlation $\text{cor}[u_i(t)u_j(t)] = \rho$ for $\forall i, j > 1$ and $i \neq j$. Then, an FI process $x_i^{(L)}(t)$ can be simulated by convolving $u_i(t)$ with the LMF filter defined in (2.94). This simplification of vector FI processes for simulation studies is without loss of generality although the estimators are available for more diverse types of long memory processes. To test the performance of estimators in the presence of perturbation with the predefined signal-to-noise ratio (SNR), $x_i^{(L)}(t)$ was also perturbed by a Gaussian white noise process with variance $\sigma_e^2 = \mathbb{E}\left[(x_i^{(L)}(t))^2\right] 10^{-\text{SNR}/10}$ as follows

$$x_i(t) = x_i^{(L)}(t) + \sigma_e e(t). \tag{4.55}$$

Figure 4.6 and 4.7 show the comparison of three wavelet-based estimators when $\rho = 0.2$ and $\rho = 0.8$ respectively. In each figure, the first and second columns correspond to $SNR = \infty$ and $SNR = 1$ respectively. Also, Case A, Case B, and Case C correspond to $\mathbf{d} = \mathbf{d}_A \doteq [0.1, 0.3, 0.7, 0.9]$, $\mathbf{d} = \mathbf{d}_B \doteq [-0.3, -0.1, 0.1, 0.3]$, and $\mathbf{d} = \mathbf{d}_C \doteq [0.3, 0.3, 0.3, 0.3]$. The simulation was performed with the parameters: the number of time points $N = 2^15$, and $LSB = 1$ or 3 (for $SNR = \infty$ and $SNR = 1$ respectively) (see Section 4.3.1.2).

When $\mathbf{x}(t) = \mathbf{x}^{((L)}(t)$ where $SNR = \infty$, the wavelet ML estimator showed the least bias and consistency for all cases (see the first column of Figure 4.6 and 4.7). On the other hand, the univariate WLMS estimator was most biased expect Case B while the multivariate WLMS estimator is less biased but less consistent. It is manifest that the wavelet ML estimator can be regarded as the best choice for a pure FI process.

When the FI process is contaminated by a Gaussian white noise, the wavelet ML estimator was seriously biased for Case A and C while it was less biased for Case B. By contrast, the multivariate WLMS estimator was less biased for Case A and Case C although it still had low consistency. More detailed statistics are

Table 4.1: The bias and consistency of the wavelet-based estimators for memory parameter when $\rho = 0.2$.

Case A: $\mathbf{d} = [0.1, 0.3, 0.7, 0.9]$									
		Bias				Std			
d_i		0.1	0.3	0.7	0.9	0.1	0.3	0.7	0.9
SNR=∞	MS	0.193	0.002	-0.071	-0.130	0.039	0.037	0.035	0.037
	US	-0.010	-0.030	-0.103	-0.170	0.015	0.018	0.020	0.021
	ML	-0.006	-0.007	0.003	0.005	0.005	0.005	0.005	0.006
SNR=1	MS	0.123	0.033	-0.077	-0.177	0.061	0.065	0.090	0.084
	US	-0.028	-0.040	-0.124	-0.259	0.014	0.016	0.013	0.011
	ML	-0.044	-0.116	-0.382	-0.578	0.005	0.004	0.004	0.004

Case B: $\mathbf{d} = [-0.3, -0.1, 0.1, 0.3]$									
		Bias				Std			
d_i		-0.3	-0.1	0.1	0.3	-0.3	-0.1	0.1	0.3
SNR=∞	MS	0.229	0.031	0.011	-0.005	0.041	0.035	0.037	0.036
	US	0.010	0.002	-0.013	-0.037	0.017	0.017	0.018	0.017
	ML	0.002	-0.002	-0.005	-0.007	0.005	0.005	0.004	0.005
SNR=1	MS	0.417	0.083	-0.005	-0.009	0.061	0.062	0.060	0.060
	US	0.235	0.053	-0.028	-0.040	0.018	0.018	0.017	0.017
	ML	0.181	0.046	-0.045	-0.116	0.005	0.004	0.004	0.004

Case C: $\mathbf{d} = [0.3, 0.3, 0.3, 0.3]$									
		Bias				Std			
d_i		0.3	0.3	0.3	0.3	0.3	0.3	0.3	0.3
SNR=∞	MS	0.158	-0.026	-0.017	-0.026	0.049	0.43	0.040	0.055
	US	-0.072	-0.075	-0.072	-0.075	0.037	0.035	0.037	0.037
	ML	-0.009	-0.009	-0.009	-0.008	0.005	0.005	0.005	0.005
SNR=1	MS	0.104	-0.059	-0.049	-0.045	0.067	0.072	0.060	0.054
	US	-0.124	-0.131	-0.129	-0.130	0.054	0.046	0.053	0.055
	ML	-0.117	-0.117	-0.117	-0.116	0.004	0.004	0.004	0.004

(a) Case A

(b) Case A with SNR=1

(c) Case B

(d) Case B with SNR=1

(e) Case C

(f) Case C with SNR=1
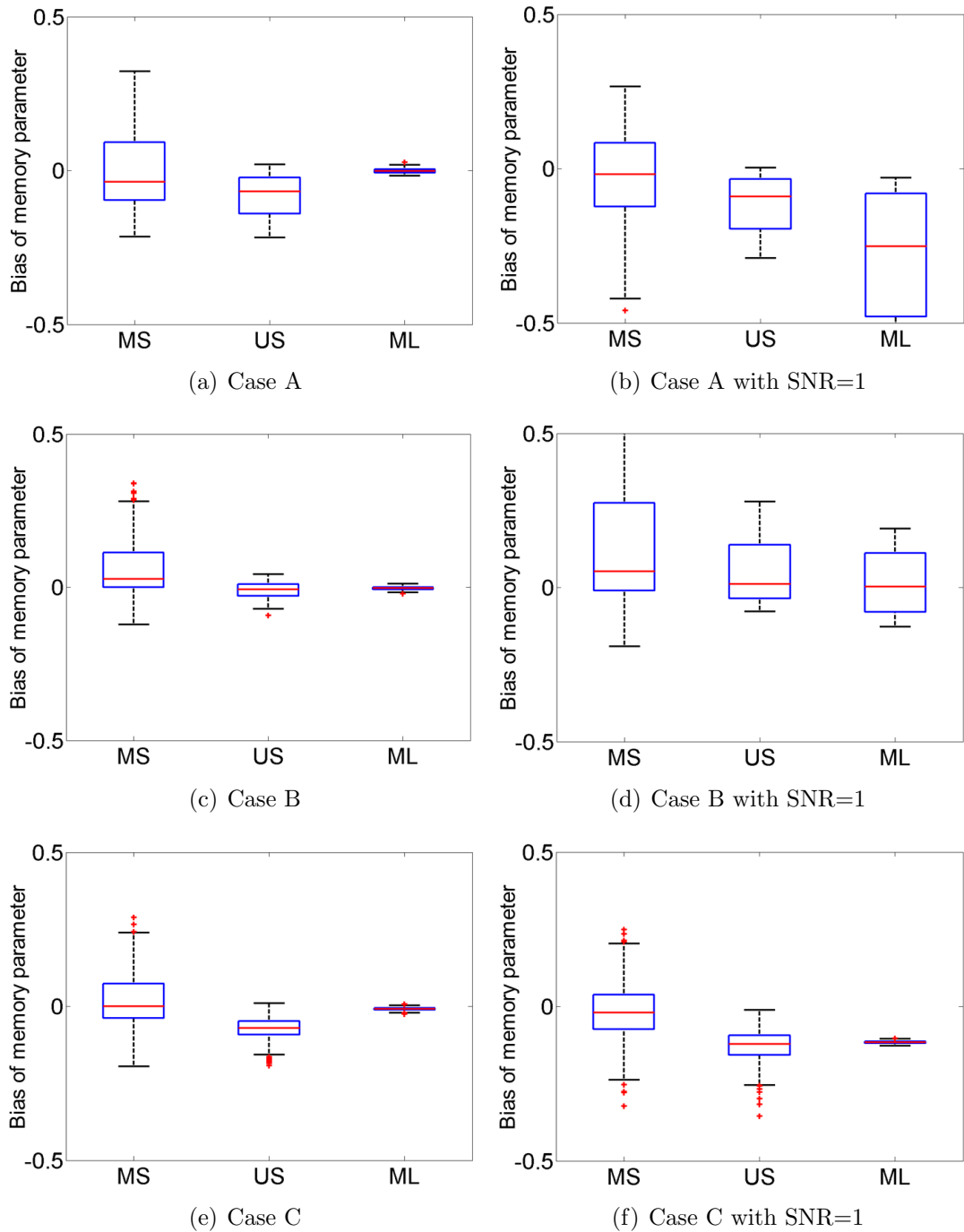
Figure 4.6: Box plots of bias in estimation of memory parameters when the short memory correlation is given as 0.2.
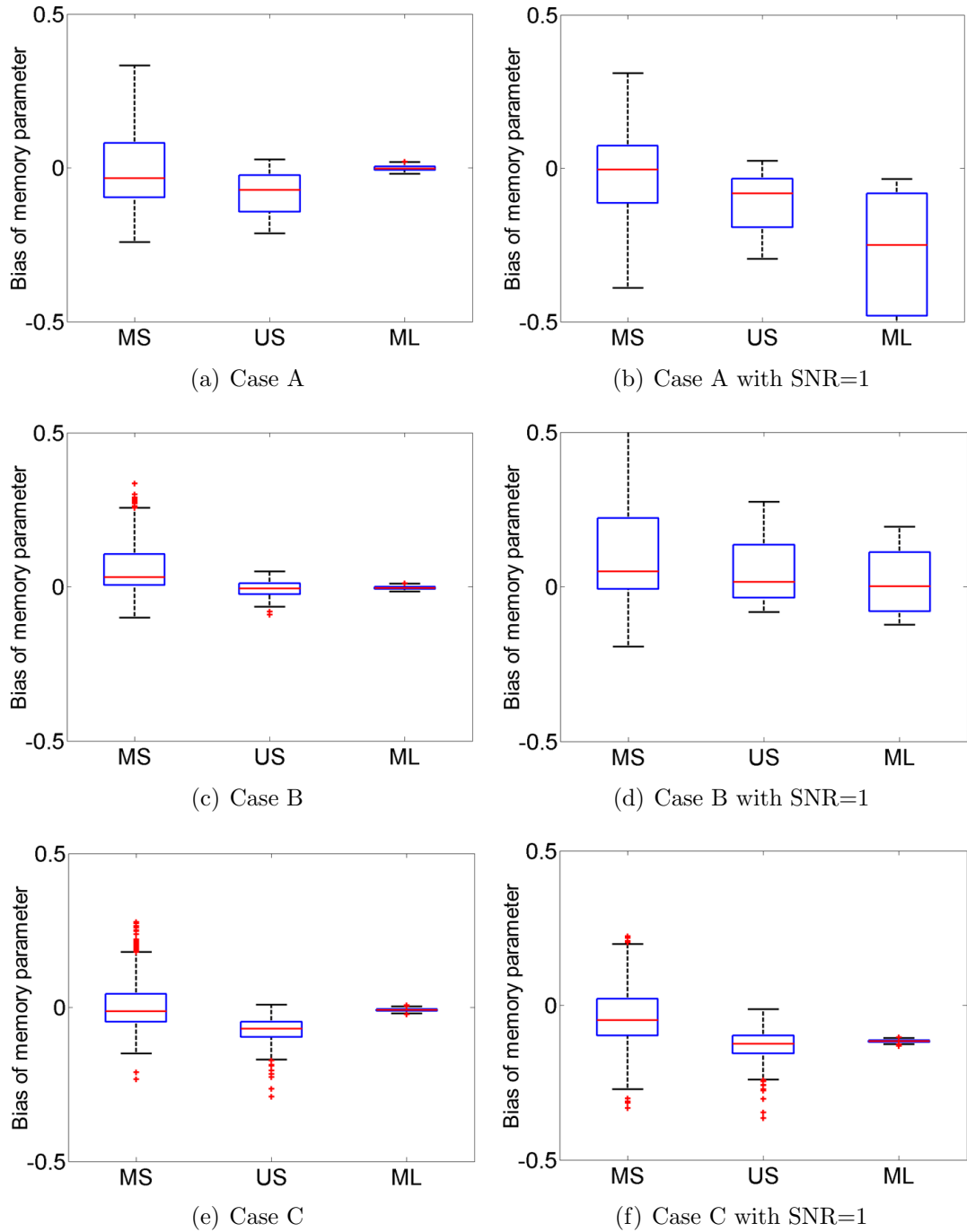
Figure 4.7: Box plots of bias in estimation of memory parameters when the short memory correlation is given as 0.8.

introduced in Table 4.1. The multivariate WLMS estimator exhibited the best performance when the FI process has long memory with $d > 0$ while its performance had fallen when $d < 0$. All of these results suggest that the multivariate WLMS estimator has the best performance among wavelet-based methods when resting state BOLD signals are seriously corrupted by white noise.

4.4.2   Estimation of fractal-based connectivities

This section reports the evaluation of the wavelet-based estimators for nonfractal connectivity such as the SDF-based method, the covariance-based method, and the linearity-based method (see Section 4.3.2). As suggested in Section 4.3, these connectivity estimators should be combined with one of memory parameter estimators. Here the univariate WLMS estimator and the wavelet ML estimator were employed. Finally, six pairs of estimators are finally tested and named the LMS-LIN, LMS-COV, LMS-SDF, ML-LIN, ML-COV, ML-SDF methods. In particular, the effects of short memory condition, dimension, and length of time series on the estimation of nonfractal connectivity are analyzed.

While the fractionally integrated noise (FIN) was simulated for the estimation of memory parameters in the previous section, the multivariate ARFIMA$(p, \mathbf{d}, 0)$ processes are simulated (see Section 2.7.2.2). Let $\mathbf{x}(t) = \{x_i(t); i = 1, \cdots, p\}$ be a vector FI process with memory parameter $\mathbf{d}$ whose dth order difference process $\mathbf{u}(t) = (1 - \mathcal{B})^{\mathbf{d}}\mathbf{x}^{(L)}(t)$ is an ARMA$(p, 0)$ process as follows

$$\mathbf{u}(t) = \mathbf{\Phi}_p^{-1}(L)\mathbf{A}\varepsilon(t). \tag{4.56}$$

where the innovation $\mathbf{A}$ and $\varepsilon(t)$ are given in (4.53) and (4.54), and

$$\mathbf{\Phi}_p(L) = \begin{pmatrix} \sum_{i=1}^p \varphi_{1,i} L^i & & 0 \\ & \ddots & \\ 0 & & \sum_{i=1}^p \varphi_{q,i} L^i \end{pmatrix}, \tag{4.57}$$

The memory parameters $\mathbf{d}$ were equally distributed over $d \in (-1/2, 1/2)$, and the simulation study was performed through Monte Carlo simulations with 100 repetition.

Effects of short memory condition and dimension

To study the effects of short memory conditions on the performance of estimators, four-dimensional ARFIMA$(p, d, 0)$ processes were simulated with four different types of short memory condition in (4.54) and (4.57):

(1A) $\mathbf{A} = \mathbf{I}$ and $\varphi_{k,i} = 0$
(1B) $\mathbf{A} = \mathbf{I}$, $\varphi_{k,1} = 0.9$ and $\varphi_{k,i} = 0$ for $i > 1$
(2A) $\mathbf{A} = \mathbf{A}_0$ and $\varphi_{k,i} = 0$
(2B) $\mathbf{A} = \mathbf{A}_0$, $\varphi_{k,1} = 0.9$ and $\varphi_{k,i} = 0$ for $i > 1$

where $\mathbf{d} = \{0.2, 0.4, 0.6, 0.8\}$ and $\mathbf{A}_0$ was set with $\rho = 0.3$ in (4.54). In the conditions (1A) and (1B), short memory processes $\mathbf{u}(t)$ is statistically independent of each other while the conditions (2A) and (2B) force short memory processes to be cross-correlated by the matrix $\mathbf{A}_0$. On the other hand, the conditions (1B) and (2B) let each process be autocorrelated.

Figure 4.8 shows the performance of six estimators for the above four short memory conditions. All estimators were less efficient for the conditions (1B) and (2B) where short memory parts were more auto-correlated. This deterioration in estimation efficiency is foreseeable because the short memory conditions in (1B) and (2B) make the convergence of short memory spectral density in (4.15) too precipitous over a short range of low frequencies. Hence, it should be noticed that the proposed wavelet-based estimators are inefficient when the short memory component $\mathbf{u}(t)$ does not strictly satisfy the assumption in (4.15). Nevertheless, the ML-LIN and ML-COV estimators of nonfractal connectivity were less biased than others even in the conditions (2A) and (2B) where short memory components are cross-correlated.

However, these estimators were significantly biased as the dimension p increases in the case that the true nonfractal connectivity ρ is large. Figure 4.9 and 4.10 show the performance of estimators with varying number of time series ($p = 2^1, 2^2, \cdots, 2^7$) when $\mathbf{u}(t)$ is given with the condition (2A) where $\rho = 0.2$ and $\rho = 0.8$ respectively. In this case, the short memory process $\mathbf{u}(t)$ can be regarded as a multivariate ARMA$(0, 0)$ process with innovation in (4.54). When the given correlation ρ of short memory components is small, the covariance-based estimators (LMS-COV and ML-COV) maintained the least bias even in large

(a) LMS-LIN
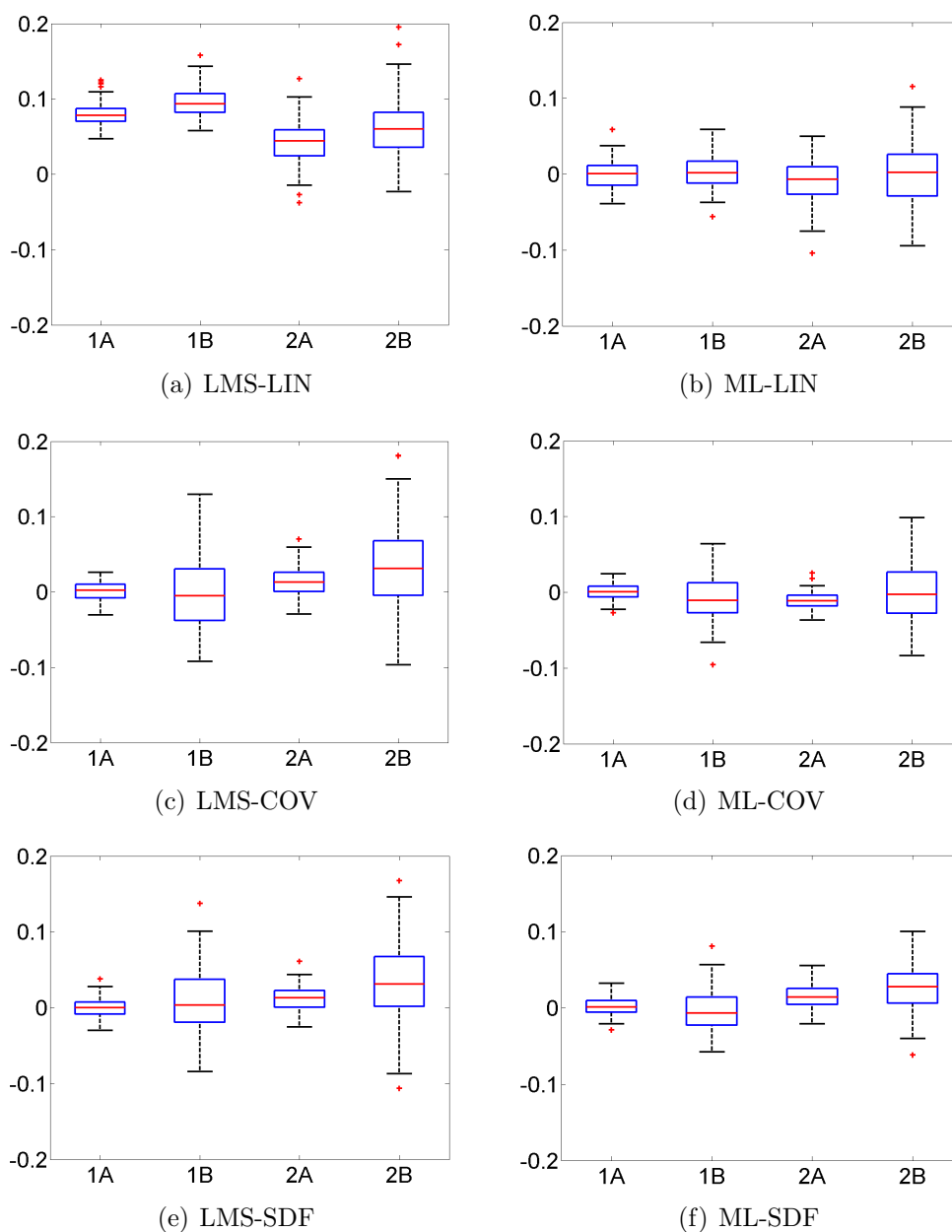
(b) ML-LIN

(c) LMS-COV

(d) ML-COV

(e) LMS-SDF

(f) ML-SDF

Figure 4.8: Box plots of bias in estimation of nonfractal connectivity for simulated ARFIMA$(p, d, 0)$ processes with different short memory conditions.

dimensions regardless of what estimator of memory parameter is applied (see Figure 4.9(c) and 4.9(d)) while the SDF-based estimators (LMS-SDF and ML-SDF) were greatly biased in large dimensions. However, the covariance-based estimators also became more biased in the case of large short memory correlation $\rho = 0.8$ (see Figure 4.10(c) and 4.10(d)). It indicates that high correlation of short memory components as well as large dimension result in the deterioration of consistency for most estimators except the LMS-LIN method. In other words, the performance of nonfractal connectivity estimators is manifestly influenced by both the number of time series and the correlation structure of short memory components, and the influence is more significant in larger dimensions.

Effects of length of time series

Fig. 4.11 illustrates the performance of nonfractal connectivity estimation with various numbers of time points. The multivariate FI processes, whose short memory $\mathbf{u}(t)$ was given with the condition (2A) where $\rho = 0$, were simulated with length $N = 2^9, 2^{10}, \cdots, 2^{15}$. Except the LMS-LIN method, most estimators became more consistent as the time length N increases. Note that the LMS-LIN method was unbiased even when the length of time series is very long. Indeed, the LMS-LIN and ML-LIN method are in prominent contrast although they are based on the linearity-based method in common. Hence, it suggests that the performance of nonfractal connectivity estimators may be subject to what method is exploited to estimate memory parameters.

Choice of estimators

Concluding the simulation studies, the covariance-based estimators (such as LMS-COV and ML-COV) are recommended as the best estimator of nonfractal connectivity in a high-dimensional brain network since they tend to be less biased in large dimensions than other wavelet-based estimators. Although the LMS-LIN estimator seems to be somewhat less biased even in large dimension than the LMS-COV and ML-COV methods, however its efficiency is seriously lowered. Fig 4.12 illustrates an example of nonfractal connectivity estimation based on the wavelet ML method. The nonfractal connectivity matrix estimated by the ML-
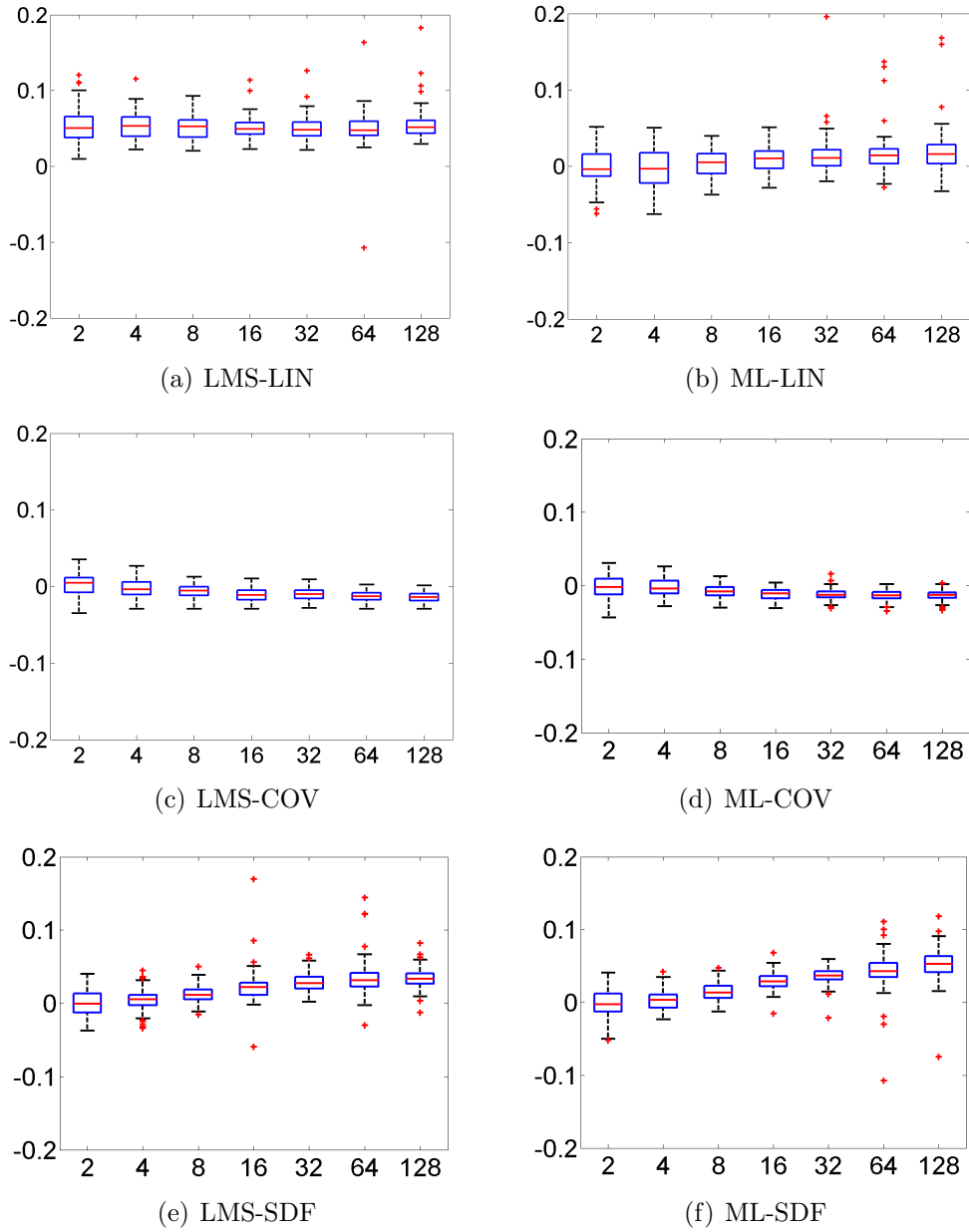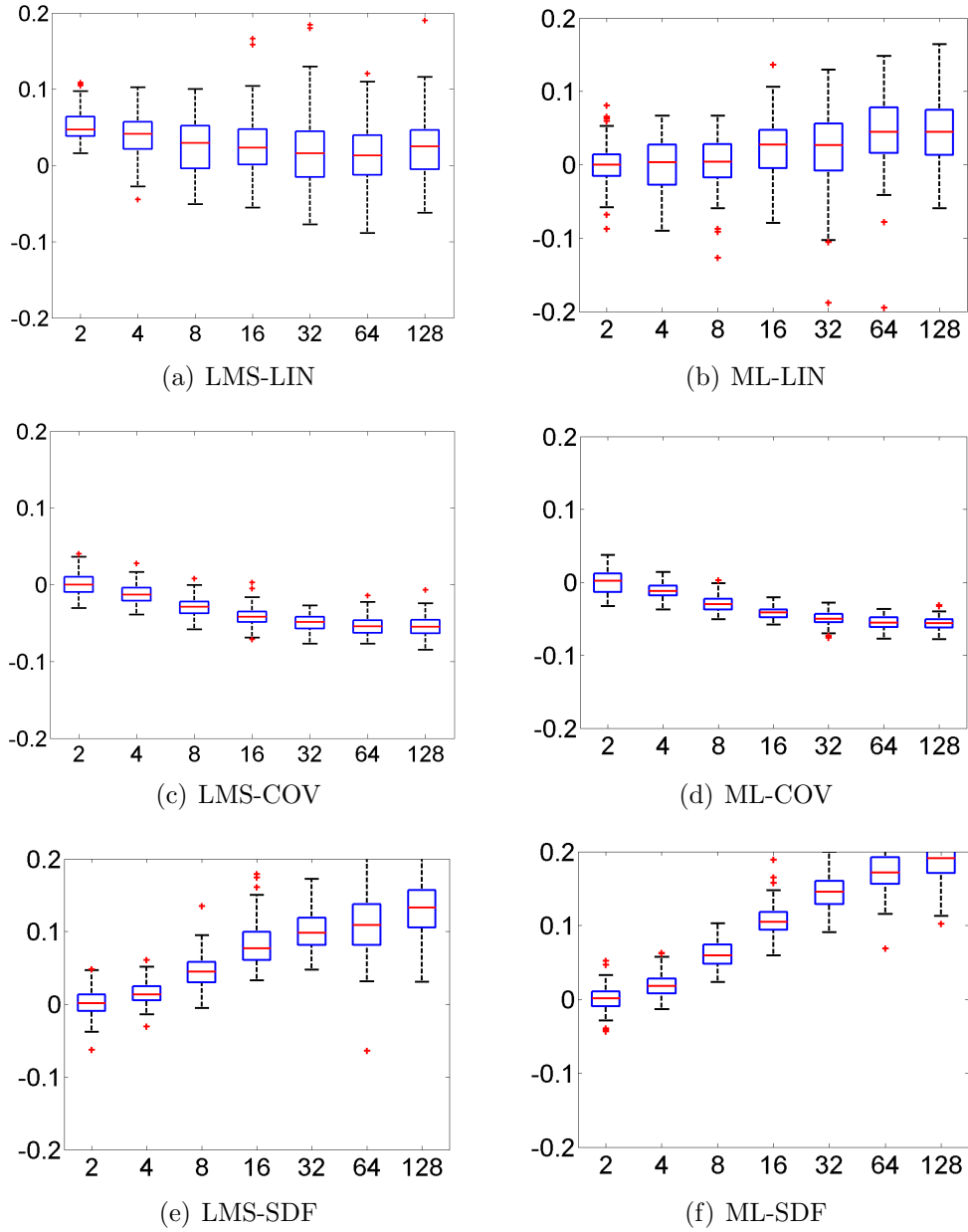
Figure 4.9: Box plots of bias in estimation of nonfractal connectivity for simulated ARFIMA$(0, d, 0)$ processes according to variable dimensions when the short memory correlation is $\rho = 0.2$.
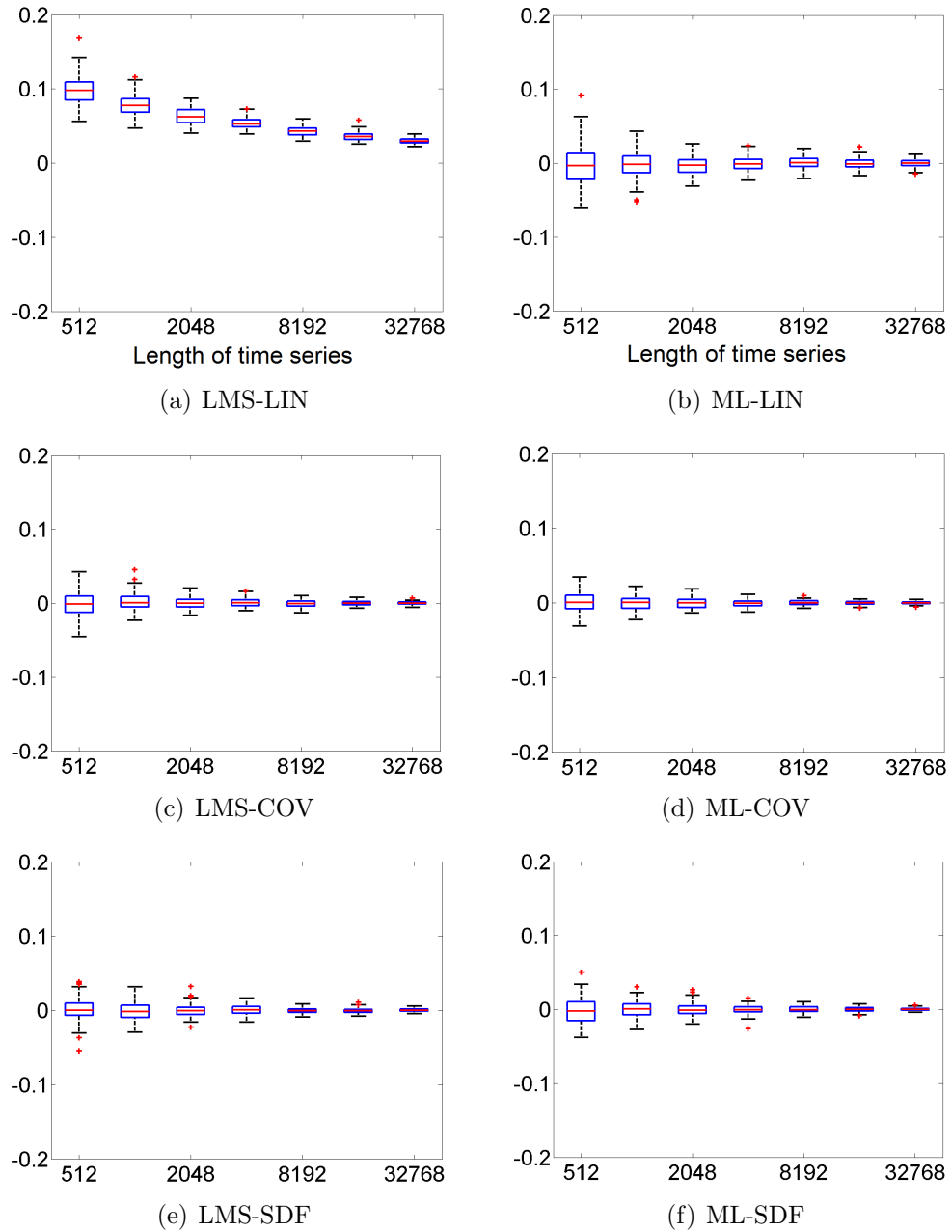
Figure 4.10: Box plots of bias in estimation of nonfractal connectivity for simulated ARFIMA$(0, d, 0)$ processes according to variable dimensions when the short memory correlation is $\rho = 0.8$.

(a) LMS-LIN

(b) ML-LIN

(c) LMS-COV

(d) ML-COV

(e) LMS-SDF

(f) ML-SDF

Figure 4.11: Box plots of bias in estimation of nonfractal connectivity for simulated ARFIMA$(0, d, 0)$ processes according to variable length of time series when the short memory correlation is $\rho = 0$.

(a) Short memory correlation

(b) ML-LIN

(c) ML-COV

(d) ML-SDF
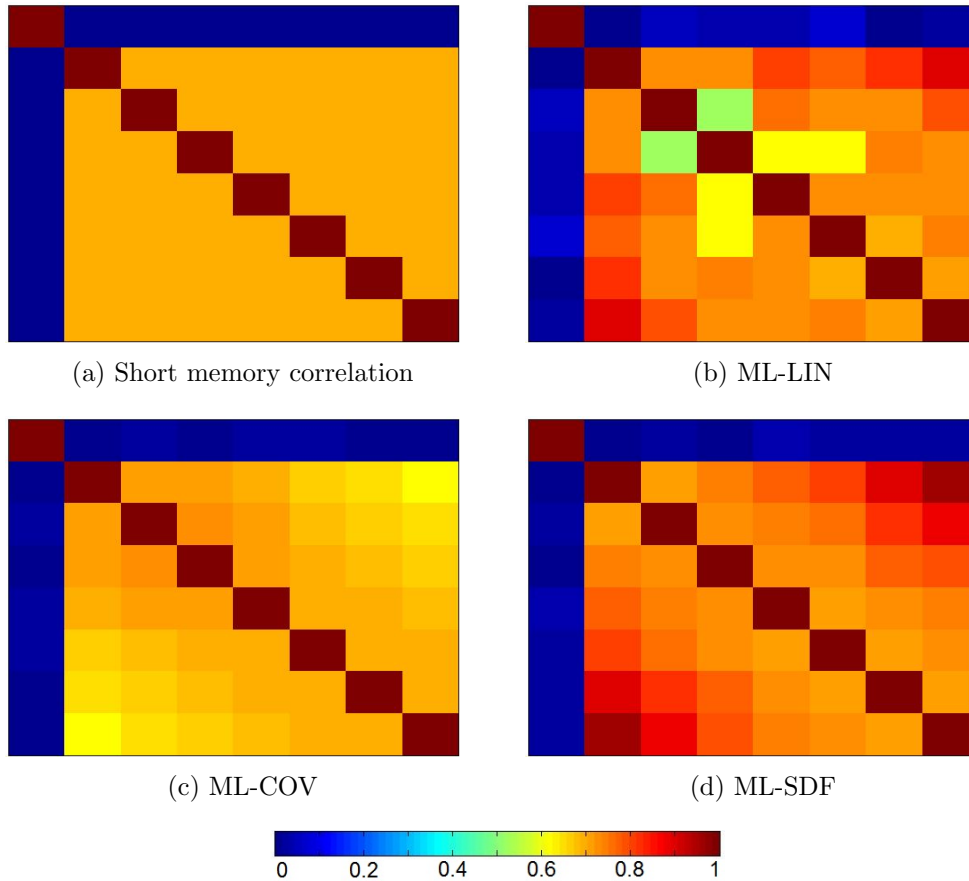
Figure 4.12: An example of nonfractal connectivity estimation in a simulated 8-dimensional ARFIMA$(0, d, 0)$ process.

COV method is more similar with the original short memory correlation matrix than others. Note that the ML-COV method is less biased than the LMS-COV method for a diversity of short memory conditions. However, the use of wavelet ML estimator is not recommended when the signal-to-noise ratio is low since it tends to be less consistent in the presence of noise contamination as discussed in Section 4.4.1.

4.5 Summary and discussion

In this chapter, a resting state BOLD signal have been modeled as an FI process on the basis of the expectation from the previous chapter such that the FI process is more appropriate for resting state BOLD signals. Although this model has been suggested for fMRI time series, it could be extensively applied for a diversity of neuroimaging data (including EEG and MEG) taken at rest. The FI process model implies that a resting state neuroimaging signal with long memory can be split into long memory and short memory components. The short memory signal is a virtual concept which does not directly represent neuronal processes. It would be valuable to empirically figure out the association between nonfractal dynamics and endogenous neuronal activities since it might provide the physical and biological basis to understand fractal behavior of brain dynamics. Based on the FI process model, a novel concept of resting state functional connectivity, called the nonfractal connectivity, has been proposed, and its properties have been clarified theoretically including the relationship with fractal connectivity.

Various wavelet-based techniques for estimating nonfractal connectivity and fractal connectivity along with memory parameter have been suggested. The estimator consists of memory parameter estimator and short memory covariance estimator as depicted in Figure 4.5. The multivariate WLMS estimator was proposed to estimate memory parameters in a multivariate manner as an extension of the bivariate WLMS method first proposed in Achard et al. (2008). It is concluded, from the simulation studies, that this advanced estimator can be chosen as a best estimator of memory parameters as long as the BOLD signals are greatly noisy. In the next step, several wavelet-based estimators has been evaluated through simulation studies. The estimation of short memory covariance is highly influenced by the short memory condition and the number of time series. It suggests that the choice of estimators should be carefully determined according to the individual properties of neuroimaging data.

Chapter 5

Applications

5.1 Introduction

The functional connectivity analysis of resting state neuroimaging signals is more intricate than task-based analysis of the brain since a resting state signal tends to be easily perturbed by physiological factors and noises while it has no reference signal such as stimulation to be regressed. It has been proposed in Section 3.5 that the fractal behavior triggered by cerebral hemodynamic activities is one of sources perturbing functional connectivity of resting state brain signals. The novel concepts of nonfractal connectivity and fractal connectivity as well as the wavelet-based estimation techniques have been proposed in Chapter 4 to overcome the fractal-driven connectivity distortion. This chapter introduces examples of fractal-based analysis for resting state functional connectivity in both human brain and animal brain. In Section 5.2 depressed patients are compared with normal persons in terms of network properties of the brain produced through the fractal-based connectivity analysis. In Section 5.3 the rat brains are studied by comparing the network properties before training the rat with those after training. All experimental results demonstrate that the fractal-based analysis provides detailed and extraordinary information on functional connectivity which cannot be identified by Pearson correlation.

5.2 Fractal-based analysis of the human brain

A possible application of fractal-based connectivity analysis is to provide information instrumental for diagnosis of diseases. An an example, the major depressive disorder (MDD) is one of complicated diseases on which doctors are hard to make a correct diagnosis (Pérez-Stable et al., 1990). A number of psychiatric researches have focused on analyzing resting state functional connectivity of neuroimaging data taken from the MDD patients at rest (Bluhm et al., 2009; Greicius, 2008; Greicius et al., 2007; Sheline et al., 2009). Recently, a study on network properties of resting state functional connectivity found a substantial difference in community structure of the brain network between healthy subjects and MDD patients (Lord et al., 2012). They computed the Pearson correlation, and then applied the distance penalization to the functional connectivity graphs to eliminate the non-neuronal effect of distance between regions on reduction of correlation (Salvador et al., 2005). A significant shift of the participation index (PI) (see Section 2.4) from healthy subjects to MDD patients was found in 29 regions from the distance-penalized network. Such a shift of PI, however, was not found in the original networks where the distance penalization was not applied. Moreover, it is not clear whether such a trend of PI shift is consistent over a range of thresholds for connectivity sparsity. In this section, it is shown that either nonfractal connectivity or fractal connectivity are beneficial to reveal the change in node strength from healthy subjects to MDD patients, and that this change is consistently observed over a range of thresholds without distance penalization.

The resting state fMRI data of twenty-one MDD patients and twenty-two healthy subjects were taken as an echo-planar imaging (EPI) sequence from a 3 Tesla scanner. The raw data with 488 time points were preprocessed, including slice time correction, motion correction, detrending, band-pass filtering (0.01 0.08Hz) and global mean removal, by using the statistical parametric mapping software (SPM5; http://www.fil.ion.ucl.ac.uk/spm) and the data processing assistant for resting-state fMRI (DPARSF; http://www.restfmri.net/forum/DPARSF) (Yan & Zang, 2010). The fMRI data was segmented into 95 ROIs of cingulate cortex and insular cortex using a variation of the automatic anatomic labeling (AAL) atlas (Tzourio-Mazoyer et al., 2002). For more specification on

the fMRI data, refer to Lord et al. (2012) that used the same data.

Three connectivity measures, such as Pearson correlation (COR), nonfractal connectivity (NFC), and fractal connectivity (FRC), were computed for each subject. The LMS-LIN estimator, consisting of the univariate WLMS estimator of memory parameter and the linearity-based estimator of short memory covariance, was used as an estimator of nonfractal connectivity and fractal connectivity (see Section 4.3.2). The minimum scale interval (MSI) and the lower scale bound (LSB) for automatic scale selection were set to be 3 and 2 respectively (see Section 4.3.1.2).

Figure 5.1 illustrates the samples of connectivity matrix. The estimators of fractal connectivity and nonfractal connectivity might be erroneous due to the short length of BOLD signals as expected in Section 4.4.2. Notice that both fractal connectivity and nonfractal connectivity have a fewer number of pairs with negative correlation than Pearson correlation has. Such a phenomenon may be caused by the pairs of regions with memory parameter higher than $1/2$; indeed, the fractal connectivity $\varrho_{m,n}$ in (4.13) has different sign with Pearson correlation $\rho_{m,n}$ if $d_m > 1/2$ and $d_n > 1/2$. Likewise, the nonfractal connectivity $\xi_{m,n}$ in (3.47) also has different sign with Pearson correlation if $d_m > 1/2$, $d_n > 1/2$ and $|d_m - d_n| < 1$. In Figure 5.1(a), 27 ROIs exhibit such a fractal behavior that $H = d + 1/2 > 1$. In the nonfractal connectivity matrix in Figure 5.1(d), a few regions exhibiting strong negative correlation with others are observed. Such an abnormal strong negative correlation may happen if $d_m > 1/2$, $d_n > 1/2$ and $|d_m - d_n| \to 1$ from (3.47).

Effects of long memory on global network properties

After yielding the connectivity matrices, both global and local network metrics were measured over a range of thresholds for connectivity sparsity (see Section 2.4 for definitions of graph theoretical metrics). Fig. 5.2 and 5.3 illustrate the comparison of fractal connectivity with nonfractal connectivity in terms of global graph metrics such as global efficiency (GE), small-worldness index (SWI), characteristic path length (CP), and clustering coefficients (CC). The distance penalization was applied before the global network metrics are produced. In Figure
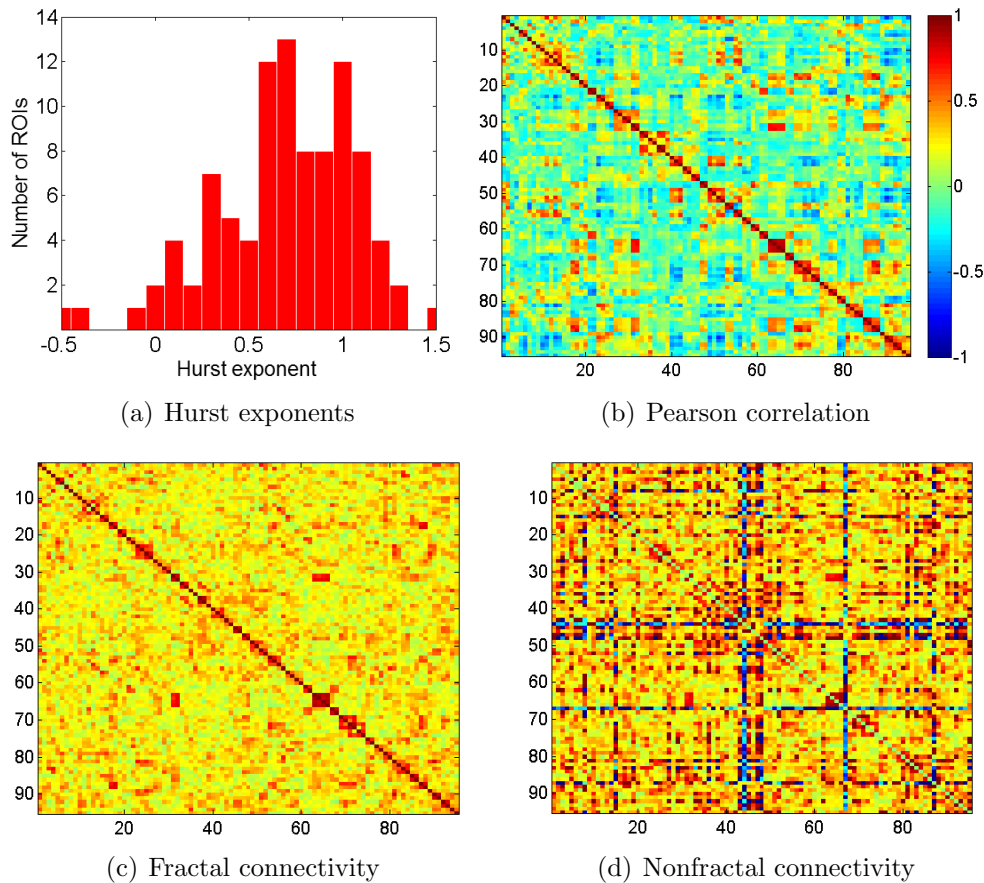
(a) Hurst exponents

(b) Pearson correlation

(c) Fractal connectivity

(d) Nonfractal connectivity

Figure 5.1: Fractal analyses of the human brain: (a) The historgram of Hurst exponents over ROIs, (b) Pearson correlation, (c) fractal connectivity, and (d) nonfractal connectivity.

5.2(a) and 5.2(b), the mean of global efficiency in both healthy subjects and MDD patients has little difference between nonfractal connectivity and fractal connectivity although GE tends to decrease in nonfractal connectivity as the threshold increases. On the other hand, the subject variance of global efficiency was significantly greater in nonfractal connectivity than fractal connectivity. In other words, the nonfractal components have less between-subject consistency of GE than the original BOLD signals have.

It is seen in Figure 5.2(c), 5.2(d), 5.3(c), 5.3(d), that both SWI and CC have lower values in nonfractal connectivity than in fractal connectivity when the threshold is small ($< 20\%$). In spite of the reduction of SWI, the nonfractal
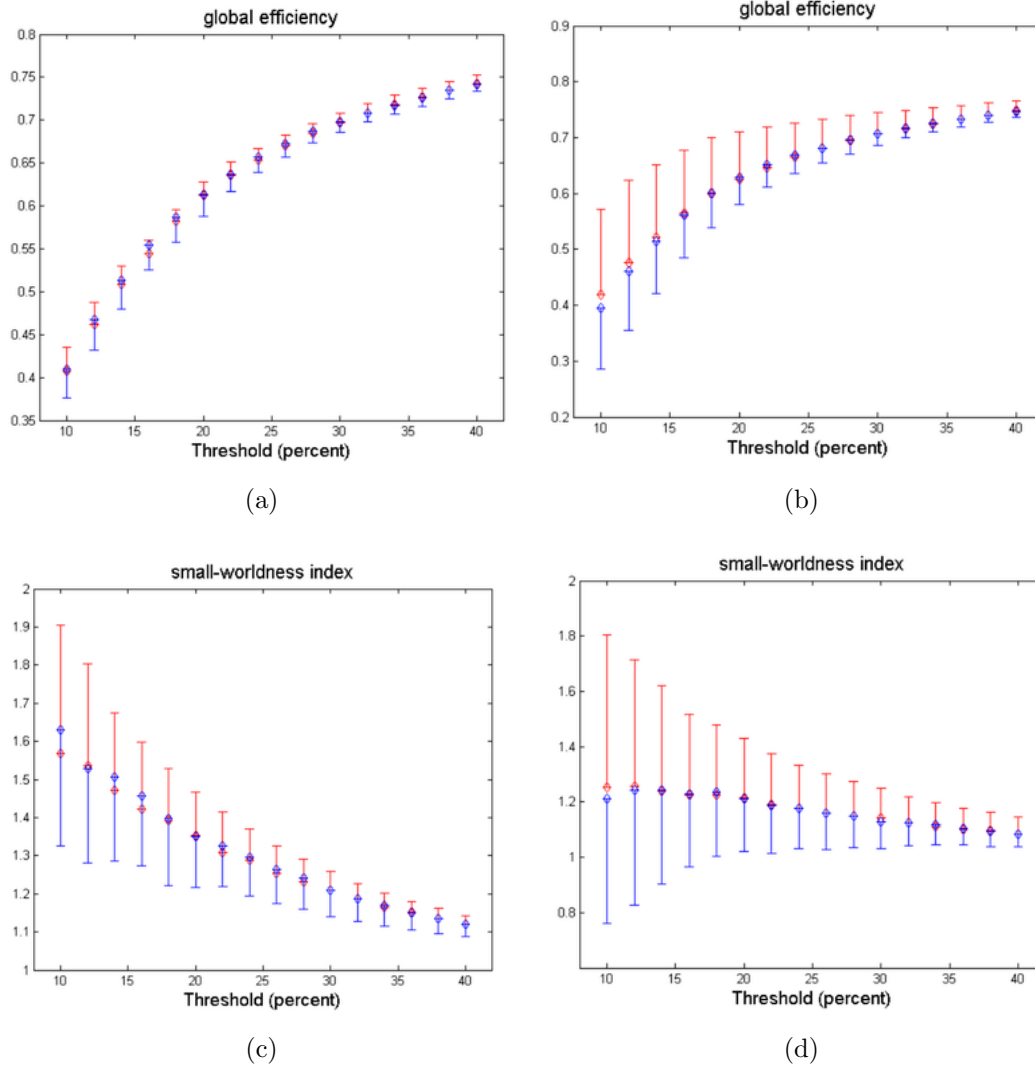
Figure 5.2: Spectrum of global efficiency and small-worldness index across thresholds for healthy subjects (red) and MDD patients (blue); (a) and (c) for fractal connectivity, (b) and (d) for nonfractal connectivity.

connectivity networks still maintain small-worldness across most thresholds; the mean SWI value is over 1 (Achard et al., 2006; Montoya & Sol, 2002; Watts & Strogatz, 1998). In addition, the small-worldness is more consistent in nonfractal connectivity over a range of thresholds than in fractal connectivity. The small-worldness is also found from the characteristic path length (CP) of both fractal connectivity and nonfractal connectivity as CP approaches to 1 as the threshold
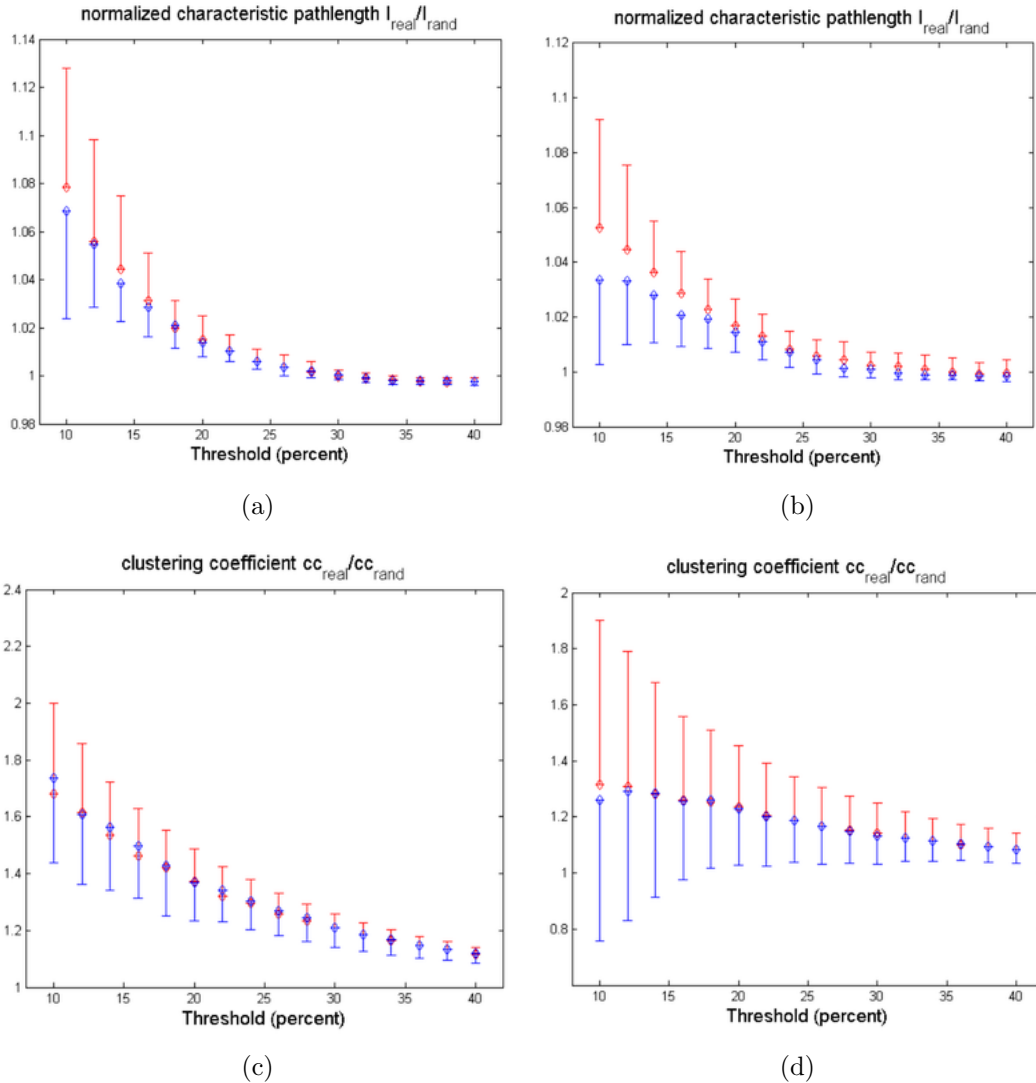
Figure 5.3: Spectrum of normalized characteristic path length and clustering coefficient across thresholds for healthy subjects (red) and MDD patients (blue); (a) and (c) for fractal connectivity, (b) and (d) for nonfractal connectivity.

increases as shown in Figure 5.3(a) and 5.3(b). Unlike other global metrics, a significant difference between healthy subjects and MDD patients is found from the trend of the mean CP of nonfractal connectivity when the threshold is small (< 20%) (see Figure 5.3(b)).

Figure 5.4 and 5.5 shows the comparison of healthy subjects with MDD patients in the global network metrics averaged over a range of thresholds. No
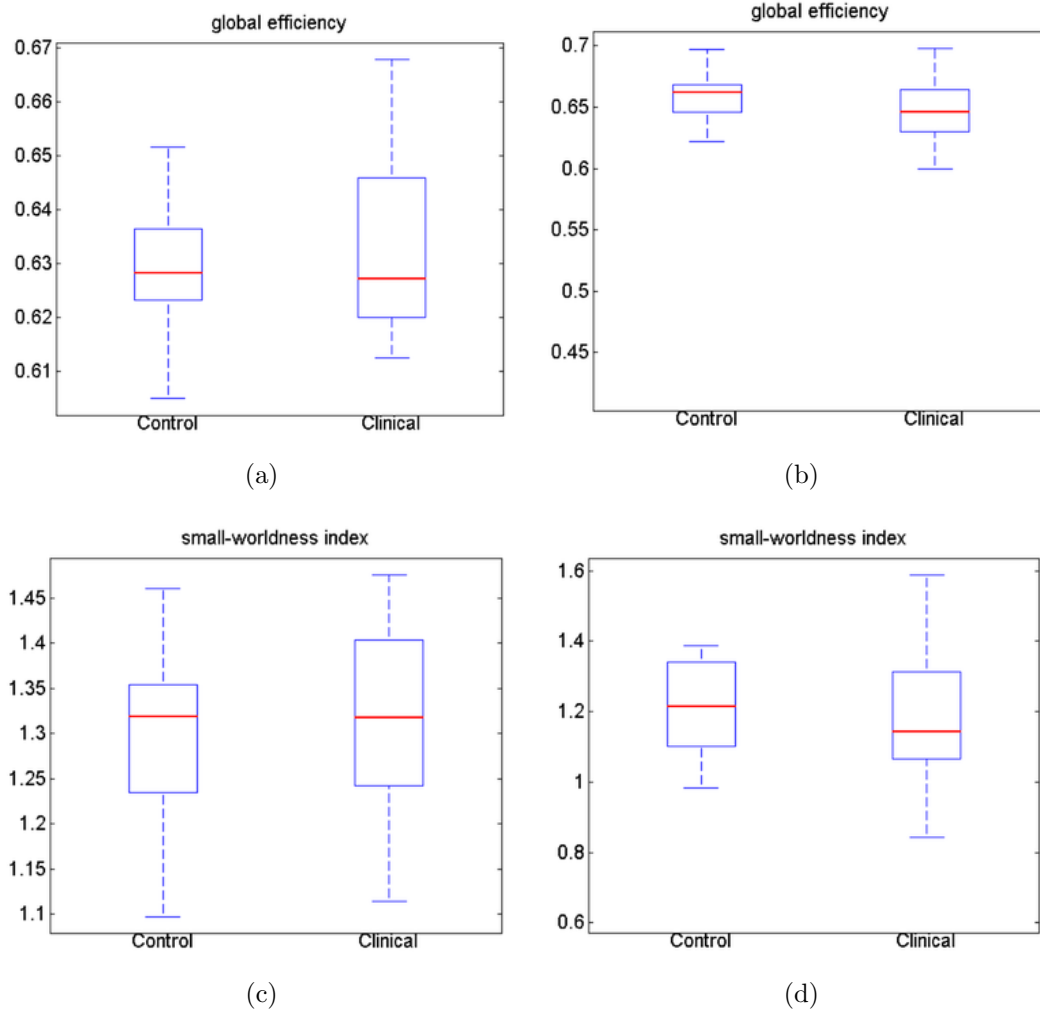
Figure 5.4: Comparison of global efficiency and small-worldness index averaged over thresholds between healthy subjects and MDD patients; (a) and (c) graph metrics in fractal connectivity, (b) and (d) those in nonfractal connectivity.

significant between-group difference in global metrics was found from both fractal connectivity and nonfractal connectivity even though the mean difference was greater in nonfractal connectivity than in fractal connectivity. It should be also noted that the subject variance was greater in nonfractal connectivity than in fractal connectivity. As a concluding remark, all these results suggest that the global network metrics are not useful to distinguish MDD patients from healthy subjects.
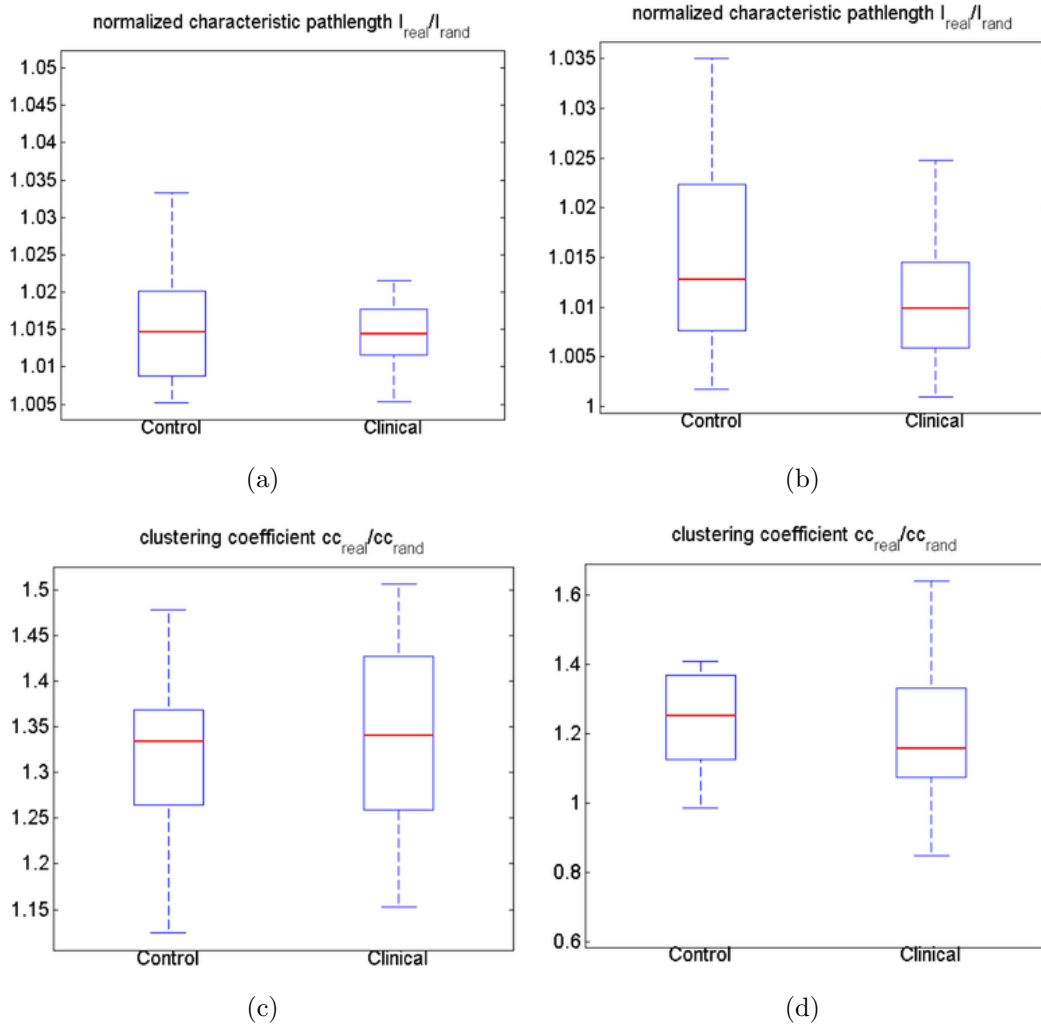
Figure 5.5: Comparison of normalized characteristic path length and clustering coefficient averaged over thresholds between healthy subjects and MDD patients; (a) and (c) graph metrics in fractal connectivity, (b) and (d) those in nonfractal connectivity.

Effects of long memory on local network properties

In addition to the global network metrics, the local network metrics were computed from fractal connectivity and nonfractal connectivity matrices, and compared with those of the Pearson correlation matrix. The two-sample t-tetst was performed for the local metrics such as local efficiency (E_{loc}), LEGE (E_{loc}/E_{glob}), participation index (PI), betweenness centrality (BCI), ranked betweenness cen-

trality (BCR), degree, modularity, path length, and strength. The distance penalization was not applied before extracting local metrics. Most local metrics except degree and strength did not exhibit a significant mean difference between healthy subjects and MDD patients. In particular a noteworthy shift between healthy subjects and MDD patients was not found even in PI of all connectivity matrices while such a substantial difference was found by Lord et al. (2012) in PI extracted from Pearson correlation of the same data. This discrepancy seems to be caused by the effect of distance penalization since the local metrics in their analysis were produced after the distance penalization, which implies that the PI is highly sensitive to the distance penalization. Therefore, the group difference in PI is disputable unless the exclusive influence of distance penalization on PI shifts are well verified through additional experiments.

While the PI had negligible group difference in all regions, degree and node-wise strength exhibited a substantial between-group difference in some regions. Figure 5.6, 5.7, 5.8, and 5.9 show the statistical comparison of node strength in three types of brain networks by depicting the distribution of mean group difference and p-values in node strength over a range of thresholds. Depicting the statistics of degree was omitted since it is almost similar with node strength. Ten brain regions, as listed in Table 5.1, were selected as the regions with the most robust group difference since they have at least one connectivity measure (among COR, NFC, and FRC) whose p-values for node strength are lower than the significance level over the range of thresholds ($\in [0.1, 0.4]$). For example, the middle horizontal line at the second column of each figure indicates the significance level $p = 0.05$; all p-values located above the line imply the rejection of the hypothesis such that healthy subjects and MDD patients have different means of node strength. In other words, the p-value can be exploited to justify a statistical hypotheses on the mean between-group difference.

As shown in Fig. 5.6(b), 5.6(f), 5.7(d), 5.7(f), and 5.8(b), there were five regions -such as ORBsupmed.R, PHG.L, CAU.R, THA.L, TPOsup.R- where node strengths extracted from nonfractal connectivity exhibited a significant mean difference between healthy subjects and MDD patients with p-values lower than the significance level. In these regions, the mean shift of node strength was greater in nonfractal connectivity than either fractal connectivity or Pearson correlation

Table 5.1: The ROIs of the human brain with significant difference in node strength between HC and MDD.

ROI name	Abbreviation	Robust Connectivity
Superior frontal gyrus, medial orbital	ORBsupmed.R	NFC
Gyrus rectus	REC.L	COR
Parahippocampal gyrus	PHG.L	NFC, FRC
Calcarine fissure and surrounding cortex	CAL.L	FRC
Caudate nucleus	CAU.R	NFC
Thalamus	THA.L	NFC
Temporal pole: superior temporal gyrus	TPOsup.R	NFC
Temporal pole: middle temporal gyrus	TPOmid.R	FRC
Anterior MCC	anterior MCC	COR
PCC-Spectro	PCC-Spectro	FRC

as shown in the first column of Figure 5.6(a), 5.6(e), 5.7(c), 5.7(e), and 5.8(a). On the other hand, the other four regions -such as PHG.L, CAL.L, TPOmid.R, and PCC-Spectro- showed significant group difference in node strength of fractal connectivity as shown in Figure 5.6(f), 5.7(b), 5.8(d), and 5.9(b). In these reasons, the node strengths of fractal connectivity may be more beneficial than those of either nonfractal connectivity or Pearson correlation to reveal the group difference between healthy subjects and MDD patients. There were two brain regions -such as REC.L and anterior MCC- that exhibited significant between-group difference in node strength of Pearson correlation as shown in Figure 5.6(d) and 5.8(f).

The mean group difference of node strength in the first columns of Figure 5.6, 5.7, 5.8, and 5.9 also have essential implication on neurodynamics; the gap of group differences between nonfractal connectivity and fractal connectivity may originate from the heterogeneity of fractal behaviors among the connected neighbors. On the contrary, the small gap of group differences in node strength between nonfractal connectivity and fractal connectivity can be interpreted as the implication such that the brain region has relatively homogeneous fractal properties over connected neighbors. According to this interpretation, the five regions -such as ORBsupmed.R, CAU.R, THA.L, TPOsup.R, PCC-Spectro- have relatively heterogeneous fractal behaviors with neighbors while the other five regions -such as REC.L, PHG.L, CAL.L, TPOmid.R, anterior MCC- have more homogeneous

(a) ORBsupmed.R

(b) ORBsupmed.R
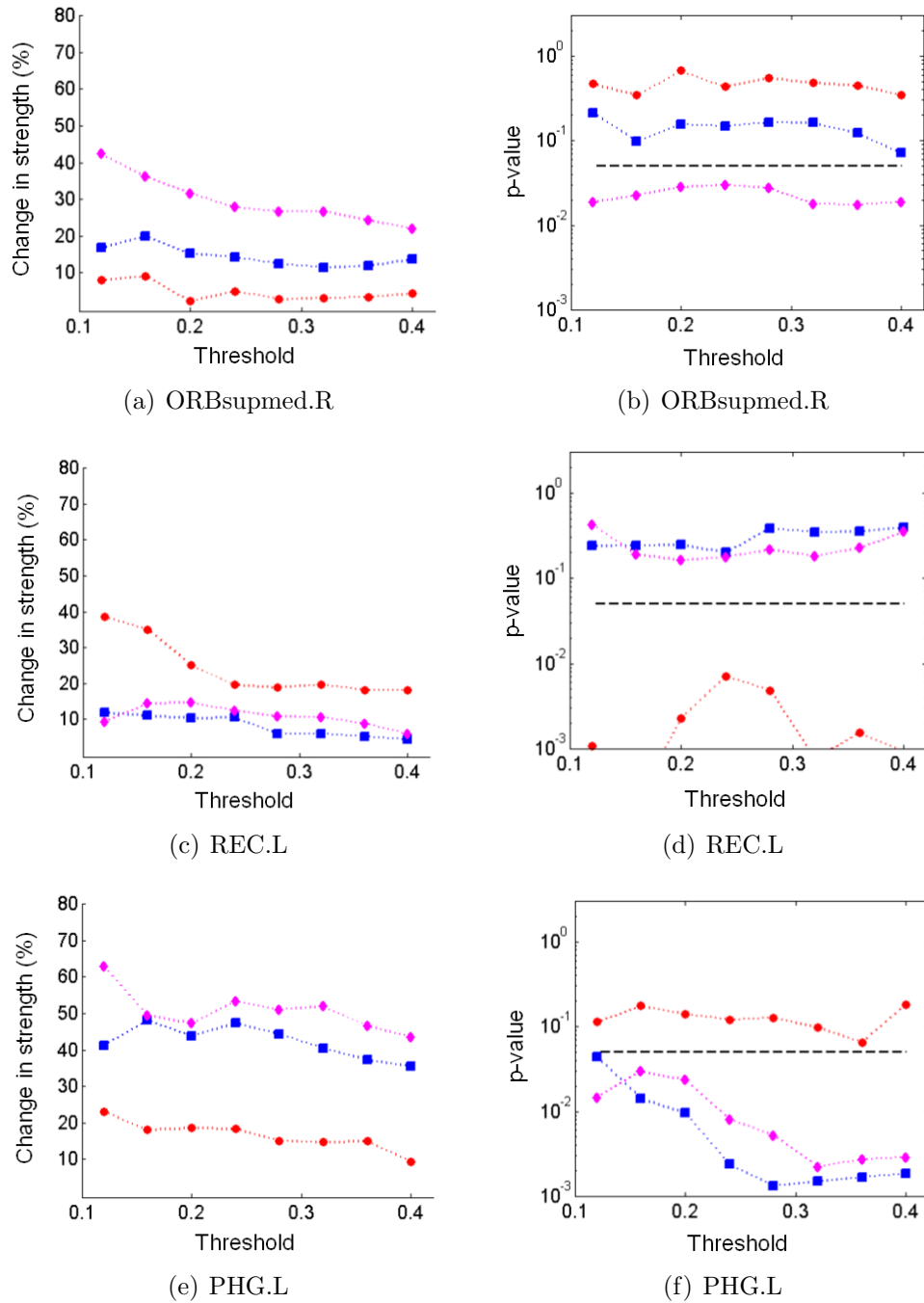
(c) REC.L

(d) REC.L

(e) PHG.L

(f) PHG.L

Figure 5.6: The t-test statistics of node strength in Pearson correlation (*circle*), non-fractal connectivity (*diamond*), and fractal connectivity (*rectangle*) for such brain regions as ORBsupmed.R, REC.L, and PHG.L.
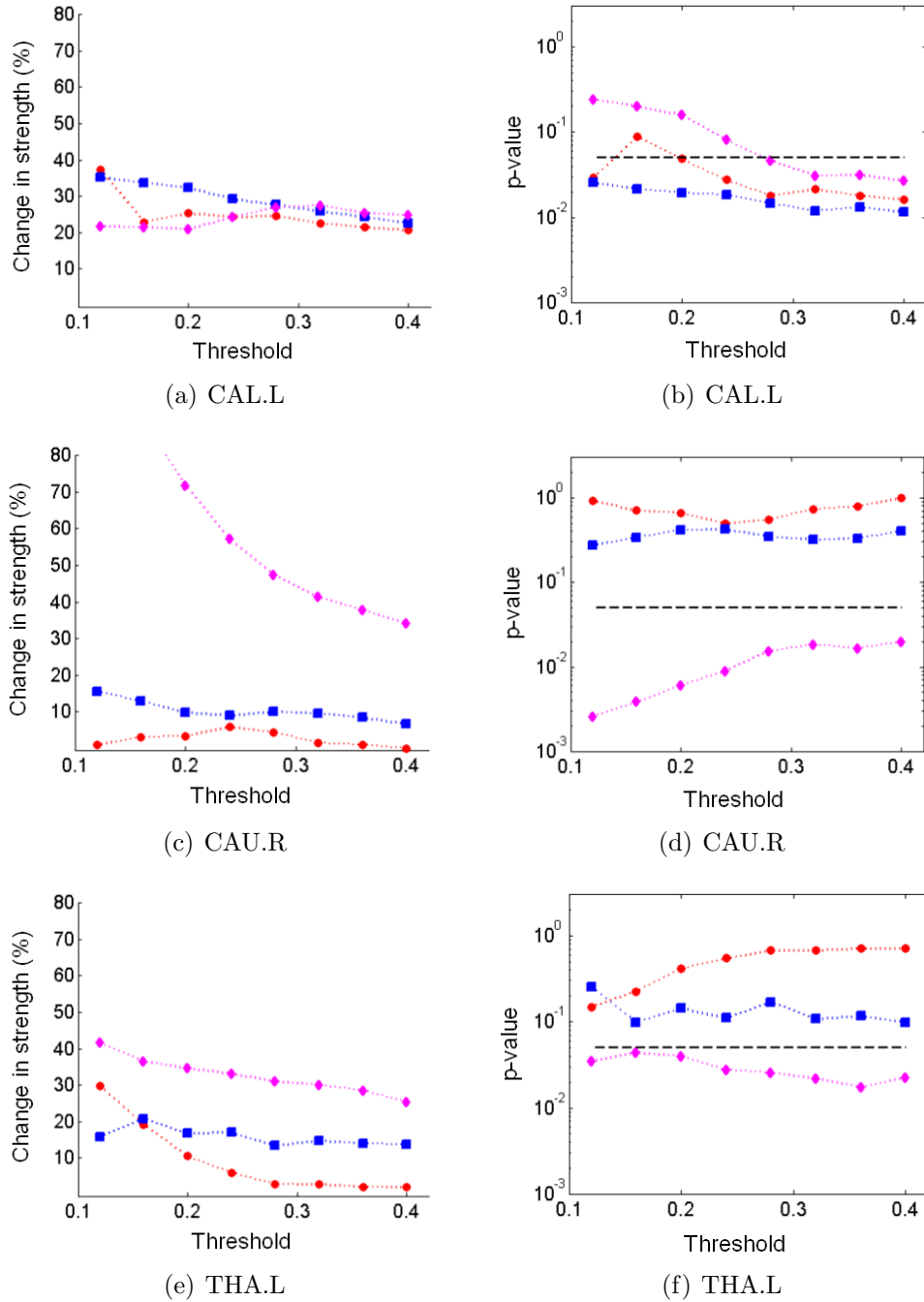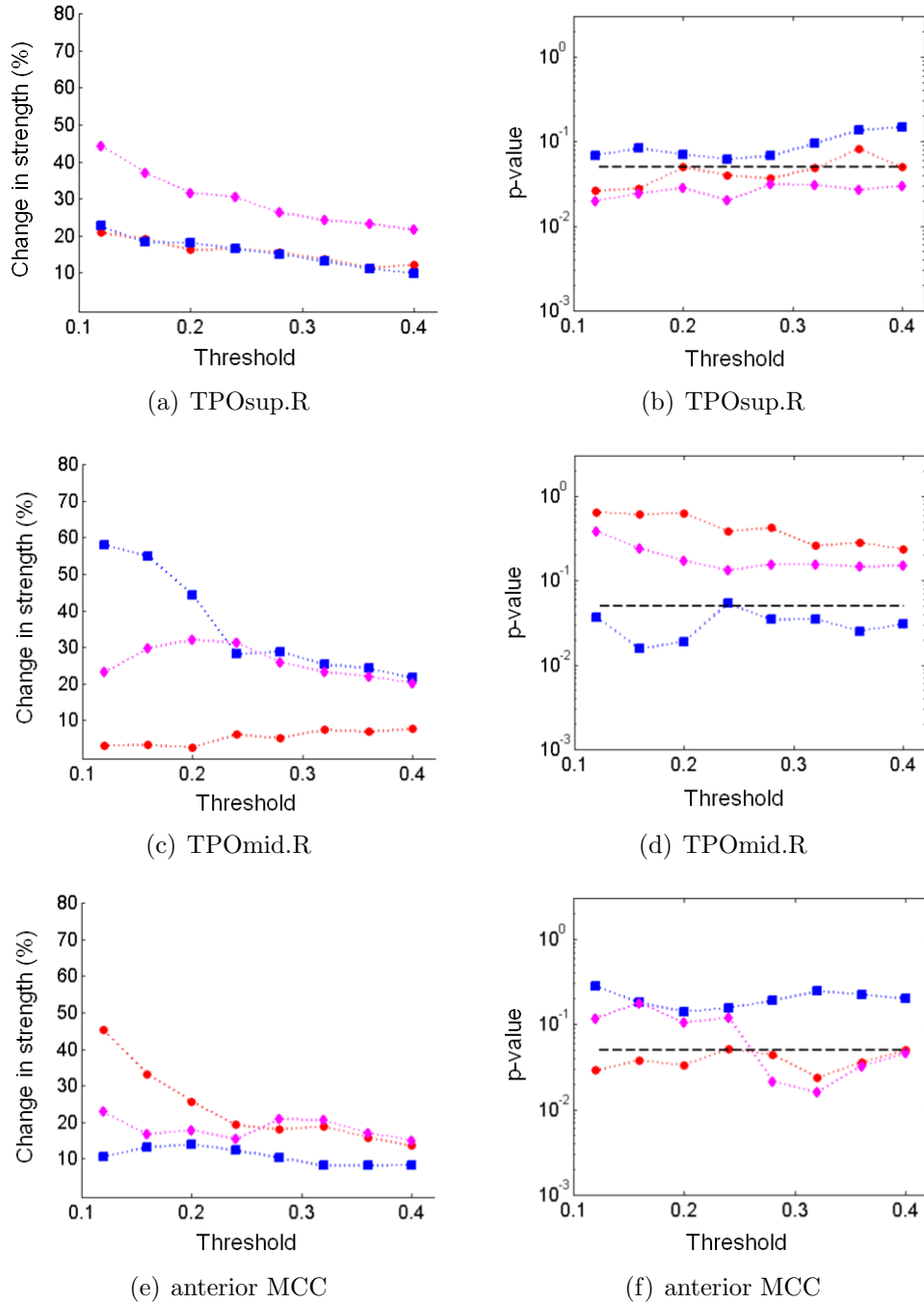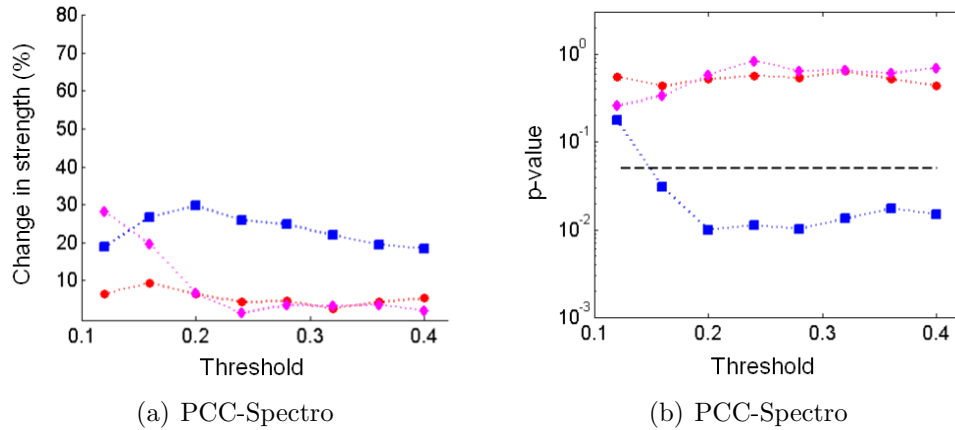
Figure 5.7: The t-test statistics of node strength in Pearson correlation (*circle*), non-fractal connectivity (*diamond*), and fractal connectivity (*rectangle*) for such brain regions as CAL.L, CAU.R, and THA.L.

(a) TPOsup.R

(b) TPOsup.R

(c) TPOmid.R

(d) TPOmid.R

(e) anterior MCC

(f) anterior MCC

Figure 5.8: The t-test statistics of node strength in Pearson correlation (*circle*), non-fractal connectivity (*diamond*), and fractal connectivity (*rectangle*) for such brain regions as TPOsup.R, TPOmid.R, and anterior MCC.

(a) PCC-Spectro (b) PCC-Spectro

Figure 5.9: The t-test statistics of node strength in Pearson correlation (*circle*), nonfractal connectivity (*diamond*), and fractal connectivity (*rectangle*) for the PCC-Spectro region.

fractal behaviors.

In conclusion, all of these experimental results for local network metrics demonstrate that both fractal connectivity and nonfractal connectivity are useful as the essential features of brain networks which reveal the between-group difference. Indeed, the nonfractal connectivity and fractal connectivity were more frequently chosen as the featured measure of functional connectivity than Pearson correlation as listed in Table 5.1.

5.3 Fractal-based analysis of the rat brain

The fractal-based connectivity analysis is instrumental for studies of animal brains even though most fractal analyses have focused on the human brain (Herman et al., 2011). This section introduces an application of the fractal-based connectivity analysis techniques proposed in Chapter 4 to the rat brain. The aim of this study is to figure out the effect of stimulation on resting state functional connectivity by observing the change in functional connectivity triggered by external stimulation as depicted in Figure 5.10(a).

Three 7-8 weeks old male Wistar rat were anesthetized with Nembutal (40 mg/kg i.p.) and underwent a standard surgical procedure to implant a bipolar stimula-
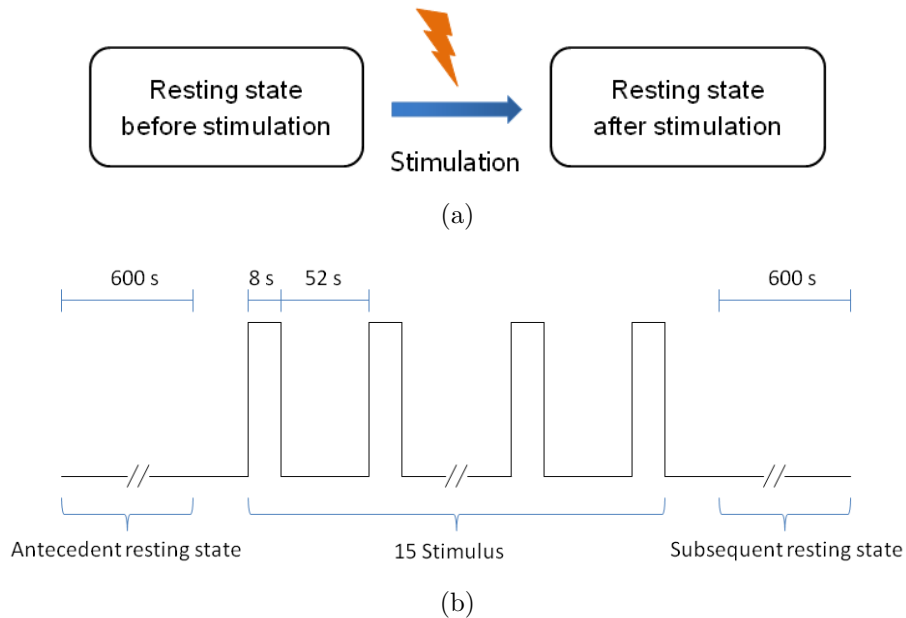
Figure 5.10: The experimental paradigm of resting state fMRI in the rat brain: (a) the summarized experimental process and (b) the stimulus details.

tion electrode. To avoid motion artifacts during fMRI data acquisition, the rats were initially anesthetized with 1.0-1.5% isoflurane (in 50:50 N_2O:O_2; v/v) and after this the narcosis was sedated by medetomidine (100 μg/kg body). The fMRI data was taken on a Bruker Biospec 47/20 4.7T scanner by using an echoplanar imaging (EPI) sequence with the environmental parameters: TR=1 s (TR=2 s during stimulation), TE=24 ms, slice thickness=1 mm, FOV=40 $\times$ 40 mm, matrix=64 $\times$ 64, 8 slices. The stimulation was given with a general block design; an fMRI data was first acquired during 600 s at rest, and then a 10 Hz stimulus train of 8 s (whose intensity is set to be a half of the maximum amplitude for evoked population spikes) was assigned every minute during 15 minutes (see Figure 5.10(b)). After the 15 times stimulus, the subsequent resting state fMRI data was acquired during 600 s. Eight horizontal T_2-weighted spin-echo images were taken as the anatomical image template by using a rapid acquisition relaxation enhanced (RARE) sequence with the parameters: repetition time (TR)=4 s, echo time (TE)=15 ms, slice thickness=1 ms, field of view (FOV)=40 $\times$ 40 mm, matrix=256 $\times$ 256, RARE factor=8, number of averages=4 (Hennig et al., 1986).

Table 5.2: The list of parcellated regions in the rat brain.

ROI name	Abbreviation
Anterior cingulate cortex	aCG
Caudate putamen (striatum), left	CPu-L
Caudate putamen (striatum), right	CPu-R
Medial entorhinal cortex, left	MEnt+MEntV-L
Medial entorhinal cortex, right	MEnt+MEntV-R
Hippocampus, left	HIP-L
Hippocampus, right	HIP-R
Primary somatosensory cortex, left	S1-L
Primary somatosensory cortex, right	S1-R
Secondary somatosensory cortex, left	S2-L
Secondary somatosensory cortex, right	S2-R
Septum: Lateral septal nucleus intermediate part, Medial septal nucleus	LSI+MS
Tectum, left	TE-L
Tectum, right	TE-R
Thalamus	TH

As listed in Table 5.2, the ROIs were manually parcellated from the anatomical images using the FMRIB Software Library (FSL) (Jenkinson et al., 2012), and were co-registered with the fMRI volumes on the basis of the affine model of 12 degrees of freedom using the FMRIB linear image registration tool (FLIRT) (see Figure 5.11; see Paxinos & Watson, 2007 for the anatomical structure of the rat brain, and Jenkinson & Smith, 2001 for FLIRT).

The functional data in each ROI were averaged into a time series, and preprocessed through removing linear trends; such additional steps as slice scan time correction and band-pass filtering were not applied. From the averaged BOLD sequences, three connectivity metrics, such as Pearson correlation, fractal connectivity, and nonfractal connectivity, were calculated for all possible pairs of ROIs. Both the LMS-LIN and ML-LIN estimators were exploited to estimate fractal connectivity and nonfractal connectivity respectively (see Section 4.3.2). The minimum scale interval (MSI) and the lower scale bound (LSB) for automatic scale selection were assigned to be 4 and 1 respectively (see Section 4.3.1.2).

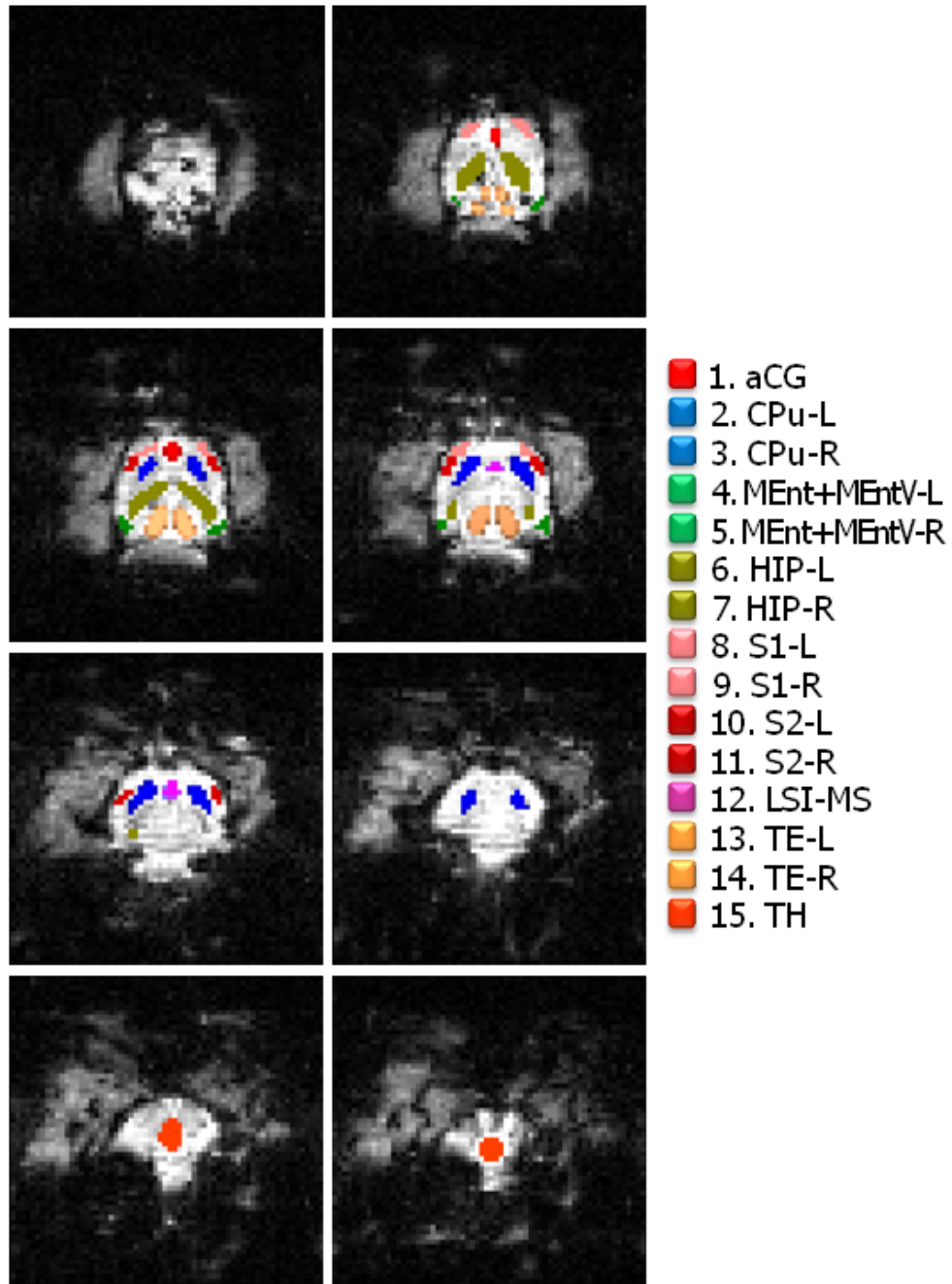The scale-dependent correlation matrices were calculated based on the wavelet

Figure 5.11: The location of fifteen ROIs in fMRI slices of the rat brain.

transform, and were exploited to estimate the Hurst exponents by the WLMS estimator. Figure 5.12(a) shows the distribution of wavelet-based LMS residuals (4.24) over all possible scale intervals. In this case, the scale interval $\mathcal{J} = [4, 6]$ with the smallest LMS residual are determined as the optimal scale interval according to the criteria (4.27). Figure 5.12(b) illustrates the voxel-wise spatial distribution of Hurst exponents in a slice. It seems that the Hurst exponents are higher in the vicinity of hippocampus, and these area with high Hurst exponent have greater long-range dependence or persistence over time.

Based on the estimated Hurst exponents, the fractal connectivity matrix for voxel-wise pairs was computed for the fMRI data taken before stimulation (see Section 4.3.2). Figure 5.12(c) shows a special Y-type pattern of voxels which have strong fractal connectivity. The set of voxels exhibiting such a spatial pattern of prominently fractal-connected neighbors tend to be located inside the Y-type pathway connecting anterior cingulate cortex (aCG), hippocampus (HIP), and medial entorhinal cortex (MEnt+MEntV) (see Figure 5.12(d)).

Along with fractal connectivity, nonfractal connectivity was also computed for both pre-stimulation fMRI data and post-stimulation fMRI data, and compared with Pearson correlation as shown in Figure 5.13. A significant rearrangement of correlation pattern in Pearson correlation was driven by stimulation after stimulation. On the other hand, there were no significant change in nonfractal connectivity between pre-stimulation resting state and post-stimulation resting state. This fact is also demonstrated in Figure 5.15 which shows the comparison of Pearson correlation and nonfractal connectivity in the mean difference between pre-stimulation and post-stimulation resting state over all pairs of ROIs. The mean shift after stimulation was greater in Pearson correlation than in nonfractal connectivity.

The difference between Pearson correlation and nonfractal connectivity is revealed more saliently when the functional connectivity are represented as graphs with threshold 0.2. In Figure 5.14, most functional connections formed before stimulation were disconnected due to stimulation. On the other hand, the nonfractal connectivity network has fewer connections than Pearson correlation, but most connections were not entangled by stimulation. Reciprocal connections in the Primary and secondary somatosensory cortices (including S1-L, S1-R, S2-
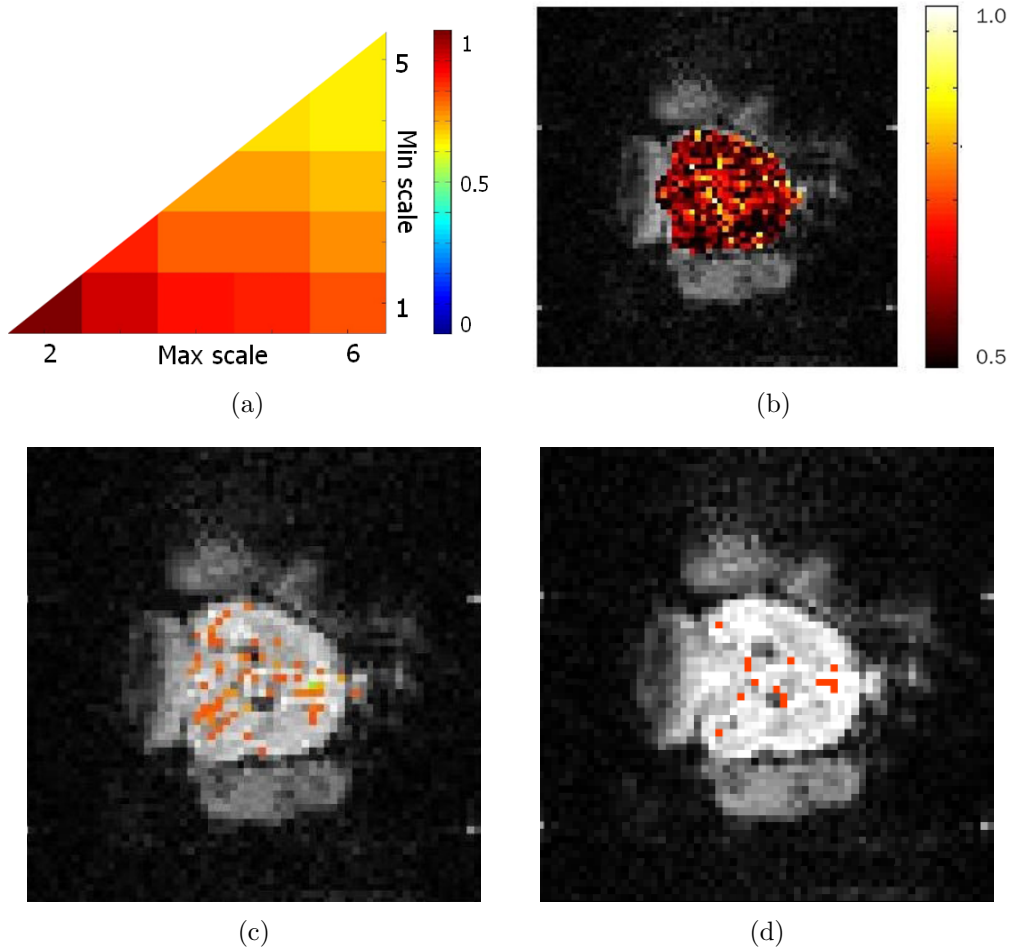
Figure 5.12: Fractal analyses of the rat brain: (a) Relative LMS residuals of the estimator over all possible scale ranges, (b) the distribution of Hurst exponents, (c) the Y-type pattern of voxels with high asymptotic wavelet correlation, and (d) the set of voxels whose asymptotically correlated neighbors are distributed in such an Y-type pattern.

L, and S2-R) were preserved in the nonfractal connectivity network regardless of stimulation. The modularity seems to be more immune to external tasks in nonfractal connectivity. Moreover, a strong interaction between left and right hemispheres in these areas were found from the nonfractal connectivity networks. This symmetric interaction was enhanced and activated after stimulation while the symmetry vanished in Pearson correlation (see Figure 5.16). The symmetry between left and right hemispheres was also found in tectum (TE-L, TE-R)
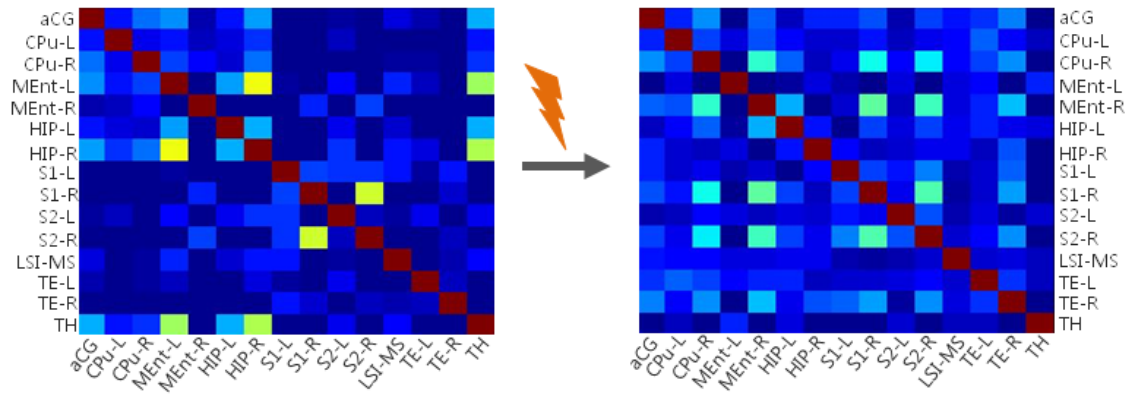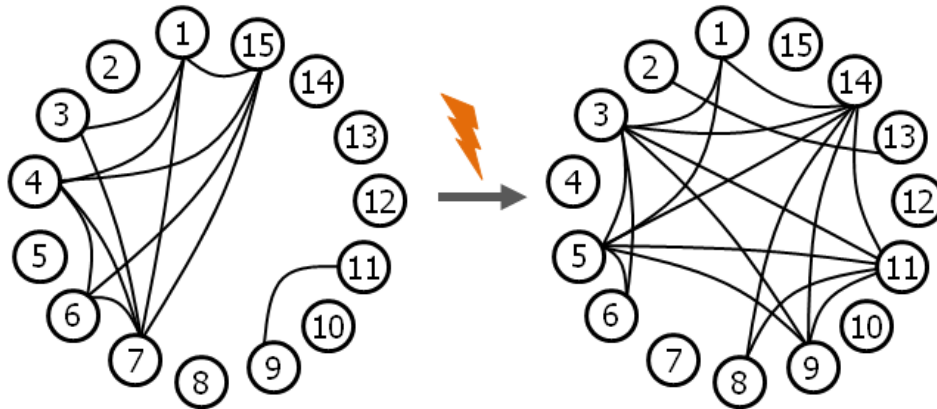
(a) Pearson correlation
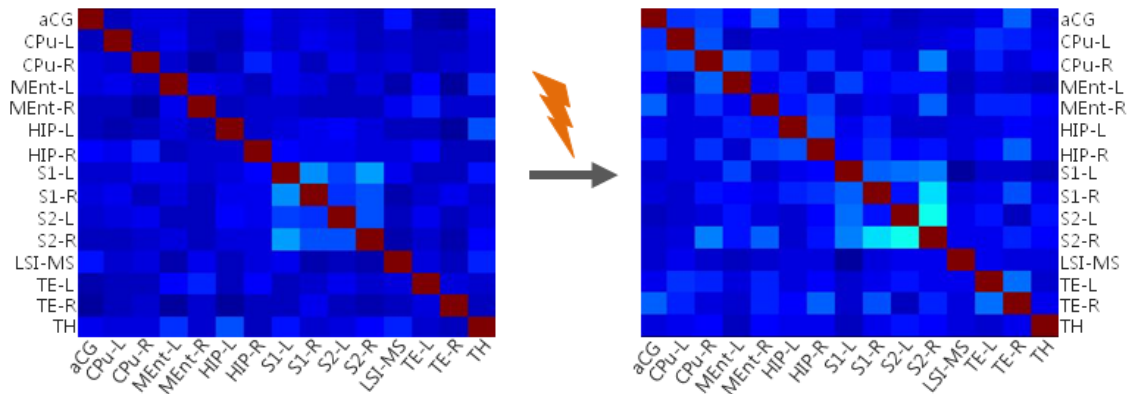
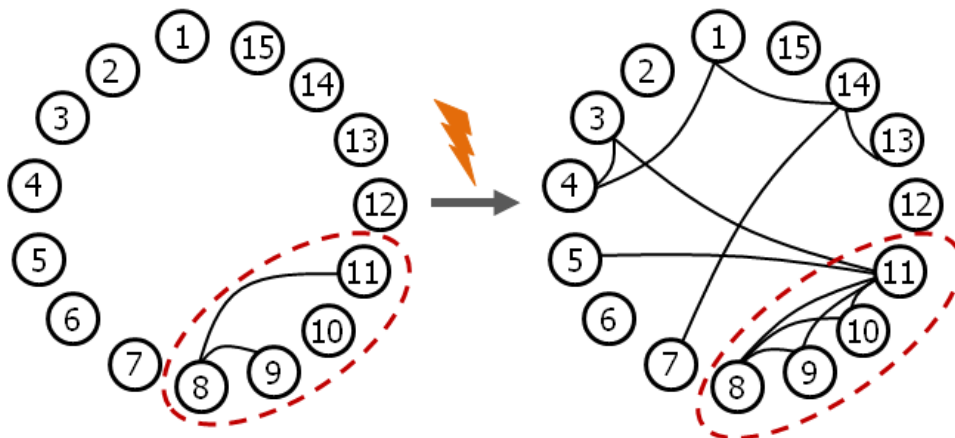
(b) Nonfractal connectivity
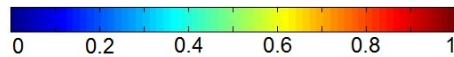
(c)

Figure 5.13: Comparison of Pearson correlation and nonfractal connectivity.

after stimulation. The other noticeable connection is the strong nonfractal connectivity between anterior cingulate cortex (aCG) and medial entorhinal cortex (MEnt+MEntV-L) since this connection has been frequently found through task-based correlation studies (Schwarz et al., 2008).

(a) Pearson correlation

(b) Nonfractal connectivity

Figure 5.14: Graph visualization of Pearson correlation and nonfractal connectivity. The threshold was set to be 0.2.

5.4 Summary and discussion

In this chapter, two applications of fractal-based connectivity analysis techniques on human and animal brains have been introduced. In these experiments, fractal connectivity and nonfractal connectivity were exploited to reveal either difference or consistency between two distinct groups of resting state BOLD signals. For the analysis of human brain, both fractal connectivity and nonfractal connectivity were effective to reveal the group difference between healthy persons and

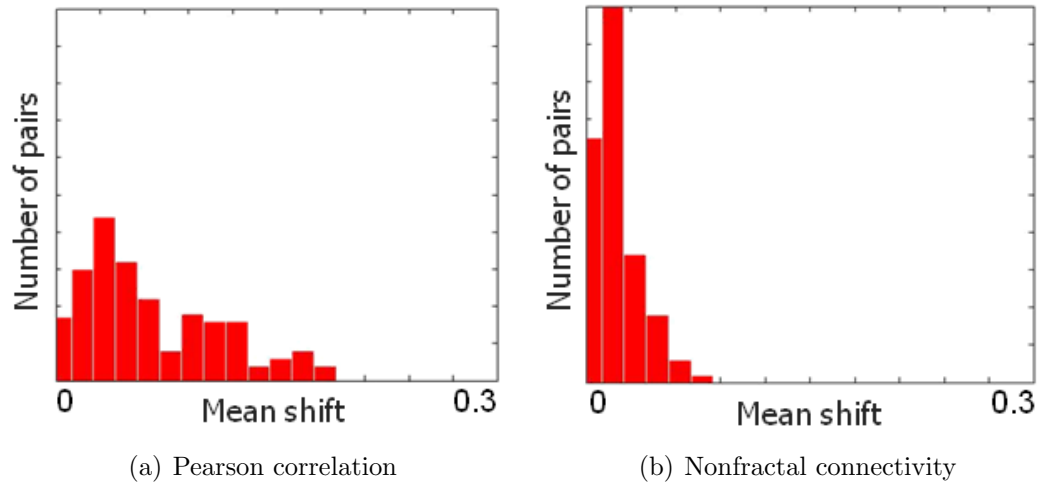(a) Pearson correlation   (b) Nonfractal connectivity

Figure 5.15: Histograms of mean differences in Pearson correlation and nonfractal connectivity between prior-stimulation and post-stimulation.
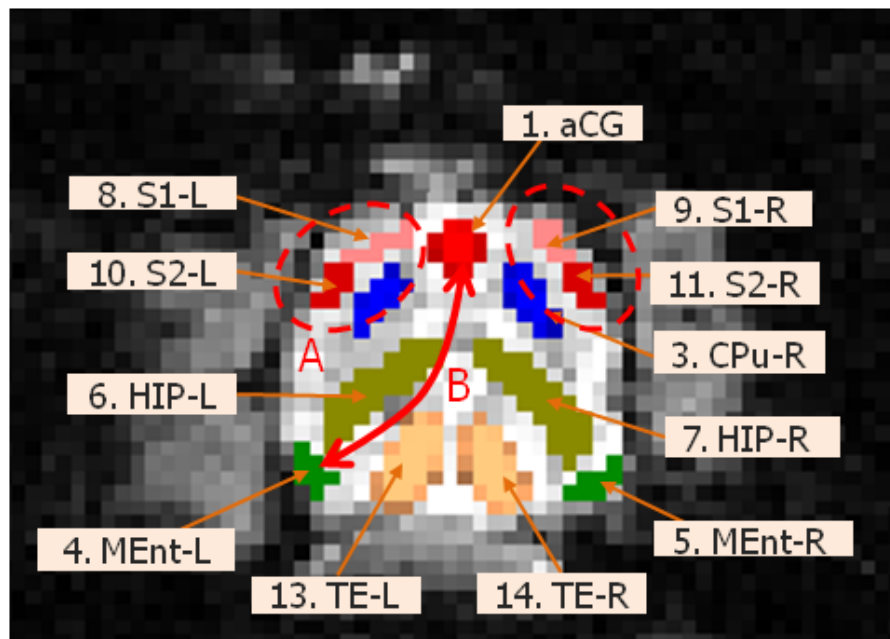

Figure 5.16: Nonfractal connectivity analyses of the rat brain.

depressive patients in such local network metrics as degree and node strength. Although the most robust connectivity metric differed according to brain regions, there were more brain regions that exhibit a significant between-group difference

in both fractal connectivity and nonfractal connectivity than in Pearson correlation. These results indicate that the fractal-based connectivity analysis may be instrumental to detect the changes in the local properties of brain networks. In the rat brain analysis, it was found that a group of strongly fractal-connected voxels were spatially distributed with the Y-type pathway which has been frequently observed in task-based fMRI data analyses. Furthermore, modularity and network symmetry between left and right hemispheres were enhanced in nonfractal connectivity than in fractal connectivity. From these results, it can be expected that the endogenous functional interactions among neuronal processes tend to be well revealed through fractal connectivity and nonfractal connectivity than Pearson correlation.

Chapter 6

Summary and Conclusion

Summary

In this thesis, a novel long memory model of resting state fMRI as well as fractal-based approaches to resting state functional connectivity have been presented. In Chapter 3, the long memory linear model of hemodynamic response has been proposed to describe the physical mechanism of long memory phenomenon driven by cerebral hemodynamic activity in terms of hemodynamic response function (HRF). While the evoked state HRF is composed of just two basis functions, the critical state HRF comprises a large number of basis functions whose coefficients are slowly decaying with a special rate. It has been shown that the BOLD signal exhibits long memory when the HRF is at the critical state. It was also argued, through the Volterra series expansion, that the nonlinearity of hemodynamic activities has little impacts on long memory property. The fact that different states of the impulse hemodynamic response are present implies that the shape of HRF may alter according to the history of neuronal activities. This property was named the history dependence excitability (HDE) of hemodynamic response.

The long memory model of hemodynamic response provides important inference on the effect of fractal behavior on functional connectivity. First of all, it suggests that the fractionally integrated (FI) process is a more suitable model for resting state BOLD signals than the fractional Gaussian noise (FGN). According to the theory of FI processes, the long memory property of hemodynamic activities may induce the distortion of functional connectivity; in other words, the

discrepancy of correlation of BOLD signals from correlation of neuronal activities increases as the difference of fractal behaviors between brain regions becomes larger. In this reason, the hemodynamic fractal behavior may act as an artifact disturbing functional connectivity analyses. In addition, it was demonstrated that the influence of long memory on directional information flow is much significant; the discrepancy of transfer entropy in BOLD signals and transfer entropy in the underlying neuronal activities was considerably sensitive to the heterogeneity of fractal behaviors.

The FI process model suggests that a resting state BOLD signal with long memory can be divided into long memory and short memory components. In Chapter 4, nonfractal connectivity has been defined as the correlation of nonfractal components. Although nonfractal connectivity between BOLD signals is not identical to the correlation of the underlying neuronal activities, it may give better information on functional dynamics of spontaneous neuronal activities than Pearson correlation since the fractal artifact is effectively suppressed. The nonfractal connectivity can be regarded as a concept contrary to fractal connectivity which is based on the asymptotic property of wavelet correlations. Various wavelet-based estimators of both nonfractal connectivity and fractal connectivity have been developed and evaluated through simulation studies. In addition, a multivariate wavelet-based LMS estimator has been proposed to improve the performance of estimating the memory parameter in the presence of perturbation by additive noise.

Chapter 5 showed how both nonfractal connectivity and fractal connectivity can be applied for resting state fMRI analyses of human and animal brains. In the human brain analysis, these fractal-based metrics were efficacious in emphasizing the group difference between healthy subjects and depressive patients. In the rat brain analysis, these fractal-based metrics were used to reveal consistent patterns (such as modularity) between pre-stimulation and post-stimulation. All of experimental results suggest that the fractal-based metrics are efficacious in emphasizing not only the group difference but also consistent patterns between two distinct classes of subjects.

Conclusion and future works

The long memory model of resting state fMRI introduced in Chapter 3 can be understood as an extension of the conventional linear hemodynamic model. Hence, it enables us to figure out not only how the fractal behavior in BOLD signals can be associated with the property of hemodynamic system, but also how the fractal property of hemodynamics affects the correlation of statistical attributes between neuronal activities and BOLD signals. In evoked states, the prominent deterministic change in neuronal activities induced by stimulation suppresses the effect of $1/f$ noise, and makes the correlation between BOLD signals more analogous with that of the corresponding neuronal activities. On the other hand, the influence of fractal property on resting state BOLD signals is relatively elevated and provokes a serious change in functional connectivity depending on the heterogeneity of fractal behaviors among regions.

The long memory model leads us to hypothesize the history dependent excitability (HDE) of hemodynamic response such that the shape of hemodynamic response may be dependent on the history of past neuronal activities. In the future work, this hypothesis needs to be verified through empirical studies; for example, the HDE could be detected not only by observing the change in resting state BOLD responses according to different neuronal activities through simultaneous measurement of BOLD signals and neuronal activities, but also by measuring the Hurst exponents of hemodynamic activities through optical imaging. This challenge would be instrumental to clarify whether the hemodynamics is the most influential factor for fractal behavior of BOLD signals.

One of expectations regarding the HDE is that a hemodynamic system with long memory properties is associated with self-organized criticality (SOC). Indeed, it was shown that the power-law distribution of an $1/f$ noise reflects self-organized criticality (Bak et al., 1987). Therefore, the frequent appearance of long memory in resting state BOLD signals implies that a resting state BOLD signal tends to be at the vicinity of critical state. One of the prospective future works is to quantify the HDE and develop a method of measuring its temporal evolution in terms of SOC. In addition, the SOC can spatially appear in a brain network while the critical state of the hemodynamic system is defined for

a single process (Beggs & Plenz, 2003; Bullmore et al., 2009; Kitzbichler et al., 2009; Tagliazucchi et al., 2012). Hence, it is necessary to identify the relationship of temporal SOC and spatial SOC theoretically and empirically since it would clarify the dependence of global SOC on fractal behavior of BOLD signals.

Note that this long memory model deals with the fractal behavior caused by hemodynamic activities. On the other hand, the nonfractal connectivity in Chapter 4 has been suggested in overall consideration of all fractal sources. To be precise, the nonfractal component of a resting state BOLD signal is an abstract signal which is not physically present and is not exactly identical to the corresponding neuronal activity. Nevertheless, it is expected that the nonfractal connectivity would be more similar to correlation of stationary neuronal activities than Pearson correlation does since the fractal artifact is effectively eliminated from original time series. Empirical studies on the difference between nonfractal signals and neuronal activities would be valuable to clearly understand the implication of nonfractal connectivity; one of ideas is to acquire both BOLD signals and neuronal process data simultaneously and map together.

The multivariate WLMS estimator proposed in Chapter 4 was more resilient to additive noises than univariate wavelet-based estimators. This estimator, however, is less efficient, and its efficiency becomes worse as the number of time series is larger. Therefore, the future prospect includes developing an advanced noise-resilient estimator which is efficient even in large dimensional networks.

Finally, the influence of fractal behavior on functional connectivity has been verified on the basis of the proposed long memory model of hemodynamic response. Additionally, its significant impacts on information flow also have been verified through simulation studies. As nonfractal connectivity has been introduced to correct the fractal-driven distortion of functional connectivity, it is necessary to develop a novel metric of information flow immune to fractal behavior in order to overcome the fractal artifact of resting state BOLD signals.

In conclusion, this study provides robust theoretical foundations linking long memory and functional connectivity. The long memory model of hemodynamic response enables to figure out not only the physical mechanism of long memory in resting state BOLD signals, but also the association between long memory and functional connectivity. In addition, the proposed fractal-based analysis tech-

niques can be effectively exploited to study the dynamics of endogenous brain activities and the intrinsic properties of functional brain networks from resting state neuroimaging data.

Appendix A

Basic concepts in dynamic system theories

A.1 Langevin equation

Here the multivariate Langevin equation of neuronal population in (2.20) is proved. Since $\epsilon(t) = -\tau_\epsilon^{-1} e^{-t/\tau_\epsilon}$, the Langevin equation of synaptic currents can be obtained from (2.19) as follows

$$
\begin{aligned}
\tau_c \frac{\mathrm{d}I_j(t)}{\mathrm{d}t} &= -\sum_{i=1}^{N} W_{j,i} \frac{\mathrm{d}}{\mathrm{d}t} \int_0^\infty e^{-t/\tau_c} f\left(I_i(t-\tau)\right) \mathrm{d}\tau \\
&= -\sum_{i=1}^{N} W_{j,i} \frac{\mathrm{d}}{\mathrm{d}t} \left\{ \left[e^{-t/\tau_c} \int f\left(I_i(t-\tau)\right) \mathrm{d}\tau \right]_{\tau=0}^{\infty} \right. \\
&\qquad \left. - \int_0^\infty \tau_c e^{-t/\tau_c} \left(\int f\left(I_i(t-\tau)\right) \mathrm{d}\tau \right) \mathrm{d}\tau \right\} \\
&= \sum_{i=1}^{N} W_{j,i} f\left(I_i(t)\right) - I_j(t).
\end{aligned}
\tag{A.1}
$$

Suppose that the gain function f is a sigmoid function. Then, the approximate Langevin equation for action potentials is given by

$$
\begin{aligned}
\tau_c \frac{\mathrm{d}x_j(t)}{\mathrm{d}t} &= \tau_c \frac{\mathrm{d}f\left(I_j(t)\right)}{\mathrm{d}I_j} \frac{\mathrm{d}I_j(t)}{\mathrm{d}t} \\
&= \frac{\mathrm{d}f\left(I_j(t)\right)}{\mathrm{d}I_j} \left(-I_j(t) + \sum_{i=1}^{N} W_{j,i} f\left(I_i(t)\right) \right) \\
&\approx -f\left(I_j(t)\right) + f\left(\sum_{i=1}^{N} W_{j,i} f\left(I_i(t)\right) \right) \\
&= -x_j(t) + f\left(\sum_{i=1}^{N} W_{j,i} x_i(t) \right).
\end{aligned}
\tag{A.2}
$$

A.2 Master equation

The total population activity $n_i(t)$ can be regarded as a Markovian stochastic process which is defined in the state space $\chi := \{0, 1, \cdots, s\}$ and has the following property of conditional probability

$$
P\left(n_i(t_k) \,|\, n_i(t), t < t_k\right) = P\left(n_i(t_k) \,|\, n_i(t_{k-1})\right).
\tag{A.3}
$$

It results in for $t_1 < t_2 < t_3$

$$
\begin{aligned}
P\left(n_i(t_1), n_i(t_2), n_i(t_3)\right) = \\
P\left(n_i(t_1)\right) P\left(n_i(t_2) \,|\, n_i(t_1)\right) P\left(n_i(t_3) \,|\, n_i(t_2)\right).
\end{aligned}
\tag{A.4}
$$

By integrating (A.4) over $n_i(t_2)$, the *Chapman-Komogorov equation* is given as follows

$$
\begin{aligned}
P&\left(n_i(t_3) \,|\, n_i(t_1)\right) \\
&= \int_{\chi} P\left(n_i(t_2) \,|\, n_i(t_1)\right) P\left(n_i(t_3) \,|\, n_i(t_2)\right) \mathrm{d}n_i(t_2).
\end{aligned}
\tag{A.5}
$$

Define the *transition probability* as $P_{a,b}(t) := P(n_i(t) = b \,|\, n_i(0) = a)$, and the *transition rate* as $q(b\,|\,a) := \lim_{\tau \to 0} P_{a,b}(\tau)/\tau$. Assume that for small τ

$$P_{a,b}(\tau) \approx (1 - \gamma(a)\tau)\,\delta(b - a) + \tau q(b\,|\,a) \tag{A.6}$$

where $\gamma(a) = \int_\chi q(b\,|\,a)\,\mathrm{d}b$. If $P(n_i, t) := P_{a,b}(t)$, the following *master equation* is obtained from (A.5) and (A.6)

$$\frac{\partial P(n_i, t)}{\partial t} = \int_\chi \{q(n_i\,|\,y)P(y, t) - q(y\,|\,n_i)P(n_i, t)\}\,\mathrm{d}y. \tag{A.7}$$

If $n_i(t)$ is an one-step process, the master equation can be written as

$$\begin{aligned}
\frac{\partial P(n_i, t)}{\partial t} &= (\mathbb{E} - 1)\,q_-(n_i)P(n_i, t) \\
&\quad + \left(\mathbb{E}^{-1} - 1\right)q_+(n_i)P(n_i, t)
\end{aligned} \tag{A.8}$$

where $\mathbb{E}f(n_i) = f(n_i + 1)$, $\mathbb{E}^{-1}f(n_i) = f(n_i - 1)$, $q_-(n_i) = q(n_i - 1\,|\,n_i)$, and $q_+(n_i) = q(n_i + 1\,|\,n_i)$. In the case of neuronal population activities, $q_-(n_i) = n_i$ and $q_+(n_i) = M_i f(n_i/M_i)$.

A.3   Fokker-Planck equation

Here the Fokker-Planck equation in (2.22) is proved. Since $n_i(t) = M_i \bar{x}_i(t) + M_i^{1/2} \xi_i(t)$ from the definition of $\xi_i(t)$, the first and thirt term in the master equation (2.21) can be expanded into

$$\begin{aligned}
&\mathbb{E}_i^{\pm}\left(T_i^{\mp}(\mathbf{n})P(\mathbf{n}, t)\right) \\
&= \left(\Omega_i^{\mp}(\mathbf{M}\bar{\mathbf{x}}) + \sum_{j=1}^{N} M_j^{-1/2}\frac{\partial \Omega_i^{\mp}(\bar{\mathbf{x}})}{\partial \bar{x}_j}\xi_j(t) + \cdots\right) \\
&\quad \times \left(\Pi(\xi, t) \pm M_i^{-1/2}\frac{\partial \Pi(\xi, t)}{\partial \xi_i} + \frac{M_i^{-1}}{2}\frac{\partial^2 \Pi(\xi, t)}{\partial \xi_i^2} + \cdots\right). \tag{A.9}
\end{aligned}$$

Also, the derivative of probability is equivalent to

$$\frac{\partial P\left(\mathbf{n}, t\right)}{\partial t} = \frac{\partial \Pi(\xi, t)}{\partial t} - \sum_{j=1}^{N} M_j^{1/2} \frac{\partial \bar{x}_j(t)}{\partial t} \frac{\partial \Pi(\xi, t)}{\partial \xi_j}. \tag{A.10}$$

The left and right terms in (2.21) can be replaced with (A.9) and (A.10). Then, the $M_j^{-1/2}$ order terms is canceled due to (2.20), and the remaining parts can be rewritten as

$$\begin{aligned}
\frac{\partial \Pi(\xi, t)}{\partial t} &\approx -\sum_{i=1}^{N} \frac{\partial}{\partial \xi_i} \left[\widetilde{A}_i(\bar{\mathbf{x}}) \Pi\left(\xi, t\right) \right] \\
&\quad + \frac{1}{2} \sum_{i=1}^{N} \frac{\partial^2}{\partial \xi_i^2} \left[\widetilde{B}_i(\bar{\mathbf{x}}) \Pi\left(\xi, t\right) \right]
\end{aligned} \tag{A.11}$$

where $\widetilde{A}_i(\bar{\mathbf{x}}) = \Omega_{i,1}(\bar{\mathbf{x}}) - \Omega_{i,-1}(\bar{\mathbf{x}})$ and $\widetilde{B}_i(\bar{\mathbf{x}}) = \Omega_{i,1}(\bar{\mathbf{x}}) + \Omega_{i,-1}(\bar{\mathbf{x}})$. $\widetilde{A}_i(\bar{\mathbf{x}})$ and $\widetilde{B}_i(\bar{\mathbf{x}})$ can be expanded as

$$\widetilde{A}_i(\mathbf{x}) = \sum_{k=1}^{N} \frac{\partial \widetilde{A}_i}{\partial \bar{x}_k} \xi_k + \frac{1}{2} \sum_{k=1}^{N} \sum_{l=1}^{N} (M_k M_l)^{-1/4} \frac{\partial^2 \widetilde{A}_i}{\partial \bar{x}_k \bar{x}_l} + \cdots, \tag{A.12}$$

$$\widetilde{B}_i(\mathbf{x}) = \widetilde{B}_i(\bar{\mathbf{x}}) + \sum_{k=1}^{N} M_k^{-1/2} \frac{\partial \widetilde{B}_i}{\partial \bar{x}_k} \xi_k + \cdots. \tag{A.13}$$

From (A.11), (A.12) and (A.13), the equation (2.22) is finally obtained.

References

Achard, S., Bassett, D. S., Meyer-Lindenberg, A., & Bullmore, E. (2008). Fractal connectivity of long-memory networks. *Physical Review E*, *77*(3), 036104. 5, 33, 82, 85, 87, 93, 94, 112

Achard, S., Salvador, R., Whitcher, B., Suckling, J., & Bullmore, E. (2006). A resilient, low-frequency, small-world human brain functional network with highly connected association cortical hubs. *The Journal of Neuroscience*, *26*(1), 63–72. 19, 117

Allegrini, P., Menicucci, D., Bedini, R., Fronzoni, L., Gemignani, A., Grigolini, P., West, B. J., & Paradisi, P. (2009). Spontaneous brain activity as a source of ideal 1/f noise. *Physical Review E*, *80*(6), 1–13. 2, 40

Amari, S.-I. (1975). Homogeneous nets of neuron-like elements. *Biological Cybernetics*, *17*(4), 211–220. 13

Amari, S.-i. (1977). Dynamics of pattern formation in lateral-inhibition type neural fields. *Biological Cybernetics*, *27*(2), 77–87. 13

Auer, D. P. (2008). Spontaneous low-frequency blood oxygenation level-dependent fluctuations and functional connectivity analysis of the resting brain. *Magnetic resonance imaging*, *26*(7), 1055–1064. 1

Baba, K., Shibata, R., & Sibuya, M. (2004). Partial correlation and conditional correlation as measures of conditional independence. *Australian & New Zealand Journal of Statistics*, *46*(4), 657–664. 16

Baillie, R. T. (1996). Long memory processes and fractional integration in econometrics. *Journal of Econometrics*, *73*(1), 5–59. 50

Bak, P., Tang, C., & Wiesenfeld, K. (1987). Self-organized criticality: An explanation of the 1/f noise. *Physical Review Letters*, *59*(4), 381–384. 138

Baroni, F., Torres, J. J., & Varona, P. (2010). History-dependent excitability as a single-cell substrate of transient memory for information discrimination. *PLoS ONE*, *5*(12), e15023. 55

Beckmann, C. F., DeLuca, M., Devlin, J. T., & Smith, S. M. (2005). Investigations into resting-state connectivity using independent component analysis. *Philosophical Transactions of the Royal Society B: Biological Sciences*, *360*(1457), 1001–1013. 2

Beggs, J. M., & Plenz, D. (2003). Neuronal avalanches in neocortical circuits. *The Journal of Neuroscience*, *23*(35), 11167–11177. 139

Beran, J. (1992). Statistical methods for data with long-range dependence. *Statistical science*, (pp. 404–416). 31

Beran, J. (1994). *Statistics for Long-Memory Processes*. Chapman and Hall. 2, 31, 32

Birn, R. M., Diamond, J. B., Smith, M. A., & Bandettini, P. A. (2006). Separating respiratory-variation-related fluctuations from neuronal-activity-related fluctuations in fmri. *NeuroImage*, *31*(4), 1536–48. 2, 40

Biswal, B., Yetkin, F., Haughton, V., & Hyde, J. (1995). Functional connectivity in the motor cortex of resting human brain using echo-planar mri. *Magnetic Resonance in Medicine*, *34*, 537–541. 1

Bluhm, R., Williamson, P., Lanius, R., Thberge, J., Densmore, M., Bartha, R., Neufeld, R., & Osuch, E. (2009). Resting state default-mode network connectivity in early depression using a seed region-of-interest analysis: Decreased connectivity with caudate nucleus. *Psychiatry and Clinical Neurosciences*, *63*(6), 754–761. 114

Brandes, U. (2001). A faster algorithm for betweenness centrality. *Journal of Mathematical Sociology*, *25*, 163–177. 72

Bressloff, P. (2009). Stochastic neural field theory and the system-size expansion. *SIAM Journal on Applied Mathematics*, *70*(5), 1488–1521. 13

Brockwell, P., & Davis, R. (2009). *Time Series: Theory and Methods*. Springer. 92

Bullmore, E., Barnes, A., Bassett, D. S., Fornito, A., Kitzbichler, M., Meunier, D., & Suckling, J. (2009). Generic aspects of complexity in brain imaging data and other biological systems. *NeuroImage*, *47*(3), 1125–1134. 18, 139

Bullmore, E., Brammer, M., Williams, S. C., Rabe-Hesketh, S., Janot, N., David, A., Mellers, J., Howard, R., & Sham, P. (1996). Statistical methods of estimation and inference for functional mr image analysis. *Magn Reson Med*, *35*(2), 261–77. 39

Bullmore, E., Fadili, J., Maxim, V., Sendur, L., Whitcher, B., Suckling, J., Brammer, M., & Breakspear, M. (2004). Wavelets and functional magnetic resonance imaging of the human brain. *Neuroimage*, *23 Suppl 1*, S234–49. 22, 39, 89

Bullmore, E., Long, C., Suckling, J., Fadili, J., Calvert, G., Zelaya, F., Carpenter, T. A., & Brammer, M. (2001). Colored noise and computational inference in neurophysiological (fmri) time series analysis: resampling methods in time and wavelet domains. *Hum Brain Mapp*, *12*(2), 61–78. 39

Bullmore, E., & Sporns, O. (2009). Complex brain networks: graph theoretical analysis of structural and functional systems. *Nat Rev Neurosci*, *10*(3), 186–198. 18, 19

Buxton, R. (2002). *Introduction to Functional Magnetic Resonance Imaging: Principles and Techniques*. Cambridge University Press. 3, 40

Buxton, R. B., Uluda, K., Dubowitz, D. J., & Liu, T. T. (2004). Modeling the hemodynamic response to brain activation. *NeuroImage*, *23, Supplement 1*(0), S220–S233. 9

Buxton, R. B., Wong, E. C., & Frank, L. R. (1998). Dynamics of blood flow and oxygenation changes during brain activation: the balloon model. *Magnetic Resonance in Medicine*, *39*(6), 855–64. 8

Coeurjolly, J. F., Amblard, P. O., & Achard, S. (2010). Normalized causal and well-balanced multivariate fractional brownian motion. *arXiv preprint arXiv:1007.2109*. 33

Cootner, P. H., Fama, E. F., Morris, W. S., Taylor, H. M., Mandelbrot, B. B., & Gomory, R. E. (1997). *Fractals and Scaling In Finance: Discontinuity, Concentration, Risk*. Mandelbrot, Benoit B. Springer. 31

Cordes, D., Haughton, V., Carew, J. D., Arfanakis, K., & Maravilla, K. (2002). Hierarchical clustering to measure connectivity in fmri resting-state data. *Magnetic Resonance Imaging*, *20*(4), 305–317. 2

Cordes, D., Haughton, V. M., Arfanakis, K., Carew, J. D., Turski, P. A., Moritz, C. H., Quigley, M. A., & Meyerand, M. E. (2001). Frequencies contributing to functional connectivity in the cerebral cortex in "resting-state" data. *American Journal of Neuroradiology*, *22*(7), 1326–33. 2, 40

Cover, T. M., & Thomas, J. A. (2006). *Elements of Information Theory*. Wiley. 17, 18

Cox, D. R. (1984). Long-range dependence: A review. *Statistics: an appraisal*, (pp. 55–74). 31

Dale, A. M. (1999). Optimal experimental design for event-related fmri. *Hum Brain Mapp*, *8*(2-3), 109–14. 39

Daunizeau, J., David, O., & Stephan, K. E. (2011). Dynamic causal modelling: A critical review of the biophysical and statistical foundations. *NeuroImage*, *58*(2), 312–322. 13

Didier, G., & Pipiras, V. (2011). Integral representations and properties of operator fractional brownian motions. *Bernoulli*, *17*(1), 1–33. 33

Doukhan, P., Lang, G., Surgailis, D., & Teyssire, G. (2010). *Dependence in Probability and Statistics*. Lecture Notes in Statistics. Springer. 31

Doukhan, P., Oppenheim, G., & Taqqu, M. S. (2002). *Theory and Applications of Long-Range Dependence*. Birkhuser Boston. 31

Eke, A., Herman, P., & Hajnal, M. (2006). Fractal and noisy cbv dynamics in humans: influence of age and gender. *Journal of Cerebral Blood Flow and Metabolism*, *26*(7), 891–8. 3

Embrechts, P. (2001). *Selfsimilar Processes*. Princeton Series in Applied Mathematics. Princeton University Press. 31

Erdélyi, A., Magnus, W., Oberhettinger, F., Tricomi, F., & Bateman, H. (1953). *Higher transcendental functions*. New York: McGraw-Hill. 48

Expert, P., Lambiotte, R., Chialvo, D. R., Christensen, K., Jensen, H. J., Sharp, D. J., & Turkheimer, F. (2011). Self-similar correlation function in brain resting-state functional magnetic resonance imaging. *Journal of The Royal Society Interface*, *8*(57), 472–9. 2

Fadel, P. J., Barman, S. M., Phillips, S. W., & Gebber, G. L. (2004). Fractal fluctuations in human respiration. *Journal of Applied Physiology*, *97*(6), 2056–64. 2

Fadili, M. J., & Bullmore, E. T. (2002). Wavelet-generalized least squares: A new blu estimator of linear regression models with 1/f errors. *NeuroImage*, *15*(1), 217–232. 32, 42, 44

Fox, M. D., & Raichle, M. E. (2007). Spontaneous fluctuations in brain activity observed with functional magnetic resonance imaging. *Nat Rev Neurosci*, *8*(9), 700–711. 1, 78

Freeman, L. C. (1978). Centrality in social networks conceptual clarification. *Social Networks*, *1*(3), 215–239. 21

Friston, K. J., Harrison, L., & Penny, W. (2003). Dynamic causal modelling. *NeuroImage*, *19*(4), 1273–302. 12

Friston, K. J., Jezzard, P., & Turner, R. (1994). Analysis of functional mri time-series. *Human Brain Mapping*, *1*(2), 153–171. 7

Friston, K. J., Josephs, O., Rees, G., & Turner, R. (1998). Nonlinear event-related responses in fmri. *Magnetic Resonance in Medicine*, *39*(1), 41–52. 60

Friston, K. J., Mechelli, A., Turner, R., & Price, C. J. (2000). Nonlinear responses in fmri: The balloon model, volterra kernels, and other hemodynamics. *NeuroImage*, *12*(4), 466–477. 9

Granger, C. W. J. (1980). Long memory relationships and the aggregation of dynamic models. *Journal of Econometrics*, *14*(2), 227–238. 35

Greicius, M. (2008). Resting-state functional connectivity in neuropsychiatric disorders. *Current Opinion in Neurology*, *21*(4), 424–430 10.1097/WCO.0b013e328306f2c5. 114

Greicius, M. D., Flores, B. H., Menon, V., Glover, G. H., Solvason, H. B., Kenna, H., Reiss, A. L., & Schatzberg, A. F. (2007). Resting-state functional connectivity in major depression: Abnormally increased contributions from subgenual cingulate cortex and thalamus. *Biological Psychiatry*, *62*(5), 429–437. 1, 114

Guimera, R., & Amaral, L. A. N. (2005). Cartography of complex networks: modules and universal roles. *Journal of Statistical Mechanics: Theory and Experiment*, *2005*(02), P02001. 22

Hannan, E. J. (1970). *The Spectral Theory of Vector Processes*, (pp. 32–126). John Wiley & Sons, Inc. 57

Hennig, J., Nauerth, A., & Friedburg, H. (1986). Rare imaging: A fast imaging method for clinical mr. *Magnetic Resonance in Medicine*, *3*(6), 823–833. 127

Henson, R., & Friston, K. (2006). *Convolution models for fMRI*. Burlington, Massachusetts: Academic Press. 8, 46

Herman, P., Kocsis, L., & Eke, A. (2009). Fractal characterization of complexity in dynamic signals: application to cerebral hemodynamics. *Methods in Molecular Medicine*, *489*, 23–40. 3, 40, 41

Herman, P., Sanganahalli, B. G., Hyder, F., & Eke, A. (2011). Fractal analysis of spontaneous fluctuations of the bold signal in rat brain. *NeuroImage*, *58*(4), 1060–1069. 2, 126

Higuchi, T. (1988). Approach to an irregular time series on the basis of the fractal theory. *Physica D: Nonlinear Phenomena*, *31*(2), 277–283. 32

Hinrichs, H., Heinze, H. J., & Schoenfeld, M. A. (2006). Causal visual interactions as revealed by an information theoretic measure and fmri. *NeuroImage*, *31*(3), 1051–1060. 17

Hinrichs, H., Noesselt, T., & Heinze, H.-J. (2008). Directed information flowa model free measure to analyze causal interactions in event related eeg-meg-experiments. *Human Brain Mapping*, *29*(2), 193–206. 17

Hodgkin, A. L., & Huxley, A. F. (1952). A quantitative description of membrane current and its application to conduction and excitation in nerve. *The Journal of Physiology*, *117*(4), 500–544. 10

Honey, C. J., Ktter, R., Breakspear, M., & Sporns, O. (2007). Network structure of cerebral cortex shapes functional connectivity on multiple time scales. *Proceedings of the National Academy of Sciences*, *104*(24), 10240–10245. 71, 72, 79

Hosking, J. R. M. (1981). Fractional differencing. *Biometrika*, *68*(1), 165–176. 35

Humphries, M. D., & Gurney, K. (2008). Network 'small-world-ness': A quantitative method for determining canonical network equivalence. *PLoS ONE*, *3*(4), e0002051. 22

Izhikevich, E. M. (2003). Simple model of spiking neurons. *Neural Networks, IEEE Transactions on*, *14*(6), 1569–1572. 10

Jenkinson, M., Beckmann, C. F., Behrens, T. E. J., Woolrich, M. W., & Smith, S. M. (2012). Fsl. *NeuroImage*, *62*(2), 782–790. 128

Jenkinson, M., & Smith, S. (2001). A global optimisation method for robust affine registration of brain images. *Medical Image Analysis*, *5*(2), 143–156. 128

Jirsa, V. K., & Haken, H. (1996). Field theory of electromagnetic brain activity. *Physical Review Letters*, *77*(5), 960–963. 13

Jirsa, V. K., & Haken, H. (1997). A derivation of a macroscopic field theory of the brain from the quasi-microscopic neural dynamics. *Physica D: Nonlinear Phenomena*, *99*(4), 503–526. 13

Johnson, B. (1974). Generalized lerch zeta function. *Pacific Journal of Mathematics*, *53*(1), 189–193. 48

Josephs, O., & Henson, R. N. A. (1999). Event-related functional magnetic resonance imaging: modelling, inference and optimization. *Philosophical Transactions of the Royal Society of London. Series B: Biological Sciences*, *354*(1387), 1215–1228. 60

Jumarie, G. (1990). *Relative information: theories and applications*. Springer series in synergetics. Springer. 17, 18

Kaiser, A., & Schreiber, T. (2002). Information transfer in continuous processes. *Physica D: Nonlinear Phenomena*, *166*(12), 43–62. 18, 71

Kitzbichler, M. G., Smith, M. L., Christensen, S. R., & Bullmore, E. (2009). Broadband criticality of human brain network synchronization. *PLoS Comput Biol*, *5*(3), e1000314. 139

Kullback, S. (1968). *Information Theory and Statistics*. Dover Books on Mathematics Series. Dover Publ. 17

Latka, M., & Latka, D. (2003). Fluctuations in cerebral hemodynamics. Tech. rep., DTIC Document. 3

Latka, M., Turalska, M., Kolodziej, D., Latka, D., Goldstein, B., & West, B. J. (2005). Scaling properties of cerebral hemodynamics. *Fractals in Biology and Medicine*, *Part 2*, 121–129. 3, 40

Latora, V., & Marchiori, M. (2001). Efficient behavior of small-world networks. *Physical Review Letters*, *87*(19), 198701. 21

Lavancier, F., Philippe, A., & Surgailis, D. (2009). Covariance function of vector self-similar processes. *Statistics & Probability Letters*, *79*(23), 2415–2421. 35

Ledesma, S., & Liu, D. (2000). Synthesis of fractional gaussian noise using linear approximation for generating self-similar network traffic. *SIGCOMM Comput. Commun. Rev.*, *30*(2), 4–17. 31

Locascio, J. J., Jennings, P. J., Moore, C. I., & Corkin, S. (1997). Time series analysis in the time domain and resampling methods for studies of functional magnetic resonance brain imaging. *Hum Brain Mapp*, *5*(3), 168–93. 39

Lord, A., Horn, D., Breakspear, M., & Walter, M. (2012). Changes in community structure of resting state functional connectivity in unipolar depression. *PLoS ONE*, *7*(8), e41282. 114, 115, 121

Lowen, S. B., & Teich, M. C. (1991). Doubly stochastic poisson point process driven by fractal shot noise. *Physical Review A*, *43*(8), 4192–4215. 16, 80

Lowen, S. B., & Teich, M. C. (2005). *Fractal-Based Point Processes*. Wiley Series in Probability and Statistics. Wiley. 16, 31, 80

Mandelbrot, B. (1977). *Fractals: Form, Chance And Dimension*. San Francisco: W.H. Freeman. 31

Mandelbrot, B., & Van Ness, J. (1968). Fractional brownian motions, fractional noises and applications. *SIAM Review*, *10*(4), 422–437. 34

Mandelbrot, B. B. (1983). *The Fractal Geometry of Nature*. W.H. Freeman. 31

Mandelbrot, B. B., & Taqqu, M. S. (1979). Robust r/s analysis of long-run serial correlation. *Bulletin of the International Statistical Institute*, *48*(2), 59–104. 32

Mandeville, J. B., Marota, J. J. A., Ayata, C., Zaharchuk, G., Moskowitz, M. A., Rosen, B. R., & Weisskoff, R. M. (1999). Evidence of a cerebrovascular postarteriole windkessel with delayed compliance. *J Cereb Blood Flow Metab*, *19*(6), 679–689. 8

Marmarelis, P. (2004). *Nonlinear Dynamic Modeling of Physiological Systems*. John Wiley and Sons. 60, 61

Marrelec, G., Horwitz, B., Kim, J., Plgrini-Issac, M., Benali, H., & Doyon, J. (2007). Using partial correlation to enhance structural equation modeling of functional mri data. *Magnetic resonance imaging*, *25*(8), 1181–1189. 1

Maxim, V., Sendur, L., Fadili, J., Suckling, J., Gould, R., Howard, R., & Bullmore, E. (2005). Fractional gaussian noise, functional mri and alzheimer's disease. *NeuroImage*, *25*(1), 141–58. 2, 31, 32, 39

Mazzoni, A., Broccard, F. D., Garcia-Perez, E., Bonifazi, P., Ruaro, M. E., & Torre, V. (2007). On the dynamics of the spontaneous activity in neuronal networks. *PloS One*, *2*(5), e439. 2, 40

Mechelli, A., Price, C. J., & Friston, K. J. (2001). Nonlinear coupling between evoked rcbf and bold signals: A simulation study of hemodynamic responses. *NeuroImage*, *14*(4), 862–872. 9

Meyer, F. G. (2003). Wavelet-based estimation of a semiparametric generalized linear model of fmri time-series. *IEEE transactions on Medical Imaging*, *22*(3), 315–22. 2

Molz, F. J., Liu, H. H., & Szulga, J. (1997). Fractional brownian motion and fractional gaussian noise in subsurface hydrology: A review, presentation of fundamental properties, and extensions. *Water Resour. Res.*, *33*(10), 2273–2286. 31

Montoya, J. M., & Sol, R. V. (2002). Small world patterns in food webs. *Journal of Theoretical Biology*, *214*(3), 405–412. 117

Moulines, E., Roueff, F., & Taqqu, M. S. (2007). On the spectral density of the wavelet coefficients of long-memory time series with application to the log-regression estimation of the memory parameter. *Journal of Time Series Analysis*, *28*(2), 155–187. 35, 36

Newman, M. E. J. (2004). Fast algorithm for detecting community structure in networks. *Physical Review E*, *69*(6), 066133. 22

Nir, Y., Fisch, L., Mukamel, R., Gelbard-Sagiv, H., Arieli, A., Fried, I., & Malach, R. (2007). Coupling between neuronal firing rate, gamma lfp, and bold fmri is related to interneuronal correlations. *Current Biology*, *17*(15), 1275–1285. 41

Nunez, P. L. (1974). The brain wave equation: a model for the eeg. *Mathematical Biosciences*, *21*(34), 279–297. 13

Ogawa, S., Lee, T. M., Kay, A. R., & Tank, D. W. (1990). Brain magnetic resonance imaging with contrast dependent on blood oxygenation. *Proceedings of the National Academy of Sciences*, *87*(24), 9868–9872. 1

Paxinos, G., & Watson, C. (2007). *The Rat Brain in Stereotaxic Coordinates: Hard Cover Edition*. Academic Press. 128

Peng, C. K., Buldyrev, S. V., Havlin, S., Simons, M., Stanley, H. E., & Goldberger, A. L. (1994). Mosaic organization of dna nucleotides. *Physical Review E*, *49*(2), 1685–1689. 32

Peng, C. K., Havlin, S., Hausdorff, J. M., Mietus, J. E., Stanley, H. E., & Goldberger, A. L. (1995). Fractal mechanisms and heart rate dynamics. *Journal of Electrocardiology*, *28*, 59–65. 2, 32

Peng, C. K., Mietus, J. E., Liu, Y., Lee, C., Hausdorff, J. M., Stanley, H. E., Goldberger, A. L., & Lipsitz, L. A. (2002). Quantifying fractal dynamics of human respiration: age and gender effects. *Annals of Biomedical Engineering*, *30*(5), 683–92. 2

Percival, D., & Walden, A. (2006). *Wavelet Methods for Time Series Analysis*. Cambridge University Press. 28, 89, 91, 93, 97

Pérez-Stable, E. J., Miranda, J., Muñoz, R. F., & Ying, Y. (1990). Depression in medical outpatients: Underrecognition and misdiagnosis. *Archives of Internal Medicine*, *150*(5), 1083–1088. 114

Priestley, B. (1989). *Spectral Analysis and Time Series*. Probability and Mathematical Statistics. Academic Press. 31

Purdon, P. L., & Weisskoff, R. M. (1998). Effect of temporal autocorrelation due to physiological noise and stimulus paradigm on voxel-level false-positive rates in fmri. *Human Brain Mapping*, *6*(4), 239–249. 39

Rajapakse, J. C., Kruggel, F., Maisog, J. M., & Yves von Cramon, D. (1998). Modeling hemodynamic response for analysis of functional mri time-series. *Human Brain Mapping*, *6*(4), 283–300. 47

Ramot, M., Wilf, M., Goldberg, H., Weiss, T., Deouell, L. Y., & Malach, R. (2011). Coupling between spontaneous (resting state) fmri fluctuations and human oculo-motor activity. *NeuroImage*, *58*(1), 213–225. 41, 42

Rangarajan, G., & Ding, M. (2003). *Processes with Long-Range Correlations: Theory and Applications*. Lecture Notes in Physics. Springer. 31

Riedi, R. H. (1999). Multifractal processes. Tech. rep., DTIC Document. 2

Robinson, P. M. (1995). Log-periodogram regression of time series with long range dependence. *The annals of Statistics*, (pp. 1048–1072). 32

Robinson, P. M. (2003). *Time Series With Long Memory*. Advanced Texts in Econometrics Series. Oxford University Press. 31

Rosa, M. J., Kilner, J., Blankenburg, F., Josephs, O., & Penny, W. (2010). Estimating the transfer function from neuronal activity to bold using simultaneous eeg-fmri. *NeuroImage*, *49*(2), 1496–1509. 41

Rubinov, M., & Sporns, O. (2010). Complex network measures of brain connectivity: Uses and interpretations. *NeuroImage*, *52*(3), 1059–1069. 22, 72

Salvador, R., Suckling, J., Coleman, M. R., Pickard, J. D., Menon, D., & Bullmore, E. (2005). Neurophysiological architecture of functional magnetic resonance images of human brain. *Cerebral Cortex*, *15*(9), 1332–1342. 1, 2, 114

Schmitt, D. T., & Ivanov, P. (2007). Fractal scale-invariant and nonlinear properties of cardiac dynamics remain stable with advanced age: a new mechanistic picture of cardiac control in healthy elderly. *American Journal of Physiology. Regulatory, Integrative and Comparative Physiology*, *293*(5), R1923–37. 2, 40

Schreiber, T. (2000). Measuring information transfer. *Physical Review Letters*, *85*(2), 461–464. 18

Schwarz, A. J., Gozzi, A., & Bifone, A. (2008). Community structure and modularity in networks of correlated brain activity. *Magnetic Resonance Imaging*, *26*(7), 914–920. 132

Shannon, C. E., & Weaver, W. (1949). *The Mathematical Theory of Communication*. Illini books. Univ. Illinois Press. 17

Sheline, Y. I., Barch, D. M., Price, J. L., Rundle, M. M., Vaishnavi, S. N., Snyder, A. Z., Mintun, M. A., Wang, S., Coalson, R. S., & Raichle, M. E. (2009). The default mode network and self-referential processes in depression. *Proceedings of the National Academy of Sciences*, *106*(6), 1942–1947. 114

Shimotsu, K. (2007). Gaussian semiparametric estimation of multivariate fractionally integrated processes. *Journal of Econometrics*, *137*(2), 277–310. 35

Shulman, R. G., Rothman, D. L., Behar, K. L., & Hyder, F. (2004). Energetic basis of brain activity: implications for neuroimaging. *Trends in Neurosciences*, *27*(8), 489–495. 1

Sporns, O. (2011). *Networks of the Brain*. Mit Press. 18, 22

Stam, C. J., & de Bruin, E. A. (2004). Scale-free dynamics of global functional connectivity in the human brain. *Human Brain Mapping*, *22*(2), 97–109. 2

Stephan, K. E., Kasper, L., Harrison, L. M., Daunizeau, J., den Ouden, H. E. M., Breakspear, M., & Friston, K. J. (2008). Nonlinear dynamic causal models for fmri. *NeuroImage*, *42*(2), 649–662. 12

Stoev, S. A., & Taqqu, M. S. (2006). How rich is the class of multifractional brownian motions? *Stochastic Processes and their Applications*, *116*(2), 200–221. 34

Tagliazucchi, E., Balenzuela, P., Fraiman, D., & Chialvo, D. R. (2012). Criticality in large-scale brain fmri dynamics unveiled by a novel point process analysis. *Frontiers in Physiology*, *3*. 41, 139

Taqqu, M. S., Teverovsky, V., & Willinger, W. (1995). Estimators for long-range dependence: an empirical study. *Fractals*, *03*(04), 785–798. 32

Teich, M. C. (1989). Fractal character of the auditory neural spike train. *IEEE Transactions on Biomedical Engineering*, *36*(1), 150–60. 2

Teich, M. C., Heneghan, C., Lowen, S. B., Ozaki, T., & Kaplan, E. (1997). Fractal character of the neural spike train in the visual system of the cat. *Journal of the Optical Society of America. A, Optics, image science, and vision*, *14*(3), 529–46. 2

Tzourio-Mazoyer, N., Landeau, B., Papathanassiou, D., Crivello, F., Etard, O., Delcroix, N., Mazoyer, B., & Joliot, M. (2002). Automated anatomical labeling of activations in spm using a macroscopic anatomical parcellation of the mni mri single-subject brain. *NeuroImage*, *15*(1), 273–289. 114

van de Ven, V. G., Formisano, E., Prvulovic, D., Roeder, C. H., & Linden, D. E. J. (2004). Functional connectivity as revealed by spatial independent component analysis of fmri measurements during rest. *Human Brain Mapping*, *22*(3), 165–178. 2

Van de Ville, D., Britz, J., & Michel, C. M. (2010). Eeg microstate sequences in healthy humans at rest reveal scale-free dynamics. *Proceedings of the National Academy of Sciences of the United States of America*, *107*(42), 18179–84. 2

Vidakovic, B. (2009). *Statistical Modeling by Wavelets*. Wiley Series in Probability and Statistics. Wiley. 22

Watts, D. J., & Strogatz, S. H. (1998). Collective dynamics of /'small-world/' networks. *Nature*, *393*(6684), 440–442. 21, 22, 117

West, B. J., Latka, M., Glaubic-Latka, M., & Latka, D. (2003). Multifractality of cerebral blood flow. *Physica A: Statistical Mechanics and its Applications*, *318*(3-4), 453–460. 3, 40

West, B. J., Zhang, R., Sanders, A. W., Miniyar, S., Zuckerman, J. H., & Levine, B. D. (1999). Fractal fluctuations in cardiac time series. *Physica A: Statistical Mechanics and its Applications*, *270*(34), 552–566. 2

Willinger, W., Taqqu, M. S., & Teverovsky, V. (1999). Stock market prices and long-range dependence. *Finance and Stochastics*, *3*(1), 1–13. 31

Wilson, H. R., & Cowan, J. D. (1972). Excitatory and inhibitory interactions in localized populations of model neurons. *Biophysical Journal*, *12*(1), 1–24. 13

Wilson, H. R., & Cowan, J. D. (1973). A mathematical theory of the functional dynamics of cortical and thalamic nervous tissue. *Kybernetik*, *13*(2), 55–80. 13

Wink, A. M., Bullmore, E., Barnes, A., Bernard, F., & Suckling, J. (2008). Monofractal and multifractal dynamics of low frequency endogenous brain oscillations in functional mri. *Human Brain Mapping*, *29*(7), 791–801. 2, 3

Woolrich, M. W., Ripley, B. D., Brady, M., & Smith, S. M. (2001). Temporal autocorrelation in univariate linear modeling of fmri data. *NeuroImage*, *14*(6), 1370–86. 2

Wornell, G. (1996). *Signal processing with fractals: a wavelet-based approach*. Prentice Hall signal processing series. Prentice Hall PTR. 22

Wornell, G. W. (1993). Wavelet-based representations for the 1/f family of fractal processes. *Proceedings of the IEEE*, *81*(10), 1428–1450. 22, 89

Wornell, G. W., & Oppenheim, A. V. (1992). Estimation of fractal signals from noisy measurements using wavelets. *Signal Processing, IEEE Transactions on*, *40*(3), 611–623. 89

Worsley, K. J., Liao, C. H., Aston, J., Petre, V., Duncan, G. H., Morales, F., & Evans, A. C. (2002). A general statistical analysis for fmri data. *NeuroImage*, *15*(1), 1–15. 39

Yamamoto, Y., Nakamura, Y., Sato, H., Yamamoto, M., Kato, K., & Hughson, R. L. (1995). On the fractal nature of heart rate variability in humans: effects of vagal blockade. *American Journal of Physiology - Regulatory, Integrative and Comparative Physiology*, *269*(4), R830–R837. 2

Yan, C., & Zang, Y. (2010). Dparsf: a matlab toolbox for "pipeline" data analysis of resting-state fmri. *Frontiers in Systems Neuroscience*, *4*. 114

Zarahn, E., Aguirre, G. K., & D'Esposito, M. (1997). Empirical analyses of bold fmri statistics. i. spatially unsmoothed data collected under null-hypothesis conditions. *NeuroImage*, *5*(3), 179–97. 2

Zhang, R., Zuckerman, J. H., & Levine, B. D. (2000). Spontaneous fluctuations in cerebral blood flow: insights from extended-duration recordings in humans. *American Journal of Physiology-Heart and Circulatory Physiology*, *278*(6), H1848–55. 3, 40, 41

Index

Lebenslauf

Persönliche Daten

Wonsang You
Rudolf-Wolf-Str. 17
39112 Magdeburg

Tel. (0391) 8370 8679
E-mail: you@ovgu.de

Studium

08/2008	M.Sc. Engineering, Korea Advanced Institute of Science and Technology (KAIST).
08/2003	B.E. Electronic Engineering, Sogang University.

Berufstätigkeit

08/2009–12/2012	Wissenschaftler Mitarbeiter, Leibniz-Institut für Neurobiologie, Magdeburg.
04/2011	Guest researcher, Gipsa-lab, Grenoble.
02/2007–12/2007	Teaching assistant, KAIST, South Korea.
08/2005–07/2008	Research assistant, KAIST, South Korea.
07/2003–03/2005	Electronic engineer, Hanwha Corporation, South Korea.

Magdeburg, 2. Januar 2013